

DISSERTATION

# Influence of the drive torque distribution on vehicle handling and stability

carried out for the purpose of obtaining the degree of  
Doctor technicae (Dr.techn.), submitted at TU Wien, Faculty of  
Mechanical and Industrial Engineering

**Manuel Eberhart**

Mat. Nr.: 11778878

under the supervision of

Univ.Prof. Dipl.-Ing. Dr.techn. Johannes Edelmann  
Institute of Mechanics and Mechatronics

Vienna, December 2025

reviewed by

Prof. Dr-Ing Gianpiero Mastinu  
Department of Mechanical Engineering  
Politecnico di Milano

Ao.Univ.Prof. Dipl.-Ing. Dr.techn. Manfred Plöchl  
Institute of Mechanics and Mechatronics  
TU Wien



I confirm, that the printing of this thesis requires the approval of the examination board.

*Affidavit*

I declare in lieu of oath, that I wrote this thesis and performed the associated research myself, using only literature cited in this volume. I confirm that this work is original and has not been submitted elsewhere for any examination, nor is it currently under consideration for a thesis elsewhere. I acknowledge that the submitted work will be checked using suitable and state-of-the-art means (plagiarism detection software).

---

City, date

---

Signature

## Danksagung

Zunächst möchte ich meiner Familie einen großen Dank aussprechen, die mich in allen Lebenslagen bedingungslos unterstützt sowie mein Studium ermöglicht und begleitet hat.

Außerdem möchte ich mich herzlich bei den Kolleginnen und Kollegen des Instituts für Mechanik und Mechatronik der TU Wien, insbesondere des Forschungsbereichs für Technische Dynamik und Fahrzeugdynamik, für das sehr angenehme Arbeitsklima und den wertvollen fachlichen Austausch bedanken. Besonders bedanken möchte ich mich bei Herrn Dipl.-Ing. Philipp Gratzner, mit dem ich mir in diesem Zeitraum das Büro teilen durfte. Er hat mich durch inhaltlich spannende Diskussionen und neue Ideen stets unterstützt und mir bei dem einen oder anderen Feierabendbier neue Motivation und Schwung gegeben.

Diese Dissertation wurde erst durch die Finanzierung der Assistentenstelle sowie die umfassende Unterstützung des Projektpartners CARIAD SE ermöglicht. Besonderer Dank hierfür gilt Herrn Dipl.-Ing. Martin Arndt, der als enger Ansprechpartner diese Forschungspartnerschaft begleitet hat, sowie Herrn Dr.-Ing. Michael Unterreiner für das Ermöglichen vieler schöner Fahrdynamikerprobungen sowie die Initiation der Zusammenarbeit.

Ich möchte mich auch besonders bei Herrn Prof. Alois Steindl bedanken. Durch seine wertvolle inhaltliche Unterstützung bei der mathematischen Formulierung der Bifurkationsanalysen hat er einen wesentlichen Beitrag geleistet und mir zugleich die Möglichkeit gegeben, in diesem Themenfeld sehr viel zu lernen.

Abschließend möchte ich Herrn Prof. Johannes Edelmann und Herrn Prof. Manfred Plöchl einen besonderen Dank für die Betreuung dieser Arbeit aussprechen. Ihre stete Bereitschaft, für Fragen und inhaltliche Diskussionen zur Verfügung zu stehen, sowie die Freiheit, die sie mir bei der Gestaltung dieser Arbeit gelassen haben, haben ein äußerst angenehmes und produktives Arbeitsumfeld geschaffen. Neben der fachlichen Zusammenarbeit werden mir insbesondere die zahlreichen gemeinsamen Fahrdynamikerprobungen und der freundschaftliche, lockere Umgang miteinander in schöner Erinnerung bleiben.

# Contents

<b>1. Introduction and scientific context</b>	<b>1</b>
1.1. Motivation . . . . .	1
1.2. State-of-the-art . . . . .	1
1.3. Research scope . . . . .	4
<b>2. Modelling</b>	<b>6</b>
2.1. Vehicle models . . . . .	6
2.2. Tyre models . . . . .	7
<b>3. Methods and assumptions</b>	<b>10</b>
3.1. Bifurcation analysis and continuation algorithm . . . . .	10
3.2. Stability of first order and modal analysis . . . . .	11
3.3. Controllability analysis . . . . .	11
3.4. Quasi-steady-state assumption . . . . .	12
3.5. Nonlinear handling diagram under longitudinal acceleration . . . . .	12
3.6. GG diagram . . . . .	14
<b>4. Summary of the articles</b>	<b>16</b>
<b>5. Scientific impact</b>	<b>19</b>
<b>Paper A</b>	<b>25</b>
<b>Paper B</b>	<b>47</b>
<b>Paper C</b>	<b>61</b>
<b>Paper D</b>	<b>77</b>

## Abstract

Modern powertrain topologies of electric all-wheel drive vehicles often include multiple motors, offering the advantage of arbitrary drive torque distribution between the individual axles or wheels, and providing new capabilities in vehicle dynamics control. This cumulative thesis investigates the influence of the front-to-rear drive torque distribution on vehicle lateral and yaw dynamics, taking into account individual motors at the front and rear axles. Considering the mutual influence of longitudinal and lateral tyre forces in the combined slip region, variable drive torque distribution may significantly influence the handling characteristics and stability properties of the vehicle. Hence, a profound understanding of this coupled behaviour is necessary.

For automated and assisted driving and for safe operation near the limits of handling, vehicle control systems should be capable to execute extreme manoeuvres or support the driver, where nonlinear system properties significantly affect stability, controllability, and consequently, safety of the vehicle. Utilising the nonlinear handling regime, including large vehicle sideslip angles, may be beneficial in particular cases to increase manoeuvrability, e.g. to avoid obstacles. A theoretical investigation of a steady-state high sideslip manoeuvre, the powerslide, is conducted regarding the influence of the drive torque distribution on its dynamics. Steady-state conditions and corresponding stability properties are derived, and the effectiveness of different actuator inputs, i.e., steering angle, total drive torque, and drive torque distribution, in stabilising the unstable powerslide is analysed and discussed. The results indicate that the drive torque distribution is an effective control input for the stabilisation task and may be superior to the total drive torque.

Considering rear-wheel drive only, the dynamic behaviour after the loss of stability at the powerslide is studied by applying bifurcation analysis. For a range of constant steering angles and drive torques, the vehicle motion and states converge either to a stable equilibrium with a considerably smaller radius of curvature than in the considered powerslide condition, or to a stable limit cycle orbiting an unstable equilibrium. Vehicle measurements confirm these theoretical findings.

In combined longitudinal and lateral accelerated manoeuvres, the change in vehicle handling and stability properties resulting from modifying the drive torque distribution in all-wheel drive vehicles is analysed, and different types of loss of stability are identified utilising bifurcation analysis. Besides Hopf and Fold bifurcations, the Takens–Bogdanov bifurcation is studied in more detail, revealing that the respective solution branch represents the boundary between final understeer and final oversteer of the vehicle, defining the maximum possible, stable acceleration envelope. Therefore, the drive torque distribution at the Takens–Bogdanov branch may be considered a good design criterion for a safe and performant powertrain baseline setup, which is validated through comparison with the optimised GG envelope of the vehicle. Related Hopf and Fold branches define limits for practically reasonable drive torque distributions.

## Kurzfassung

Neue Antriebsarchitekturen in allradgetriebenen Elektrofahrzeugen inkludieren oft mehrere individuelle Antriebsmotoren und bieten im Vergleich zu mechanisch gekoppelten Antriebssystemen neue Möglichkeiten für Fahrdynamikregelsysteme. Diese Arbeit untersucht den Einfluss der Momentenverteilung zwischen Vorder- und Hinterachse auf die Lateraldynamik von Fahrzeugen unter Berücksichtigung einzelner Motoren an der Vorder- und Hinterachse. Die variable Momentenverteilung zwischen Vorder- und Hinterachse, in Kombination mit der gegenseitigen Beeinflussung der Reifenlängs- und Reifenquerkräfte im kombinierten Schlupfbereich, kann einen erheblichen Einfluss auf die Handling- und Stabilitätseigenschaften haben, was ein tiefgehendes Verständnis des gemeinsamen Einflusses erforderlich macht.

Vor allem für das automatisierte Fahren müssen Fahrzeugregelsysteme in der Lage sein, den fahrdynamischen Grenzbereich, bei dem nichtlineares Systemverhalten auftritt und die Stabilität und Handlingeigenschaften maßgeblich beeinflusst, zu beherrschen. Die Nutzung der nichtlinearen Handlingeigenschaften des Fahrzeugs, einschließlich großer Schwimmwinkel, kann in bestimmten Fällen die Manövrierfähigkeit, beispielsweise für Ausweichmanöver, erhöhen. Es erfolgt eine theoretische Untersuchung des Powerslides, der ein instabiler Fahrzustand ist, wobei der Einfluss der Momentenverteilung auf die stationären Zustände sowie die Stabilitätseigenschaften analysiert wird. Verschiedene Systemeingänge – Lenkwinkel, Gesamtmoment und Momentenverteilung – werden hinsichtlich der Steuerbarkeit des instabilen Modes des Powerslides analysiert. Die Ergebnisse zeigen, dass die Momentenverteilung ein effektiver Akteur zur Stabilisierung des Powerslides ist und dem Gesamtmoment überlegen sein kann.

Für ein Fahrzeug mit Hinterradantrieb wird die Dynamik nach Verlust der Stabilität, das postkritische Verhalten, bei konstant gehaltenen Fahrereingängen untersucht. Dabei konvergiert der Fahrzustand entweder zu einem stabilen stationären Zustand mit sehr kleinem Kurvenradius oder zu einem stabilen Grenzyklus, der einem instabilen Gleichgewichtszustand zugehörig ist. Messungen mit einem Versuchsfahrzeug bestätigen die theoretischen Erkenntnisse.

Zusätzlich wird der Einfluss der Momentenverteilung bei Manövern mit gleichzeitiger Längs- und Querbeschleunigung untersucht, wobei unterschiedliche Arten des Stabilitätsverlusts identifiziert werden. Die Takens–Bogdanov Lösung stellt die Grenze zwischen Unter- und Übersteuern im Grenzbereich dar und definiert gleichzeitig das maximal mögliche Beschleunigungspotenzial stabiler Fahrzustände, das im GG-Diagramm veranschaulicht wird. Daraus ergibt sich, dass die Momentenverteilung entlang der Takens–Bogdanov Lösung ein geeignetes Auslegungskriterium für eine sichere und gleichzeitig performante Allradgrundverteilung ist, was durch den Vergleich mit dem durch Optimierung berechneten GG-Diagramm bestätigt wird. Neben der Takens–Bogdanov Lösung werden zugehörige Hopf und Fold Lösungen identifiziert, die zugleich die Grenzen des praktisch relevanten Stellbereichs für die Momentenverteilung darstellen.



# 1. Introduction and scientific context

## 1.1. Motivation

Modern powertrain topologies of electric all-wheel drive vehicles often include multiple motors, offering new capabilities in vehicle dynamics control. A typical powertrain topology of electric all-wheel drive vehicles consists of individual, not mechanically coupled motors at the front and rear axles, [1], as considered in this thesis. The arbitrary front-to-rear drive torque distribution may improve the ‘agility’ and manoeuvrability of the vehicle, and enhance stability properties and performance potential.

The interaction between the tyre and the road surface is one of the main factors determining vehicle dynamics. In the combined slip region of the tyre, the mutual influence of longitudinal and lateral tyre forces enables an adaptation of the lateral tyre force through a modulation of the longitudinal tyre force or longitudinal slip. Especially at the limits of handling, the mutual influence of the longitudinal and lateral tyre forces is significant. The effect of reducing lateral tyre force by increasing longitudinal tyre force, together with variable drive torque distribution, allows to influence the vehicle handling characteristics and stability properties significantly.

As the characteristics of this mutual influence depend on the slip, the effectiveness of drive torque distribution modifications changes depending on the vehicle state. For example, at regular steady-state cornering at moderate lateral accelerations, there is an effect of the drive architecture – front-wheel-drive (FWD), rear-wheel-drive (RWD), or all-wheel-drive (AWD) – on the handling properties of the vehicle, however, since the required drive forces are small, its influence remains minor, [2]. In combined longitudinal and lateral accelerated manoeuvres, i.e. cornering under longitudinal acceleration, the tyre is typically utilised in the combined slip region. Together with the occurrence of front-to-rear weight transfer, the drive torque distribution plays a crucial role in defining the vehicle’s handling characteristics, stability properties, and combined acceleration potential. Furthermore, for automated and assisted driving, vehicle control systems should be capable of executing extreme manoeuvres, e.g., using the maximum possible lateral acceleration potential to avoid obstacles. Depending on the road surface, high sideslip manoeuvres can be beneficial to increase the vehicle’s manoeuvrability. In drifting, due to the large sideslip angles and longitudinal slips at the rear tyres, there is a strong coupling between the longitudinal and lateral tyre forces at the rear axle. Consequently, a large influence of the drive torque distribution is expected.

## 1.2. State-of-the-art

In recent years, the number of available actuators has increased through the introduction of, e.g., rear-wheel steering, semi-active and active suspension, steer-by-wire, active camber, and individual wheel drive concepts, providing new possibilities for actively influencing vehicle dynamics, [3]. Multiple actuators create the need for integrated or global chassis control strategies, allowing for enhanced exploitation of the available tyre–road friction potential, [4, 5]. Therefore, a thorough understanding of how these actuators affect vehicle

behaviour is essential for both the design of control systems and a deeper understanding of the overall system dynamics. New powertrain concepts, particularly those employing individual electric motors on the front and rear axles or even on the individual wheels, offer new possibilities to improve the vehicle's handling characteristics and stability properties effectively, [6], thereby enhancing the vehicle's driving performance for both manual and automated driving. The vehicle handling characteristics are fundamentally important for evaluating its (open-loop) stability and for assessing the vehicle's response to driver steering commands, [7–10]. From a driver's perspective, vehicle handling characteristics must provide a predictable response and enable controllability under critical driving conditions.

The potential improvement in 'agility' and manoeuvrability can enhance both vehicle safety and the capability of driver assistance systems or autonomous driving applications, [11]. Vehicle automation has become a major focus of recent research and development efforts, [12]. However, autonomous vehicles are typically characterised by a conservative driving style, and stability control systems generally restrict vehicle operation to the linear handling regime, [13, 14]. The development of driver assistance systems has so far focused on moderate handling manoeuvres such as lane keeping and lane changing, which are already implemented in production vehicles with lower levels of automation. For higher levels of automation, however, vehicle control systems must also be capable of performing manoeuvres near the limits of handling, where nonlinear system behaviour becomes dominant and strongly influences stability, controllability, and consequently safety, [15].

Operating within the nonlinear handling regime, including large vehicle sideslip angles, may be beneficial in particular situations to improve manoeuvrability, for example, to avoid obstacles, [11, 16, 17]. Previous studies [18–21] have shown that under specific road conditions, minimum-time cornering manoeuvres are characterised by large vehicle sideslip angles, and depending on the powertrain architecture, even countersteering may be advantageous. Particularly in off-road conditions, the maximum lateral acceleration is achieved at large vehicle sideslip angles, [22].

Even though the steady-state drift, i.e. the powerslide, is an unstable vehicle state, it is frequently utilised by rally drivers, particularly on loose gravel surfaces. The powerslide is defined in [23] for RWD vehicles as a steady-state cornering motion characterised by a large vehicle sideslip angle and a large steering angle, where the front wheels point to the outside of the turn, combined with large traction forces at the rear axle. The large vehicle sideslip angle and large traction forces at the rear axle lead to a strong coupling between the longitudinal and lateral tyre forces. Increasing the drive torque increases the longitudinal slip at the rear tyres, thereby reducing their lateral force. This characteristic property of the tyre can be used to stabilise the powerslide. While human drivers typically employ both steering and drive torque for stabilising the powerslide, a study of the potential of these control inputs for an RWD vehicle, [24], reveals that either the steering angle or drive torque alone is sufficient for stabilisation. Several researchers have investigated the powerslide and its stability properties. In [25, 26], the powerslide is identified as an unstable saddle-node equilibrium. In [27], periodic limit cycles were

identified after the loss of stability at the powerslide. The loss of stability at the powerslide corresponds to a monotonic loss of stability. The yaw rate of the vehicle will start to increase or decrease depending on the disturbance. From a practical perspective, the resulting trajectories of the centre of gravity (COG) and vehicle states in the time period (closely) after the loss of stability seem to be important, as the related trajectories would not be feasible with regular driving and are becoming more relevant in recent and future research, [16, 17].

A variety of control approaches have been proposed to stabilise the powerslide of an RWD vehicle using steering and drive torque inputs, [28–31]. In [32], a sliding-mode controller with drive and braking inputs at the front and rear axles, with fixed steering, is proposed for stabilising the powerslide equilibrium. Goh et al. [33] developed a controller capable of maintaining the powerslide while tracking a desired path, and later applied a model-inversion technique with wheel slip control to improve control performance, [34]. More recently, a nonlinear model predictive control approach was proposed in [35] to achieve dynamic, non-equilibrium drifting while remaining within prescribed track limits. Furthermore, for overactuated vehicles with individual wheel drives, several controllers have been developed to stabilise the powerslide, [22, 36, 37].

To analyse the lateral dynamics of a vehicle during longitudinal acceleration, a quasi-steady-state (QSS) assumption is commonly employed. This approach transforms transient driving conditions into a mechanically equivalent equilibrium, enabling the application of mathematical methods originally developed for steady-state analysis. Horiuchi et al. added a virtual external force to the equation of motion of the vehicle in the longitudinal direction to consider front-to-rear load transfer and longitudinal tyre forces in [38]. In [39], a quasi-steady-state assumption is applied, neglecting the change of the longitudinal velocity for a short period of time. In [40] and [41], it is additionally required that the derivative of the longitudinal slip of each wheel is zero, while the lateral and yaw motions satisfy the steady-state condition.

When considering cornering during longitudinal acceleration, both in driving and braking conditions, the handling characteristics and stability properties of the vehicle can change significantly, [38, 39, 42]. The stability properties are closely linked to the effective axle sideslip stiffness and, consequently, handling characteristics of the vehicle. Since traction forces can alter the effective axle sideslip stiffness, the drive architecture becomes particularly important during longitudinally accelerated cornering manoeuvres.

Klomp et al. [42] analysed the effect of different drivetrain layouts – AWD, FWD and RWD – on handling characteristics and lateral acceleration potential under longitudinal acceleration. They proposed an ‘optimal’ drive torque distribution using a quasi-steady-state assumption. Further studies on different drivetrain layouts focused on handling and yaw dynamics, [2, 43], indicating that FWD vehicles are less prone to understeer in steady-state cornering due to the additional yaw moment generated by longitudinal forces at the front axle. Using a basic two degrees of freedom (DOF) vehicle model and a simplified Magic Formula tyre model, Ono et al. [44] demonstrated that vehicle loss of stability can arise from a saddle-node/Fold bifurcation, which considerably depends on

the rear lateral tyre force saturation. A steering control strategy is proposed to stabilise the motion of the vehicle. The joint point locus approach is applied in [45] to identify system equilibrium points and assess their stability properties, considering different friction potentials at the front and rear axles. A comprehensive study on a two DOF vehicle model is done by Rossa et al. in [25], where various types of loss of stability for different combinations of effective tyre force characteristics at the front and rear axles are studied, using bifurcation analysis and phase-plane diagrams. Pauwelussen studied the influence of the nonlinear tyre force characteristics on the stability behaviour of a vehicle in [46], focusing on the appearance of limit cycles.

Several studies have investigated vehicle stability during braking manoeuvres combined with steering input. Horiuchi et al. [38] applied a quasi-steady-state assumption to model the vehicle behaviour under combined lateral and longitudinal acceleration in braking conditions. Using the steering angle as a bifurcation parameter, they identified a Fold bifurcation for a specific vehicle configuration under negative longitudinal acceleration with a fixed brake torque distribution. In [47], the stability properties are further analysed during combined braking and steering for various velocities and steering angles for a constant brake distribution. In contrast to conventional hydraulic brake systems, regenerative braking via electric motors enables a variable brake force distribution, potentially extending the combined stable longitudinal and lateral acceleration envelope.

Beyond extending the stable handling domain, an actively controlled drive torque distribution can also enhance vehicle responsiveness. A responsiveness–stability metric is introduced in [48], and a controller is proposed that adapts the drive torque distribution to prioritise either responsiveness or stability, depending on the driving condition.

### 1.3. Research scope

While previous research on the powerslide has primarily focused on RWD vehicles, limited attention has been paid to analysing the powerslide for AWD vehicles, particularly with variable drive torque distribution. Hence, the stability properties and the handling characteristics for AWD vehicles in unstable vehicle states with large sideslip angles are not yet fully resolved. A profound understanding of these interactions is crucial, particularly for the design of automation and control systems. Furthermore, the dynamic behaviour after loss of stability at the powerslide, the resulting motion and corresponding properties, remains to be explored.

The influence of a variable drive torque distribution on the vehicle’s handling characteristics and stability properties, particularly in cornering under longitudinal acceleration, has received limited attention in the literature. In combined longitudinal and lateral acceleration manoeuvres, where the tyre is typically used in the combined slip region and nonlinear effects become dominant, a thorough understanding of the interaction with variable drive torque distribution is crucial. Considering the vehicle’s acceleration potential, the influence of the powertrain topology and, consequently, the drive torque distribution becomes particularly relevant.

Considering these gaps, the following research goals are defined, summarising the key objectives of this cumulative thesis:

- Analysis of the influence of the drive torque distributions between the front and the rear axles on the powerslide steady-state conditions and corresponding stability properties.
- Study of different control strategies to stabilise the powerslide, i.e. controllability of different actuators, including steering angle, total drive torque and drive torque distribution.
- Examination of the dynamic behaviour after loss of stability at a powerslide condition for fixed controls.
- Investigation of the influence of the drive torque distribution on stability boundaries and performance limitations, and their correlation with handling characteristics at the limit of handling at combined longitudinal and lateral acceleration.
- Evaluation of an optimal drive torque distribution to maximise the stable lateral acceleration potential during longitudinal acceleration.

The remainder of this thesis is structured as follows. Section 2 provides a brief overview of the used vehicle and tyre models, followed by the presentation of the applied methods and assumptions in Section 3. The thesis consists of four publications in total. A brief summary of these papers and the contribution of the author of this dissertation is provided in Section 4. The scientific impact of this thesis is outlined in Section 5. The papers are attached in the appendix.

## 2. Modelling

In this thesis, different vehicle and tyre models are employed due to different modelling requirements. Modelling, and in particular, the choice of the appropriate model fidelity, is crucial for capturing the relevant effects and understanding complex dynamical behaviour while keeping the model as simple as possible.

### 2.1. Vehicle models

For the investigation of the powerslide, the basic two-wheel vehicle model, illustrated in Figure 1, is considered, in which the weight transfer left-to-right and front-to-rear is neglected. The front and rear substitute tyres represent the front and rear effective axle characteristics of the reference vehicle. In total, the model has five degrees of freedom: vehicle velocity  $v$ , vehicle sideslip angle  $\beta$ , yaw rate  $\dot{\psi}$  and angular velocities at the front and rear axles  $\omega_F$  and  $\omega_R$ , respectively. Although the model is rather simple, it is suitable for representing the vehicle dynamics at the powerslide, [23]. This model is applied in *Paper A* and *Paper B*. Vehicle parameters, governing equations and further information are provided in *Paper A*.

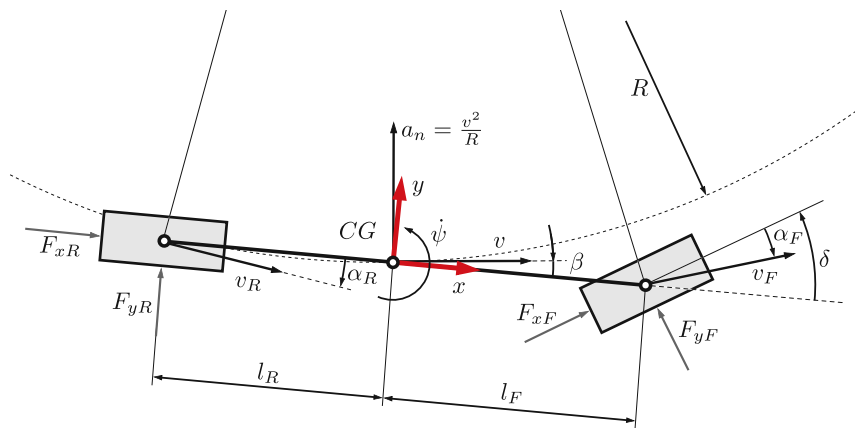


Figure 1: Illustration of the two-wheel vehicle model.

For combined accelerated manoeuvres, a more sophisticated vehicle model has to be considered to map both the ‘global’ vehicle motion and the dynamics of the individual wheels. For that purpose, a 10 degrees of freedom vehicle model is used, illustrated in Figure 2. This model enables a more precise representation of the vehicle dynamics, particularly at combined acceleration manoeuvres, incorporating weight transfer in both longitudinal and lateral directions. Modelling the dynamics of the individual wheels is essential, as the saturation of a single wheel can determine the vehicle’s performance potential and may lead to a ‘local’ loss of stability, such as spin-up of a single wheel, as well as to a ‘global’ loss of stability, affecting the yaw dynamics. This model is utilised in

*Paper C* and *Paper D*. The corresponding vehicle parameters and governing equations are provided in *Paper C*.

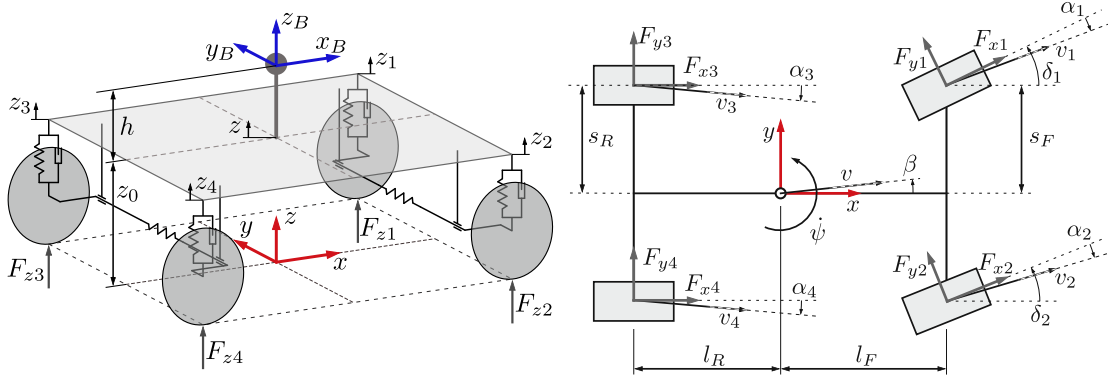


Figure 2: Schematic illustration of the 10 degrees of freedom vehicle model.

## 2.2. Tyre models

In the literature, several fundamentally different approaches exist for modelling the tyre force characteristics, ranging from purely empirical models to physical models. In empirical approaches, measurement data is approximated using mathematical functions. In contrast, physics-based models rely on fundamental physical relationships, e.g., based on the finite element method. In this thesis, two different models are employed: the brush tyre model and Magic Formula tyre model, [7].

The brush tyre model is a simplified physical model that captures the essential mechanical characteristics with only a few parameters. This model is used for the sake of simplicity in *Paper B*. It includes the mutual influence of longitudinal and lateral tyre forces in sufficient detail for the analysed vehicle states with large vehicle sideslip angles.

The Magic Formula tyre model is a semi-empirical tyre model that relies on empirically derived relationships based on measurement data and is utilised in *Paper A*, *Paper C* and *Paper D*.

The longitudinal and lateral tyre forces,  $F_{xi}$  and  $F_{yi}$ , respectively, depend on the vertical tyre force  $F_{zi}$ , the tyre sideslip angle  $\alpha_i$ , and the longitudinal slip  $s_{xi}$ . The influence of the camber angle is neglected. In Figure 3, the normalised lateral tyre forces  $F_{yi}/F_{zi,0}$  are depicted over the normalised longitudinal tyre forces  $F_{xi}/F_{zi,0}$  for constant sideslip angles  $\alpha$  and friction potential scaling representing dry asphalt, calculated with the Magic Formula tyre model.  $F_{zi,0}$  represents the nominal tyre vertical load. The characteristics of a front tyre are shown in solid lines, and the characteristics of a rear tyre are shown in dash-dotted lines. While the sideslip angle  $\alpha$  is constant, the lateral tyre force  $F_{yi}$  is reduced by increasing the longitudinal slip, illustrating the mutual influence of the two components. Since the reference vehicle has different tyre dimensions on the front and rear axles, the front and rear tyres have different cornering stiffnesses, slip stiffnesses and

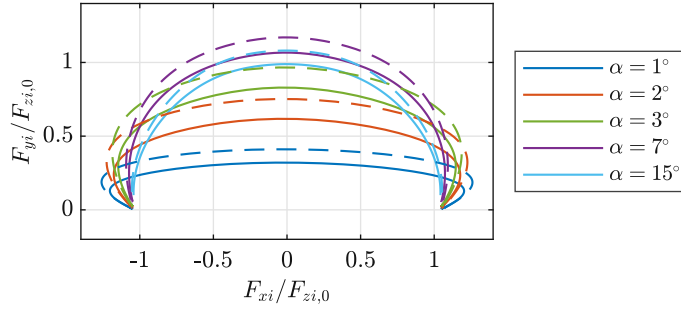


Figure 3: Magic Formula tyre model: Combined normalised tyre forces for constant sideslip angles  $\alpha$  and varied longitudinal slip  $s_x$  for a front tyre,  $i \in \{1, 2\}$  (solid lines), and a rear tyre,  $i \in \{3, 4\}$  (dash-dotted lines).

friction potentials. Examining the pure lateral tyre characteristics (i.e. the points where  $F_{xi}/F_{zi,0} = 0$  for different values of  $\alpha$  in Figure 3) shows that the cornering stiffness of the front tyres is lower than the cornering stiffness of the rear tyres. Both the maximum lateral and longitudinal friction potentials are higher at the rear tyres compared to the front tyres. With increasing longitudinal slip, the (local) cornering stiffness of the tyres decreases, significantly affecting the vehicle's handling and stability properties under combined lateral and longitudinal tyre slip conditions.

To illustrate the influence of the mutual dependence of longitudinal and lateral tyre forces on handling and stability, a vehicle state representing an accelerated cornering manoeuvre is selected as an example, and the respective tyre forces are depicted in Figure 4. The driving condition at normal acceleration  $a_n = 6 \text{ m/s}^2$  and tangential acceleration  $a_t = 5 \text{ m/s}^2$  with a drive torque distribution of  $\gamma = 0.8$ , describing the portion of the total drive torque at the rear axle  $\gamma = T_R/T_{\text{tot}}$ , is selected, considering the 10 DOF vehicle model, Figure 2. The lateral tyre forces  $F_{yi}$  are plotted over the longitudinal tyre force  $F_{xi}$ , where longitudinal tyre slips  $s_{xi}$  are varied for constant tyre sideslip angles  $\alpha_i$  and vertical tyre forces  $F_{zi}$  for the tyres  $i = 1 - 4$ . The corresponding tyre forces for  $\gamma = 0.8$

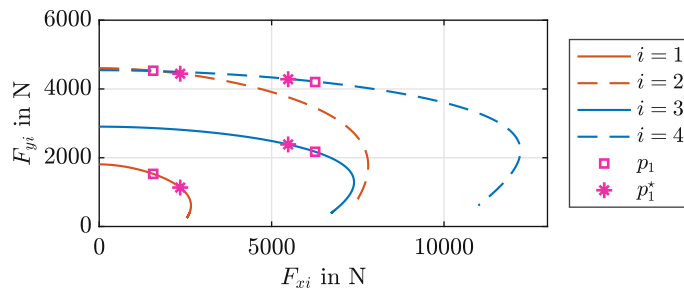


Figure 4: Tyre forces  $F_{yi}$  over  $F_{xi}$  for constant tyre slip angles  $\alpha_i$  for a vehicle normal acceleration  $a_n = 6 \text{ m/s}^2$  and tangential acceleration  $a_t = 5 \text{ m/s}^2$  and  $\gamma = 0.8$  ( $p_1$ ) and for the changed drive torque distribution  $\gamma = 0.7$  ( $p_1^*$ ).

are marked with a magenta square and denoted  $p_1$ . Changing the drive torque distribution from  $\gamma = 0.8$  to  $\gamma = 0.7$  and keeping  $\alpha_i$  and  $F_{z_i}$  constant, results in tyre forces marked with a magenta star denoted  $p_1^*$ . At  $p_1$  and  $p_1^*$ , the longitudinal tyre forces  $F_{x_i}$  of one axle are equal due to the open differential gears. The change of the drive torque distribution to  $\gamma = 0.7$  ( $p_1^*$ ) increases the longitudinal tyre forces at the front axle ( $F_{x_1}$  and  $F_{x_2}$ ) and correspondingly decreases the longitudinal tyre forces at the rear axle ( $F_{x_3}$  and  $F_{x_4}$ ). It is observed that the lateral tyre forces at the front axle ( $F_{y_1} + F_{y_2}$ ) decrease, while the lateral tyre forces at the rear axle ( $F_{y_3} + F_{y_4}$ ) increase. A yaw moment will be generated, and the corresponding modification of the effective axle sideslip stiffness will result in a change in the handling characteristics and stability properties. This example illustrates the importance of a sufficiently accurate tyre force model.

### 3. Methods and assumptions

The primary focus of this thesis is on the theoretical analysis of the system. The influence of the drive torque distribution on the steady-state and quasi-steady-state conditions of the vehicle, as well as its corresponding stability properties, is investigated. For this purpose, methods like bifurcation analysis and continuation algorithm, stability and modal analysis, controllability analysis, and quasi-steady-state assumption are utilised. Furthermore, methods to analyse the vehicle handling properties and performance potential are employed. This section provides a brief overview of these methods and refers to the corresponding publications.

#### 3.1. Bifurcation analysis and continuation algorithm

Bifurcation analysis in general refers to the study of changes in the structure or stability of the solutions of a system as parameters are varied, [49–52]. To conduct a bifurcation analysis, the system to be investigated is described by the dynamics equation

$$\dot{\mathbf{x}}(t) = \mathbf{f}(\mathbf{x}, \mathbf{p}) \quad (1)$$

where  $\mathbf{x}$  represents the state vector of the vehicle model and  $\mathbf{p}$  is the vector of parameters. The parameter vector is split into a distinguished parameter  $\lambda$ , e.g. the drive torque distribution  $\gamma$ , and free and fixed parameters  $\mathbf{p}_{\text{free}}$  and  $\mathbf{p}_{\text{fixed}}$ , respectively.

Different (steady-state or quasi-steady-state) driving conditions shall be investigated for a constant vehicle velocity or constant radius of curvature for a varied distinguished parameter. Therefore, constraint equations  $\mathbf{g}(\mathbf{x}, \mathbf{p}) = \mathbf{0}$  are employed, and the augmented set of equations reads as follows:

$$\dot{\mathbf{x}}(t) = \mathbf{f}(\mathbf{x}, \mathbf{p}), \quad \mathbf{g}(\mathbf{x}, \mathbf{p}) = \mathbf{0}. \quad (2)$$

where

$$\mathbf{g}(\mathbf{x}, \mathbf{p}) = \begin{bmatrix} \mathbf{x}_k - \mathbf{x}_{k,0} \\ \mathbf{p}_l - \mathbf{p}_{\text{fixed}} \end{bmatrix} \quad (3)$$

with the indices  $k$  of the fixed states and  $l$  of the fixed parameters. If more states shall be fixed, a respective number of fixed parameters from  $\mathbf{p}_{\text{fixed}}$  must be incorporated into  $\mathbf{p}_{\text{free}}$ .

To track solution paths of bifurcation points (e.g. Hopf, Fold and Takens–Bogdanov bifurcations), additional constraint equations related to the respective type of bifurcation, [49–52], have to be considered. Depending on the codimension of the corresponding bifurcation [49], the respective number of fixed parameters has to be set free.

To calculate a solution branch and analyse the corresponding properties, a path continuation algorithm is utilised. Starting at a found solution, the algorithm tracks the solution path by ‘tangential continuation’, utilising the current and prior found solutions to make an initial guess for the next solution step, [50], while varying a distinguished parameter.

This method is used in *Paper A*, *Paper B*, *Paper C* and *Paper D*.

### 3.2. Stability of first order and modal analysis

Once a steady-state or quasi-steady-state solution of the nonlinear system is found, the nonlinear equations of motion are linearised w.r.t. this solution,  $\Delta \dot{\mathbf{x}} = \mathbf{A} \Delta \mathbf{x} + \mathbf{B} \Delta \mathbf{u}$  with system matrix  $\mathbf{A}$  and input matrix  $\mathbf{B}$ .  $\Delta \mathbf{x} = \mathbf{x} - \mathbf{x}_0$  represents the deviation of the state vector and  $\Delta \mathbf{u} = \mathbf{u} - \mathbf{u}_0$  the deviation of the input vector from the analysed (quasi-)steady-state solution, indicated by index 0. By solving the eigenvalue problem  $\mathbf{A} \mathbf{p}_i = \lambda_i \mathbf{p}_i$ , with eigenvalue  $\lambda_i$  and eigenvector  $\mathbf{p}_i$  corresponding to mode  $i$ , the local dynamic behaviour and stability of the steady-state solutions may be analysed. The eigenvalue  $\lambda_i$  provides information about the dynamic behaviour of mode  $i$  (exponential or oscillatory behaviour), while the respective eigenvector  $\mathbf{p}_i$  describes the mode shape and consequently the contributions of the individual states to this mode.

Lyapunov's first method implies that a steady-state solution is stable if all eigenvalues of  $\mathbf{A}$  have negative real parts, [49]. If one or more eigenvalues have a positive real part, the steady-state is unstable. If one or more eigenvalues have a zero real part while all the other eigenvalues have a negative real part, the steady-state is at the stability boundary. The configuration and number of the eigenvalues with zero real part determine the type of bifurcation emerging from this solution.

This method is used in *Paper A*, *Paper B*, *Paper C* and *Paper D*.

### 3.3. Controllability analysis

To analyse the effectiveness of different inputs to control an unstable system state, a modal controllability analysis provides insights into how a mode is affected by a specific input. The modal observability measure provides information on how a mode is visible from a specific output of the locally linearised system model. These measures and their combination were introduced by Hamdan et al. in [53]. Choi et al. applied a modified version in [54] by taking the length of the input vector  $|\mathbf{b}_j|$  of input  $j$  into account. The measure is further extended in *Paper A* by considering the range of operation of each actuator by scaling the modal controllability measure with the maximum input of the actuator.

The subsequent measure of modal controllability of mode  $i$  with input  $j$  is the cosine of the angle between the left eigenvector  $\mathbf{q}_i$  (from  $\mathbf{A}^T \mathbf{q}_i = \lambda_i \mathbf{q}_i$ ) and input vector  $\mathbf{b}_j$  scaled with the length of the input vector  $|\mathbf{b}_j|$  and the maximum input  $u_{j,\max}$  of actuator  $j$ . This measure can be interpreted as the projection of the input vector  $\mathbf{b}_j$  on the left eigenvector  $\mathbf{q}_i$  normalised to length 1, scaled with  $u_{j,\max}$  and yields

$$M_{c,ij} = \cos \theta_{ij} |\mathbf{b}_j| u_{j,\max} \quad \text{with} \quad \cos \theta_{ij} = \frac{\mathbf{q}_i^T \mathbf{b}_j}{|\mathbf{q}_i| |\mathbf{b}_j|}. \quad (4)$$

As a measure for the modal observability of mode  $i$  from output  $k$ , the projection of the

right eigenvector  $\mathbf{p}_i$  on the output vector  $\mathbf{c}_k$  is applied,

$$M_{o,ki} = \cos \theta_{ki} |\mathbf{c}_k| \quad \text{with} \quad \cos \theta_{ki} = \frac{\mathbf{c}_k \mathbf{p}_i}{|\mathbf{p}_i| |\mathbf{c}_k|}. \quad (5)$$

The product of these two measures,  $M_{co,jk} = M_{o,ki} M_{c,ij}$ , provides insight into the effectiveness of specific input-output combinations in controlling a specific mode.

This method is applied in *Paper A*.

### 3.4. Quasi-steady-state assumption

To analyse the influence of the drive torque distribution  $\gamma$  on the stability properties of the vehicle during manoeuvres with combined lateral and longitudinal acceleration, the transient vehicle state  $a_n \neq 0$  and  $a_t \neq 0$ , with normal acceleration  $a_n$  and tangential acceleration  $a_t$ , is transformed to a quasi-steady-state that approximates the transient condition well, [38, 40–42].

In *Paper C* and *Paper D*, a similar approach to Horiuchi et al. [38] is used, where an equivalent longitudinal force is applied in the vehicle's longitudinal axis at the centre of gravity to transform the transient state during acceleration and braking into an equivalent equilibrium state. In this thesis, the derivative of the vehicle velocity,  $\dot{v}$ , is set to the desired tangential acceleration  $a_t$ . This is equivalent to applying an inertial force acting at the centre of gravity of the vehicle in the opposite direction of the velocity  $v$ . As a result, both the vertical load transfer and the longitudinal tyre forces required to achieve the desired tangential acceleration  $a_t$  are taken into account, allowing the accelerated vehicle state to be treated as a steady-state condition. The yaw acceleration  $\ddot{\psi}$ , the derivative of the vehicle sideslip angle  $\dot{\beta}$ , and the derivatives of the other states are set to zero to satisfy the steady-state condition.

### 3.5. Nonlinear handling diagram under longitudinal acceleration

The handling diagram offers fundamental insights into the vehicle's handling properties. It allows for visualising and analysing the handling characteristics of a vehicle. The evolutions of steering angle and vehicle sideslip angle are plotted over the lateral or normal acceleration under steady-state conditions. The handling diagram provides numerous information about the vehicle, such as steering characteristics, i.e. understeer, neutral-steer and oversteer behaviour, differences in cornering stiffness between the front and rear axles, and stability properties of the vehicle. Reaching the limit of handling, near the maximum possible lateral acceleration, where nonlinear behaviour becomes dominant, the handling behaviour can be distinguished between final understeer and final oversteer behaviour, depending on whether the steering angle increases or decreases, respectively.

The handling diagram is also employed in experimental testing and simulation to assess and compare vehicles or setup configurations. There are different approaches to generate the handling diagram in an experimental setup: either the vehicle velocity is kept constant and the steering angle is increased, denoted as the *ramp-steer-test*, or the radius

of curvature is kept constant while increasing the velocity and simultaneously adjusting the steering angle to track the desired circular path.

Regarding the handling characteristics under longitudinal acceleration, the steering behaviour and stability properties of the vehicle may change significantly. Since steady-state conditions are assumed in the handling diagram, the quasi-steady-state assumption is applied to the studied vehicle model. To illustrate the potential insights that can be derived from the handling diagram, this diagram is plotted in Figure 5 for the vehicle model parameter considered in this thesis.

While the analysed vehicle shows final understeer characteristics at steady-state cornering for both  $\gamma = 0$  (FWD configuration) and  $\gamma = 1$  (RWD configuration), an increase of the vehicle tangential acceleration  $a_t$  results in a qualitative change in the handling characteristics of the vehicle with the RWD configuration. The handling diagram in Figure 5 is derived for a constant tangential acceleration  $a_t = 4 \text{ m/s}^2$ . It can be observed that the handling characteristics change to final oversteer behaviour for the RWD vehicle ( $\gamma = 1$ ), blue line. In contrast, for an AWD configuration with a considerable portion of the total drive torque  $T_{\text{tot}}$  at the front axle, e.g.  $\gamma = 0.7$ , the final understeer characteristics are maintained, green line.

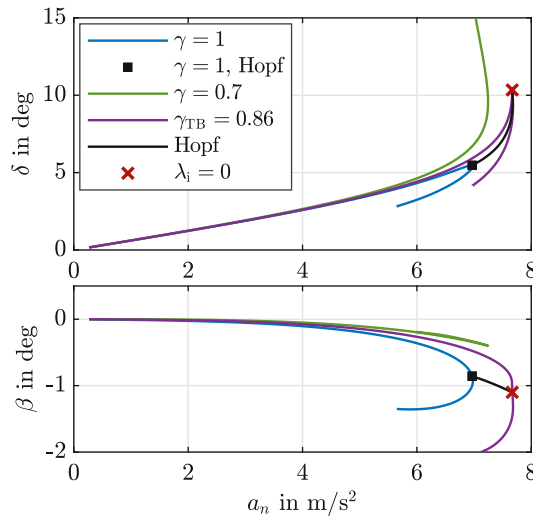


Figure 5: Steering angle  $\delta$  and vehicle sideslip angle  $\beta$  for different drive torque distributions  $\gamma$  plotted over the normal acceleration  $a_n$ . Quasi-steady-state solutions for tangential acceleration  $a_t = 4 \text{ m/s}^2$  and constant velocity  $v = 20 \text{ m/s}$ .

Evaluating the eigenvalues of the  $\gamma = 1$  branch to assess stability properties, a Hopf-type loss of stability is identified close to the maximum normal acceleration  $a_n \approx 7 \text{ m/s}^2$ , marked with a black square in Figure 5. The solution of the Hopf branch, black line, is calculated for constant tangential acceleration  $a_t = 4 \text{ m/s}^2$  and varied drive torque distribution  $\gamma$ . With decreasing drive torque distribution  $\gamma$ , the Hopf point, starting at the black square with  $\gamma = 1$ , moves to higher normal accelerations  $a_n$ , black line, until

the imaginary part of the Hopf eigenvalue  $\lambda_i$  approaches zero, indicated by the red  $\times$ . For  $\lambda_i = 0$ , a bifurcation occurs, characterised by a double zero eigenvalue, known as the Takens–Bogdanov bifurcation. This point, with  $\gamma_{TB} = 0.86$ , defines the drive torque distribution to achieve the maximum possible stable quasi-steady-state driving condition. The corresponding handling curve is depicted in Figure 5, purple line. A further decrease of the drive torque distribution results in final understeer handling characteristics of the vehicle.

The handling diagram is used in *Paper A*, *Paper B*, *Paper C*, and *Paper D*.

### 3.6. GG diagram

The GG diagram, also called acceleration envelope, is a graphical representation of the combined longitudinal and lateral acceleration potential of the vehicle. It is often used in vehicle dynamics to visualise the acceleration limits and performance boundaries under simultaneous braking/acceleration and cornering. Hence, it is a very suitable and frequently employed method for comparing the combined acceleration potential of different powertrain topologies.

Considering the results from the handling diagram Figure 5, it becomes obvious that the Takens–Bogdanov point, red  $\times$ , represents a driving condition near the maximum attainable normal acceleration  $a_n$  of the vehicle for a given tangential acceleration  $a_t$ . Moreover, it defines the maximum normal acceleration  $a_n$  of stable steady-state driving conditions in the vehicle handling characteristics for the drive torque distribution  $\gamma_{TB}$ . Hence, by varying the tangential acceleration  $a_t$ , the corresponding normal acceleration  $a_n$  at the Takens–Bogdanov points defines the stable GG envelope of the vehicle.

In Figure 6, the GG envelope is plotted w.r.t. the longitudinal and lateral acceleration of the vehicle,  $a_x$  and  $a_y$ , respectively, as is typical for a GG diagram, [55]. Since this diagram is symmetrical w.r.t. the abscissa, it is plotted and discussed for  $a_y \geq 0 \text{ m/s}^2$  only in the following.

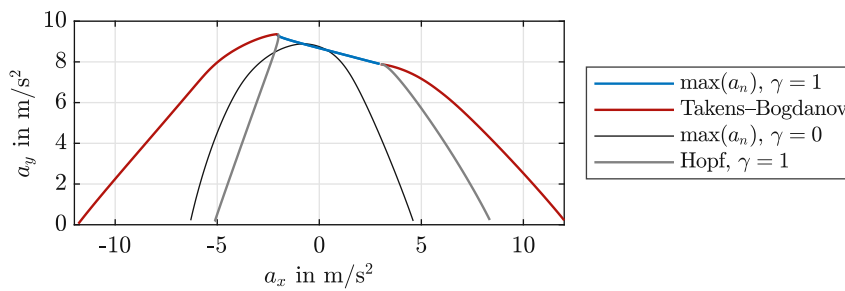


Figure 6: Takens–Bogdanov and Hopf branches in the GG diagram.

At longitudinal accelerations  $a_x \approx 3 \text{ m/s}^2$  to  $12 \text{ m/s}^2$  and decelerations  $a_x \approx -2 \text{ m/s}^2$  to  $-12 \text{ m/s}^2$ , Takens–Bogdanov branches exist and are plotted in red colour. Between  $a_x \approx -2 \text{ m/s}^2$  and  $a_x \approx 3 \text{ m/s}^2$ , the vehicle exhibits final understeer behaviour for several

drive torque distributions  $\gamma$ , where the maximum attainable normal accelerations  $a_y$  for  $\gamma = 1$  is depicted in Figure 6, blue colour.

At  $a_x \approx 3 \text{ m/s}^2$ , besides the Takens–Bogdanov branch, also a Hopf bifurcation emerges, both for a drive torque distribution of  $\gamma = 1$ , and similar at  $a_x \approx -2 \text{ m/s}^2$ . Beyond longitudinal accelerations  $a_x \approx 3 \text{ m/s}^2$ , the Hopf branch for  $\gamma = 1$  (grey solid line in Figure 6) limits the ‘stable’ area of combined accelerations for the RWD configuration, similarly for negative  $a_x$ .

The black line in Figure 6 shows the maximum attainable combined lateral and longitudinal accelerations for drive and brake forces applied at the front axle only ( $\gamma = 0$ ). It can be observed that in the acceleration case,  $a_x > 0$ , the configuration with  $\gamma = 1$  is superior compared to  $\gamma = 0$  considering the GG envelope, with the opposite in the deceleration case. However, the (stable) GG envelope for both  $\gamma = 1$  and  $\gamma = 0$  is considerably smaller compared to the Takens–Bogdanov configuration.

This method is used in *Paper C* and *Paper D*.

## 4. Summary of the articles

### Paper A

*Insights into stability and control of the powerslide motion with variable drive torque distribution - applied to a driver assistance system*

Manuel Eberhart, Manfred Plöchl,  
Michael Unterreiner, Johannes Edelmann

Vehicle System Dynamics  
<https://doi.org/10.1080/00423114.2025.2457433>

The characteristic properties of the powerslide motion for an all-wheel drive (electric) vehicle with individual motors at the front and rear axles are investigated. The change in handling and stability properties due to variations in the drive torque distribution is analysed and discussed.

The controllability analysis indicates that the drive torque distribution is an effective control input for stabilisation and can be superior to the total drive torque input. The powerslide cannot be stabilised for particular conditions with the total drive torque input at a fixed drive torque distribution. Depending on the (nominal) drive torque distribution, the control strategy has to be changed from an ‘RWD-strategy’ to an ‘AWD-strategy’. The loss of controllability of the unstable powerslide mode with the total drive torque input indicates the (constant) drive torque distribution, where the strategy has to be changed.

Based on these findings, a driver assistance system is presented that allows the human driver to track a desired circular path solely by steering commands. The powerslide motion is stabilised by a controller acting on the total drive torque and on the drive torque distribution. The characteristics, limitations in dynamics and reactions of a human driver are considered by introducing a virtual test driver model in a simulation environment. The successfully stabilised powerslide is shown in simulation with a basic vehicle model and in an experimental setup with a test vehicle.

*Manuel Eberhart is responsible for:* writing of the original draft; derivation of the model equations; calculation of steady-states and theoretical system analysis; simulation and experiments; visualisation and presentation of the results.

### Paper B

*Post-critical behaviour of the powerslide motion*

Johannes Edelmann, Manuel Eberhart,  
Alois Steindl, Manfred Plöchl

Vehicle System Dynamics  
<https://doi.org/10.1080/00423114.2025.2471346>

In this study, the post-critical behaviour after loss of stability of a vehicle in powerslide motion is given attention. The loss of stability of a vehicle in powerslide motion is of monotonic nature. The yaw rate of the vehicle will start to increase or decrease depending on the disturbance. Then, there will be a transition from the powerslide equilibrium to another equilibrium for the same fixed controls. For very large (negative) steering angles, this equilibrium may be stable, and the vehicle will end in steady-state cornering with a typically small radius and different states compared to the corresponding steady-state

cornering in powerslide condition. For smaller steering angles, the equilibrium will be unstable and of oscillatory nature and a respective Hopf bifurcation is found. The resulting stable limit cycles of the vehicle states appear as flower-like trajectories on the road plane, where the centre of gravity (COG) of the vehicle spirals around a fixed point.

The findings in this paper build on theoretical research, but evidence from practical observations and vehicle test runs suggests the plausibility of the results. From a practical application point of view, trajectories of the COG and vehicle states in the time period (closely) after the loss of stability seem to be most important, as the related trajectories are not feasible with regular driving, [16].

*Manuel Eberhart is responsible for:* calculation of steady-states and theoretical system analysis; performing simulations; conducting experiments; visualisation of the results.

## Paper C

### *Stability boundaries and bifurcation analysis of an AWD vehicle: the influence of the drive torque distribution*

Manuel Eberhart, Manfred Plöchl,  
Johannes Edelmann

Nonlinear Dynamics  
<https://doi.org/10.1007/s11071-025-11232-x>

In this paper, the impact of the drive torque distribution between the front axle and rear axle of an AWD vehicle on its combined lateral and longitudinal handling envelope, as well as on respective stability properties, is investigated. To analyse manoeuvres at combined longitudinal and lateral accelerations, a quasi-steady-state assumption is used to apply bifurcation and continuation techniques. Regarding the critical mode shapes, a rather detailed vehicle and tyre model is considered in a simulation study on the stability properties of a vehicle at the limits of handling in regular driving to map both the ‘global’ vehicle motion and the dynamics of the individual wheels.

Stability analysis for quasi-steady-state handling manoeuvres reveals different types of stability loss. The Takens–Bogdanov bifurcations appear at the limits of handling and characterise the change from final oversteer to final understeer behaviour. Corresponding Hopf and Fold bifurcations are found that define limits for practically reasonable drive torque distributions. The drive torque distributions at the Takens–Bogdanov branch determine the transition from a Hopf to a Fold bifurcation. Two distinct Fold surfaces are identified that are related to the tyre operating conditions at the corresponding Takens–Bogdanov bifurcations. These Fold surfaces exhibit different characteristic types of loss of stability, where one of these surfaces is considered to be of practical relevance.

*Manuel Eberhart is responsible for:* writing of the original draft; derivation of the model equations; stability and bifurcation analysis; visualisation and presentation of the results.

## Paper D

### *Influence of the Front-Rear Torque Distribution on the Handling Characteristics and Stability Boundaries of an AWD-Vehicle*

Manuel Eberhart, Martin Arndt,  
Johannes Edelmann, Manfred Plöchl

16th International Symposium on Advanced Vehicle  
Control

[https://doi.org/10.1007/978-3-031-70392-8\\_29](https://doi.org/10.1007/978-3-031-70392-8_29)

The Takens–Bogdanov solution branch is shown to be a reasonable design criterion for the drive torque distribution of an AWD vehicle, since almost the maximum normal acceleration for a given longitudinal acceleration (or an equivalent drive torque demand) may be achieved without ‘early’ final understeer or final oversteer behaviour. The acceleration envelope defined by Takens–Bogdanov solution is compared to the acceleration envelope found with optimisation technique. In contrast to the latter, which includes unstable solutions, the Takens–Bogdanov solution branch may be of more practical relevance, since the solutions are stable. Exemplary solutions from both the Takens–Bogdanov solution branch and the optimal solution are compared, together with their corresponding handling characteristics.

*Manuel Eberhart is responsible for:* writing of the original draft; derivation of the model equations; stability and bifurcation analysis; performing simulations; visualisation and presentation of the results.

## 5. Scientific impact

Within this cumulative thesis, the effect of the drive torque distribution on vehicle handling characteristics and stability properties is investigated. It is observed that the drive torque distribution can significantly change the handling characteristics and stability properties. A variable drive torque distribution offers the potential to ‘stabilise’ or ‘agilise’ the vehicle and is essential for the full exploitation of the combined acceleration potential.

The scientific novelties of the conducted research may be summarised as follows:

- For the powerslide, it is shown that the drive torque distribution is a proper actuator to stabilise the unstable motion. The influence of the drive torque distribution on the possible steady-states was studied, showing that the handling characteristics undergo qualitative changes. In contrast to RWD vehicles, counter-steering may not be required to maintain a steady-state powerslide for AWD vehicles. Considering a given vehicle sideslip angle  $\beta$ , up to three powerslide equilibria can be identified for a constant drive torque distribution  $\gamma$ , each associated with different steering angles  $\delta$ . See [Paper A](#).
- The controllability analysis of different system inputs reveals that the baseline drive torque distribution is essential for stabilising the powerslide with the total drive torque. Depending on the drive train configurations, a qualitative change in control strategy between the ‘RWD-strategy’ and the ‘AWD-strategy’ may be required. This theoretical observation also coincides with anecdotal knowledge from expert drivers. See [Paper A](#).
- The post-critical behaviour after loss of stability at the powerslide is studied. There will be a transition from the powerslide equilibrium to another equilibrium for the same fixed controls. The vehicle motion converges to either a stable equilibrium with a considerably smaller radius of curvature or to a stable limit cycle orbiting an unstable equilibrium. See [Paper B](#).
- The impact of the drive torque distribution of an AWD vehicle during combined lateral and longitudinal acceleration on the handling characteristics and stability properties is investigated. The Takens–Bogdanov bifurcation at the limits of handling is identified, characterising the transition from final oversteer to final understeer characteristics, and corresponding Hopf and Fold bifurcations are identified. See [Paper C](#).
- The Takens–Bogdanov solution branch is shown to be a reasonable design criterion for a baseline drive torque distribution of an AWD vehicle to exploit the full acceleration potential of the vehicle. The Takens–Bogdanov solution branch was compared to a GG-envelope derived from optimisation. The solutions are quite similar, but in contrast to the latter, which includes unstable solutions, the Takens–Bogdanov solution branch may be of more practical relevance, since the solutions correspond to stable conditions. See [Paper D](#).

## References

- [1] L. D. Novellis, A. Sorniotti and P. Gruber. Design and comparison of the handling performance of different electric vehicle layouts. *Proceedings of the Institution of Mechanical Engineers, Part D: Journal of Automobile Engineering* 228.2 (2014), 218–232. DOI: [10.1177/0954407013506569](https://doi.org/10.1177/0954407013506569).
- [2] B. Lenzo et al. On the handling performance of a vehicle with different front-to-rear wheel torque distributions. *Vehicle System Dynamics* 57.11 (2019), 1685–1704. DOI: [10.1080/00423114.2018.1546013](https://doi.org/10.1080/00423114.2018.1546013).
- [3] M. Ploechl, P. Lugner and J. Edelmann. Basics of Longitudinal and Lateral Vehicle Dynamics. *Road and Off-Road Vehicle System Dynamics Handbook*. Ed. by G. Mastinu and M. Ploechl. Boca Raton: CRC Press, 2014, 971–1021. DOI: [10.1201/b15560](https://doi.org/10.1201/b15560).
- [4] V. Mazzilli et al. Integrated chassis control: Classification, analysis and future trends. *Annual Reviews in Control* 51 (2021), 172–205. DOI: <https://doi.org/10.1016/j.arcontrol.2021.01.005>.
- [5] P. Mandl, J. Edelmann and M. Plöchl. Vehicle Motion Control for Overactuated Vehicles to Enhance Controllability and Path Tracking. *Applied Sciences* 14.22 (2024). DOI: [10.3390/app142210718](https://doi.org/10.3390/app142210718).
- [6] L. De Novellis, A. Sorniotti and P. Gruber. Wheel Torque Distribution Criteria for Electric Vehicles With Torque-Vectoring Differentials. *IEEE Transactions on Vehicular Technology* 63.4 (2014), 1593–1602. DOI: [10.1109/TVT.2013.2289371](https://doi.org/10.1109/TVT.2013.2289371).
- [7] H. Pacejka. Tire and vehicle dynamics. 2nd ed. Oxford: Elsevier, 2005.
- [8] H. B. Pacejka. Simplified Analysis of Steady-state Turning Behaviour of Motor Vehicles. Part 1. Handling Diagrams of Simple Systems. *Vehicle System Dynamics* 2.3 (1973), 161–172. DOI: [10.1080/00423117308968439](https://doi.org/10.1080/00423117308968439).
- [9] H. B. Pacejka. Simplified Analysis of Steady-State Turning Behaviour of Motor Vehicles Part 2: Stability of the Steady-State Turn. *Vehicle System Dynamics* 2.4 (1973), 173–183. DOI: [10.1080/00423117308968440](https://doi.org/10.1080/00423117308968440).
- [10] H. B. Pacejka. Simplified Analysis of Steady-State Turning Behaviour of Motor Vehicles Part 3: More Elaborate Systems. *Vehicle System Dynamics* 2.4 (1973), 185–204. DOI: [10.1080/00423117308968441](https://doi.org/10.1080/00423117308968441).
- [11] M. Acosta, S. Kanarachos and M. Blundell. Vehicle agile maneuvering: From rally drivers to a finite state machine approach. *2016 IEEE Symposium Series on Computational Intelligence (SSCI)*. 2016, 1–8. DOI: [10.1109/SSCI.2016.7850095](https://doi.org/10.1109/SSCI.2016.7850095).
- [12] T. Ersal et al. Connected and automated road vehicles: state of the art and future challenges. *Vehicle System Dynamics* 58.5 (2020), 672–704. DOI: [10.1080/00423114.2020.1741652](https://doi.org/10.1080/00423114.2020.1741652).

- [13] Y. Chen et al. Path Tracking and Handling Stability Control Strategy With Collision Avoidance for the Autonomous Vehicle Under Extreme Conditions. *IEEE Transactions on Vehicular Technology* 69.12 (2020), 14602–14617. DOI: [10.1109/TVT.2020.3031661](https://doi.org/10.1109/TVT.2020.3031661).
- [14] Y. Yasui et al. Improvement of Vehicle Directional Stability for Transient Steering Maneuvers Using Active Brake Control. *International Congress & Exposition*. SAE International, 1996. DOI: [10.4271/960485](https://doi.org/10.4271/960485).
- [15] Z. Zhu et al. A Survey of Lateral Stability Criterion and Control Application for Autonomous Vehicles. *IEEE Transactions on Intelligent Transportation Systems* 24.10 (2023), 10382–10399. DOI: [10.1109/TITS.2023.3280200](https://doi.org/10.1109/TITS.2023.3280200).
- [16] P. Stano et al. Enhanced Active Safety Through Integrated Autonomous Drifting and Direct Yaw Moment Control via Nonlinear Model Predictive Control. *IEEE Transactions on Intelligent Vehicles* 9.2 (2024), 4172–4190. DOI: [10.1109/TIV.2023.3340992](https://doi.org/10.1109/TIV.2023.3340992).
- [17] T. Zhao et al. Collision Avoidance with Transitional Drift Control. *2021 IEEE International Intelligent Transportation Systems Conference (ITSC)*. 2021, 907–914. DOI: [10.1109/ITSC48978.2021.9564496](https://doi.org/10.1109/ITSC48978.2021.9564496).
- [18] D. Tavernini et al. Minimum time cornering: the effect of road surface and car transmission layout. *Vehicle System Dynamics* 51.10 (2013), 1533–1547. DOI: [10.1080/00423114.2013.813557](https://doi.org/10.1080/00423114.2013.813557).
- [19] K. Berntorp et al. Models and methodology for optimal vehicle maneuvers applied to a hairpin turn. *2013 American Control Conference*. 2013, 2139–2146. DOI: [10.1109/ACC.2013.6580152](https://doi.org/10.1109/ACC.2013.6580152).
- [20] B. Olofsson et al. An Investigation of Optimal Vehicle Maneuvers for Different Road Conditions. *IFAC Proceedings Volumes* 46.21 (2013), 66–71. DOI: [10.3182/20130904-4-JP-2042.00007](https://doi.org/10.3182/20130904-4-JP-2042.00007).
- [21] E. Velenis, P. Tsiotras and J. Lu. Modeling aggressive maneuvers on loose surfaces: The cases of Trail-Braking and Pendulum-Turn. *2007 European Control Conference (ECC)*. Kos: IEEE, 2007, 1233–1240. DOI: [10.23919/ECC.2007.7068670](https://doi.org/10.23919/ECC.2007.7068670).
- [22] M. Acosta, S. Kanarachos and M. E. Fitzpatrick. On full MAGV lateral dynamics exploitation: Autonomous drift control. *2018 IEEE 15th International Workshop on Advanced Motion Control (AMC)*. Tokyo: IEEE, 2018, 529–534. DOI: [10.1109/AMC.2019.8371149](https://doi.org/10.1109/AMC.2019.8371149).
- [23] J. Edelmann and M. Plöchl. Handling characteristics and stability of the steady-state powerslide motion of an automobile. *Regular and Chaotic Dynamics* 14.6 (2009), 682–692. DOI: [10.1134/S1560354709060069](https://doi.org/10.1134/S1560354709060069).
- [24] J. Edelmann and M. Plöchl. Controllability of the powerslide motion of vehicles with different drive concepts. *Procedia Engineering* 199 (2017), 3266–3271. DOI: [10.1016/j.proeng.2017.09.357](https://doi.org/10.1016/j.proeng.2017.09.357).

- [25] F. Della Rossa, G. Mastinu and C. Piccardi. Bifurcation analysis of an automobile model negotiating a curve. *Vehicle System Dynamics* 50.10 (2012), 1539–1562. DOI: [10.1080/00423114.2012.679621](https://doi.org/10.1080/00423114.2012.679621).
- [26] R. Y. Hindiyeh and J. C. Gerdes. Equilibrium analysis of drifting vehicles for control design. *Dynamic Systems and Control Conference*. Vol. 48920. 2009, 181–188. DOI: [10.1115/DSCC2009-2626](https://doi.org/10.1115/DSCC2009-2626).
- [27] A. Steindl, J. Edelmann and M. Plöchl. Influence of Tyre Characteristics on Periodic Motions for an Understeering Vehicle. *PAMM* 22.1 (2023), e202200289. DOI: [10.1002/pamm.202200289](https://doi.org/10.1002/pamm.202200289).
- [28] E. Velenis et al. Steady-state drifting stabilization of RWD vehicles. *Control Engineering Practice* 19.11 (2011), 1363–1376. DOI: [10.1016/j.conengprac.2011.07.010](https://doi.org/10.1016/j.conengprac.2011.07.010).
- [29] M. Werling, P. Reinisch and L. Gröll. Robust power-slide control for a production vehicle. *International Journal of Vehicle Autonomous Systems* 13.1 (2015), 27–42. DOI: [10.1504/IJVAS.2015.070727](https://doi.org/10.1504/IJVAS.2015.070727).
- [30] R. Chaichaowarat and W. Wannasuphoprasit. Optimal Control for Steady State Drifting of RWD Vehicle. *IFAC Proceedings Volumes* 46.21 (2013), 824–830. DOI: [10.3182/20130904-4-JP-2042.00055](https://doi.org/10.3182/20130904-4-JP-2042.00055).
- [31] R. Y. Hindiyeh and J. C. Gerdes. Design of a dynamic surface controller for vehicle sideslip angle during autonomous drifting. *IFAC Proceedings Volumes* 43.7 (2010), 560–565. DOI: [10.3182/20100712-3-DE-2013.00160](https://doi.org/10.3182/20100712-3-DE-2013.00160).
- [32] E. Velenis, E. Frazzoli and P. Tsiotras. Steady-state cornering equilibria and stabilisation for a vehicle during extreme operating conditions. *International Journal of Vehicle Autonomous Systems* 8.2-4 (2010), 217–241. DOI: [10.1504/IJVAS.2010.035797](https://doi.org/10.1504/IJVAS.2010.035797).
- [33] J. Y. Goh and J. C. Gerdes. Simultaneous stabilization and tracking of basic automobile drifting trajectories. *2016 IEEE Intelligent Vehicles Symposium (IV)*. 2016, 597–602. DOI: [10.1109/IVS.2016.7535448](https://doi.org/10.1109/IVS.2016.7535448).
- [34] J. Y. Goh, T. Goel and J. Christian Gerdes. Toward Automated Vehicle Control Beyond the Stability Limits: Drifting Along a General Path. *Journal of Dynamic Systems, Measurement, and Control* 142.2 (2019), 021004. DOI: [10.1115/1.4045320](https://doi.org/10.1115/1.4045320).
- [35] J. Y. Goh et al. Beyond the stable handling limits: nonlinear model predictive control for highly transient autonomous drifting. *Vehicle System Dynamics* 62.10 (2024), 2590–2613. DOI: [10.1080/00423114.2023.2297799](https://doi.org/10.1080/00423114.2023.2297799).
- [36] X. Hou et al. Autonomous drift controller for distributed drive electric vehicle with input coupling and uncertain disturbance. *ISA Transactions* 120 (2022), 1–17. DOI: [10.1016/j.isatra.2021.03.009](https://doi.org/10.1016/j.isatra.2021.03.009).
- [37] H. Nakano et al. Control of an electric vehicle with a large sideslip angle using driving forces of four independently-driven wheels and steer angle of front wheels. *2014 IEEE/ASME International Conference on Advanced Intelligent Mechatronics*. 2014, 1073–1078. DOI: [10.1109/AIM.2014.6878223](https://doi.org/10.1109/AIM.2014.6878223).

- [38] S. Horiuchi, K. Okada and S. Nohtomi. Analysis of accelerating and braking stability using constrained bifurcation and continuation methods. *Vehicle System Dynamics* 46 (2008), 585–597. DOI: [10.1080/00423110802007779](https://doi.org/10.1080/00423110802007779).
- [39] M. Abe. A theoretical analysis on vehicle cornering behaviors in acceleration and in braking. *Vehicle System Dynamics* 15.sup1 (1986), 1–14. DOI: [10.1080/00423118608969122](https://doi.org/10.1080/00423118608969122).
- [40] A. Tremlett et al. Quasi-steady-state linearisation of the racing vehicle acceleration envelope: a limited slip differential example. *Vehicle System Dynamics* 52.11 (2014), 1416–1442. DOI: [10.1080/00423114.2014.943927](https://doi.org/10.1080/00423114.2014.943927).
- [41] De Novellis, Leonardo, Sorniotti, Aldo and Gruber, Patrick. Optimal Wheel Torque Distribution for a Four-Wheel-Drive Fully Electric Vehicle. *SAE International Journal of Passenger Cars - Mechanical Systems* 6.1 (2013), 128–136. DOI: <https://doi.org/10.4271/2013-01-0673>.
- [42] M. Klomp and R. Thomson. Influence of front/rear drive force distribution on the lateral grip and understeer of all-wheel drive vehicles. *International Journal of Vehicle Design* 56.1-4 (2011), 34–48. DOI: [10.1504/IJVD.2011.043272](https://doi.org/10.1504/IJVD.2011.043272).
- [43] F. Bucchi and F. Frendo. A new formulation of the understeer coefficient to relate yaw torque and vehicle handling. *Vehicle System Dynamics* 54.6 (2016), 831–847. DOI: [10.1080/00423114.2016.1167225](https://doi.org/10.1080/00423114.2016.1167225).
- [44] E. Ono et al. Bifurcation in vehicle dynamics and robust front wheel steering control. *IEEE Transactions on Control Systems Technology* 6.3 (1998), 412–420. DOI: [10.1109/87.668041](https://doi.org/10.1109/87.668041).
- [45] S. Shen et al. Nonlinear dynamics and stability analysis of vehicle plane motions. *Vehicle System Dynamics* 45.1 (2007), 15–35. DOI: [10.1080/00423110600828285](https://doi.org/10.1080/00423110600828285).
- [46] J. Pauwelussen. Axle characteristics and vehicle limit cycle behaviour. *Vehicle System Dynamics* 0.0 (2024), 1–19. DOI: [10.1080/00423114.2024.2322487](https://doi.org/10.1080/00423114.2024.2322487).
- [47] X. Wang et al. Research on the Vehicle Steering and Braking Stability Region. *Applied Sciences* 13.13 (2023). DOI: [10.3390/app13137806](https://doi.org/10.3390/app13137806).
- [48] L. Zhang et al. Cooperative chassis control system of electric vehicles for agility and stability improvements. *IET Intelligent Transport Systems* 13.1 (2019), 134–140. DOI: [10.1049/iet-its.2018.5079](https://doi.org/10.1049/iet-its.2018.5079).
- [49] Y. A. Kuznetsov. Elements of applied bifurcation theory. 2nd ed. New York: Springer, 1998.
- [50] R. Seydel. Practical bifurcation and stability analysis. 3rd ed. New York: Springer, 2010.
- [51] J. Guckenheimer and P. Holmes. Nonlinear oscillations, dynamical systems, and bifurcations of vector fields. 1st ed. New York: Springer, 1983.
- [52] H. Troger and A. Steindl. Nonlinear stability and bifurcation theory: an introduction for engineers and applied scientists. 1st ed. Vienna: Springer, 1991.

- [53] A. M. A. Hamdan and A. H. Nayfeh. Measures of modal controllability and observability for first- and second-order linear systems. *Journal of Guidance, Control, and Dynamics* 12.3 (1989), 421–428. DOI: [10.2514/3.20424](https://doi.org/10.2514/3.20424).
- [54] J. W. Choi et al. Design of an effective controller via disturbance accommodating left eigenstructure assignment. *Journal of Guidance, Control, and Dynamics* 18.2 (1995), 347–354. DOI: [10.2514/3.21390](https://doi.org/10.2514/3.21390).
- [55] W. F. Milliken and D. L. Milliken. Race car vehicle dynamics. Warrendale: SAE international, 1995.

## Paper A

*Insights into stability and control of the powerslide motion with variable drive torque distribution – applied to a driver assistance system*

TU Wien: Manuel Eberhart, Manfred Plöchl, Johannes Edelmann

CARIAD SE: Michael Unterreiner

*Vehicle System Dynamics*, January 2025

<https://doi.org/10.1080/00423114.2025.2457433>

**Keywords:** powerslide, drifting, nonlinear vehicle dynamics, all-wheel drive vehicle, controllability, driver model

**Abstract:** In this study, a theoretical investigation of the steady-state powerslide motion, or drift, is conducted to gain insight into the influence of the total drive torque and front/rear axle drive torque distribution on the powerslide dynamics of an all-wheel drive vehicle, including the case of a rear-wheel drive vehicle. The steady-state conditions and stability properties are derived, and different actuator inputs, i.e. steering angle, total drive torque and drive torque distribution, to stabilise the unstable powerslide motion are analysed and discussed with respect to different control strategies. The results indicate that the drive torque distribution is an effective control input for stabilisation and can be superior to the total drive torque input. The powerslide cannot be stabilised for particular conditions with the total drive torque input at fixed drive torque distribution. Based on these findings, a driver assistance system is presented that allows the human driver to track a desired circular path only by steering commands. The powerslide motion is stabilised automatically by a controller acting on the total drive torque and on the drive torque distribution if favourable. The characteristics, limitations in dynamics and reactions of a human driver are considered by introducing a virtual test driver model in a simulation environment. The successfully performed powerslide is shown in simulation with a basic vehicle model and in an experimental setup with a test vehicle.

## Insights into stability and control of the powerslide motion with variable drive torque distribution – applied to a driver assistance system

M. Eberhart<sup>a</sup>, M. Plöchl<sup>a</sup>, M. Unterreiner<sup>b</sup> and J. Edelmann<sup>a</sup>

<sup>a</sup>TU Wien, Institute of Mechanics and Mechatronics, Vienna, Austria; <sup>b</sup>CARIAD SE, Vehicle Motion & Energy, Wolfsburg, Germany

### ABSTRACT

In this study, a theoretical investigation of the steady-state powerslide motion, or drift, is conducted to gain insight into the influence of the total drive torque and front/rear axle drive torque distribution on the powerslide dynamics of an all-wheel drive vehicle, including the case of a rear-wheel drive vehicle. The steady-state conditions and stability properties are derived, and different actuator inputs, i.e. steering angle, total drive torque and drive torque distribution, to stabilise the unstable powerslide motion are analysed and discussed with respect to different control strategies. The results indicate that the drive torque distribution is an effective control input for stabilisation and can be superior to the total drive torque input. The powerslide cannot be stabilised for particular conditions with the total drive torque input at fixed drive torque distribution. Based on these findings, a driver assistance system is presented that allows the human driver to track a desired circular path only by steering commands. The powerslide motion is stabilised automatically by a controller acting on the total drive torque and on the drive torque distribution if favourable. The characteristics, limitations in dynamics and reactions of a human driver are considered by introducing a virtual test driver model in a simulation environment. The successfully performed powerslide is shown in simulation with a basic vehicle model and in an experimental setup with a test vehicle.

### ARTICLE HISTORY

Received 17 July 2024  
Revised 19 November 2024  
Accepted 16 January 2025

### KEYWORDS

Powerslide; drifting;  
nonlinear vehicle dynamics;  
all-wheel drive vehicle;  
controllability; driver model

## 1. Introduction

The powerslide is an unstable driving condition and is defined in [1] for rear-wheel drive (RWD) vehicles as a steady-state cornering motion with a large vehicle sideslip angle and large steering angle, where the front wheels point to the outside of the turn, combined with large traction forces at the rear axle. Due to the large sideslip angle of the vehicle and large longitudinal slips at the rear tyres, there is a strong coupling between the longitudinal and lateral tyre forces. Increasing the longitudinal tyre slip by increasing the drive torque

**CONTACT** Manuel Eberhart  [manuel.eberhart@tuwien.ac.at](mailto:manuel.eberhart@tuwien.ac.at)

© 2025 The Author(s). Published by Informa UK Limited, trading as Taylor & Francis Group.  
This is an Open Access article distributed under the terms of the Creative Commons Attribution-NonCommercial-NoDerivatives License (<http://creativecommons.org/licenses/by-nc-nd/4.0/>), which permits non-commercial re-use, distribution, and reproduction in any medium, provided the original work is properly cited, and is not altered, transformed, or built upon in any way. The terms on which this article has been published allow the posting of the Accepted Manuscript in a repository by the author(s) or with their consent.

reduces the lateral tyre forces. Human drivers of RWD vehicles are able to use this characteristic property of the tyre to stabilise the unstable powerslide motion with the drive torque input only [2].

Even though the powerslide is an unstable steady-state driving condition, it is frequently utilised by rally drivers, particularly on loose gravel surfaces. Techniques from rally drivers, i.e. the pendulum manoeuvre and trail braking, are analysed by Velenis et al. [3]. With optimisation methods, it is shown that high sideslip manoeuvres can be advantageous in particular cases. It is demonstrated in [4–7] that for specific road conditions, the minimum time manoeuvre for a hairpin curve is characterised by large sideslip angles of the vehicle and, dependent on the drivetrain architecture of the vehicle, even countersteering may be beneficial. In [8], Acosta et al. found that large vehicle sideslip angle manoeuvres can increase manoeuvrability, and in [9], it is shown that for off-road conditions, the maximum lateral acceleration at negotiating a curve with an overactuated vehicle is achieved with large vehicle sideslip angle.

The improvement in agility can help enhance vehicle safety and improve the capability of driver assistance systems or autonomous driving applications. Autonomous vehicles typically feature a conservative driving style, and stabilisation systems usually restrict the vehicle's operation to the linear handling regime. This is typically achieved by applying differential braking. The linear regime may be extended with enhanced drivetrain architectures, particularly with electric motors and independently driven wheels. Utilising the nonlinear handling regime, including large vehicle sideslip angles, may help gain more agility in specific scenarios, e.g. to avoid obstacles. Sorniotti et al. show that obstacles could be avoided more efficiently with a large sideslip manoeuvre than by regular driving applying a nonlinear MPC approach, [10]. Zhao et al. propose in [11] a controller to improve vehicle safety by allowing large vehicle sideslips in critical situations and show in [12] that corresponding manoeuvres may prevent collisions.

Several researchers investigated the powerslide condition and the stabilisation of this unstable vehicle state. Ono et al. [13] show for a basic two degrees of freedom vehicle model that vehicle loss of stability due to oversteering at high lateral acceleration is caused by a saddle-node bifurcation. A steering control strategy is proposed to stabilise the unstable motion of the vehicle. In [14], Della Rossa et al. published an extended analysis of possible equilibria for different vehicle handling and tyre characteristics and configurations with a similar two degrees of freedom vehicle model. In [14,15], it is noted that the powerslide is an unstable saddle node. Steindl et al. found in [16] periodic limit cycles after the non-oscillatory loss of stability of the powerslide, and Edelmann et al. reveal in [17] the influence of different constant inputs on these periodic motions and present respective vehicle measurements on packed snow.

A controllability analysis of the powerslide is carried out in [2]. The authors outline that the powerslide can either be stabilised with the drive torque, the steering angle, or with both inputs for a RWD vehicle. Velenis et al. propose a sliding-mode controller with only drive and braking inputs at the front and rear axle with fixed steering to stabilise the powerslide equilibrium, [18]. In [19], an LQR-controller for a FWD vehicle with handbrake actuation is suggested with steering and drive torque as input. Controllers for stabilisation of RWD vehicles with steering and drive torque input are proposed in [20–24]. Goh et al. simultaneously stabilise the powerslide and track a given path autonomously in [25], and

a model-inversion technique with wheel slip control is applied to improve the control performance in [26]. In [27], Goh et al. use a nonlinear model predictive control (NMPC) approach to perform dynamic, non-equilibrium drifting with a RWD vehicle while staying within the track limits. Front-wheel braking may be used to increase the set of possible vehicle trajectories, [28], and different controllers for overactuated vehicles with individual wheel drive are addressed in [9,29,30].

The main contribution of this paper is the analysis of the powerslide motion for an AWD vehicle with different drive torque distributions between the front and the rear axle, which has not been addressed in the literature before. An electric car with individual motors at the front and rear axle is considered, and various levels of friction potentials are included. Stability properties and possibilities to stabilise the powerslide motion are addressed by evaluating a controllability measure for different actuators which include steering angle, total drive torque and drive torque distribution. The need for a qualitative change of the control strategy for rear-wheel drive (RWD) and all-wheel drive (AWD) vehicles with fixed drive torque distribution to stabilise the powerslide is revealed and discussed. The stabilisation is shown both in simulation utilising a human driver model and in an experimental setup with the human driver in the loop. The driver's task is to track a circular trajectory with steering input only, while the powerslide motion is stabilised with a basic controller of the drive torque distribution, acting as a driver assistance system.

The remainder of this paper is organised as follows: Section 2 introduces the applied vehicle and tyre model. The system dynamics are studied in Section 3. The possible equilibria for the steady-state cornering condition are derived, and the stability and controllability properties of the powerslide conditions are discussed. Consequences on possible control strategies are addressed. Section 4 presents simulation and measurement results for a possible application in a driver assistance system. Finally, the essential outcome of the paper is briefly summarised, and conclusions are drawn.

## 2. Vehicle and tyre model

To investigate the impact of the drive torque distribution on the powerslide motion, in addition to the basic two-wheel vehicle model, Figure 1, the dynamics of the front and rear (substitutive) wheels are considered. Thus, the vehicle model has five degrees of freedom: vehicle velocity  $v$ , sideslip angle of the vehicle  $\beta$ , yaw rate  $\dot{\psi}$ , and angular velocities of the front and rear wheels  $\omega_F$  and  $\omega_R$ , respectively. The equations of motion of the basic two-wheel vehicle model read

$$m\dot{v} \cos \beta - m\dot{v}(\dot{\beta} + \dot{\psi}) \sin \beta = F_{xF} \cos \delta - F_{yF} \sin \delta + F_{xR} \quad (1)$$

$$m\dot{v} \sin \beta + m\dot{v}(\dot{\beta} + \dot{\psi}) \cos \beta = F_{xF} \sin \delta + F_{yF} \cos \delta + F_{yR} \quad (2)$$

$$\ddot{\psi} I_z = (F_{xF} \sin \delta + F_{yF} \cos \delta) l_F - F_{yR} l_R \quad (3)$$

with the vehicle mass  $m$ , the steering angle  $\delta$ , the distances  $l_F$  and  $l_R$  from the centre of gravity  $CG$  to the front and rear axle, the yaw moment of inertia of the vehicle  $I_z$ , the longitudinal axle/tyre forces  $F_{xF}$  and  $F_{xR}$ , and the lateral axle/tyre forces  $F_{yF}$  and  $F_{yR}$ . The axle/wheel dynamics at the front and rear axles are described by

$$I_F \dot{\omega}_F = T_F - r F_{xF} \quad \text{and} \quad I_R \dot{\omega}_R = T_R - r F_{xR} \quad (4)$$

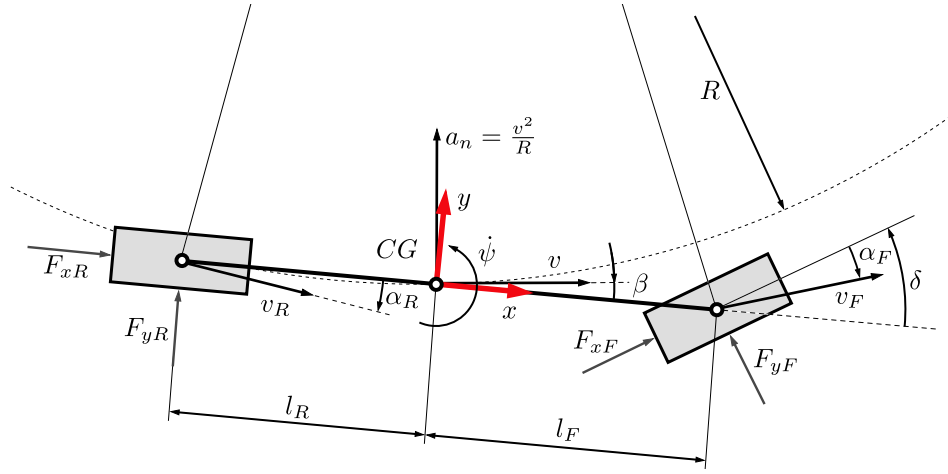


**Figure 1.** Two-wheel vehicle model at regular cornering.

with the angular velocities  $\omega_F$  and  $\omega_R$ , the effective moments of inertia  $I_F$  and  $I_R$ , the drive torques  $T_F$  and  $T_R$ , and the loaded radius  $r$ , which is considered constant and equal to the effective rolling radius.

To map the powerslide handling regime, not only the complete set of nonlinear system Equations (1)–(4) has to be considered, but also the mutual influence of longitudinal and lateral tyre forces. The *Magic Formula* tyre model [31] is applied here.

The respective sideslip angles  $\alpha_i$  and longitudinal slips  $s_{xi}$  of the tyres read

$$\alpha_F = \delta - \arctan\left(\frac{\dot{\psi}l_F}{v \cos \beta} + \tan \beta\right) \quad \text{and} \quad \alpha_R = -\arctan\left(-\frac{\dot{\psi}l_R}{v \cos \beta} + \tan \beta\right), \quad (5)$$

$$s_{xF} = -\frac{v_{wF} - \omega_F r}{v_{wF}} \quad \text{and} \quad s_{xR} = -\frac{v \cos \beta - \omega_R r}{v \cos \beta} \quad (6)$$

with the longitudinal velocity of the front tyre

$$v_{wF} = v \cos \beta \cos \delta + (v \sin \beta + \dot{\psi}l_F) \sin \delta. \quad (7)$$

As different front and rear tyres are considered, Figure 2 depicts the normalised combined longitudinal and lateral tyre forces for varied tyre sideslip angles  $\alpha_i$  for the front and rear tyres at the constant nominal tyre loads  $F_{zF} = 6000$  N and  $F_{zR} = 6250$  N. The tyre parameters are fitted to measurement data to achieve the desired handling characteristics of a reference vehicle, also taking the steering system compliance into account. Vehicle model parameters are listed in Table 1.

### 3. System dynamics analysis

To gain insight into the system dynamics of the powerslide, the steady-state solution branches of the system model are derived first. The influence of the tyre–road friction potential and the drive torque distribution on the steady-state solution branches are examined, and the corresponding stability properties and the effectiveness of different control inputs to stabilise the unstable powerslide solution branch are studied.

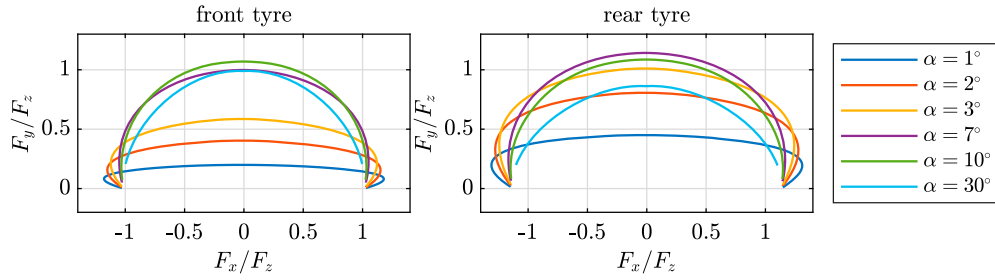


**Figure 2.** Combined tyre forces in the longitudinal and lateral direction for different sideslip angles  $\alpha$  and tyre-road friction potential  $\mu = 1$ .

**Table 1.** Parameters of the two-wheel vehicle model.

Parameter	Abbr.	Value	Unit
Vehicle mass	$m$	2500	kg
Yaw moment of inertia	$I_z$	3600	kgm <sup>2</sup>
Front axle inertia	$I_F$	6.5	kgm <sup>2</sup>
Rear axle inertia	$I_R$	40	kgm <sup>2</sup>
Front axle distance $\overline{CGF}$	$l_F$	1.48	m
Rear axle distance $\overline{CGR}$	$l_R$	1.42	m
Eff. rolling/loading radius	$r$	0.36	m

### 3.1. Steady-state solution branches

The nonlinear equations of motion in (1)–(4) are written in state-space notation

$$\dot{\mathbf{x}} = \mathbf{f}(\mathbf{x}, \mathbf{u}) \quad (8)$$

with the state vector  $\mathbf{x} = [\beta, \dot{\psi}, v, \omega_F, \omega_R]^T$  and input vector  $\mathbf{u} = [\delta, T_{\text{tot}}, \gamma]^T$  with total drive torque  $T_{\text{tot}} = T_F + T_R$  and drive torque distribution  $\gamma = T_R/T_{\text{tot}}$ , defined as the portion of the total drive torque at the rear axle. The steady-state solution branches of the system (8) are numerically calculated by setting  $\dot{\mathbf{x}} = \mathbf{0}$  and  $\dot{\psi} = v/R$  with constant radius of curvature  $R$ .

For the handling diagram in Figure 3, the vehicle sideslip angle  $\beta$ , the steering angle  $\delta$  and the total drive torque  $T_{\text{tot}}$  are plotted over the normal acceleration  $a_n = v^2/R$ . Therefore, a radius of curvature with  $R = 60$  m, a tyre-road friction potential with  $\mu = 1$ , and a drive torque distribution with  $\gamma = 0.8$  have been assumed. Similar to [1], up to four different steady-state solutions are found for a particular vehicle velocity  $v$  and radius of curvature  $R$ .

Besides regular cornering ①, with small positive steering angle  $\delta$ , small vehicle sideslip angle  $\beta$ , and small total drive torque  $T_{\text{tot}}$ , there are two additional branches, ② and ④, denoted overdraw steering, with larger positive steering angle  $\delta$  and therefore larger sideslip angle  $\alpha_F$  at the front axle w.r.t. regular cornering.

The first overdraw steering branch ② appears when, due to the friction limit of the front tyre, the maximum lateral acceleration  $a_n$  is reached, and the steering angle is further increased. The sideslip angle  $\alpha_F$  at the front axle increases while the vehicle sideslip angle  $\beta$  remains almost the same w.r.t. regular cornering.

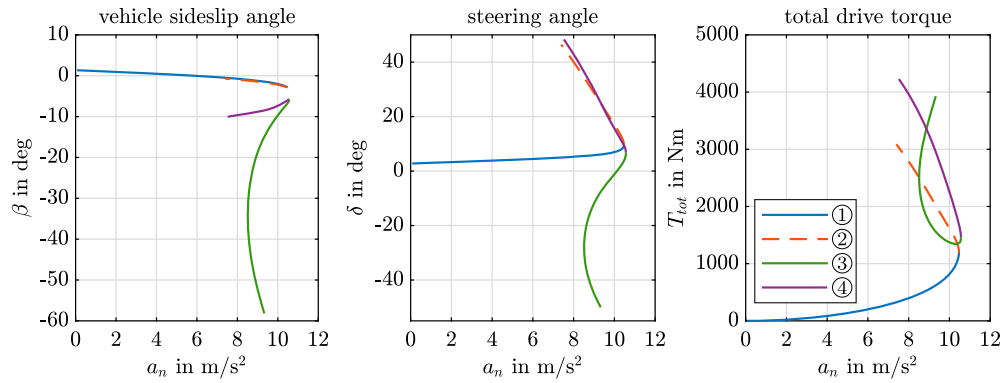


**Figure 3.** Steady-state solutions of the two-wheel vehicle model (①: regular cornering, ②: overdraw steering 1, ③: powerslide, ④: overdraw steering 2) for radius  $R = 60$  m, tyre–road friction potential  $\mu = 1$ , and drive torque distribution  $\gamma = 0.8$ .

For the second overdraw steering branch ④, the vehicle sideslip angle  $\beta$  shows a decreased but rather constant negative value of about  $\beta \approx -8^\circ$ , while the sideslip angle of the front axle  $\alpha_F$  increases with decreasing normal acceleration. The required total drive torque for both overdraw steering solutions increases with the steering angle  $\delta$  due to the higher cornering resistance.

The powerslide branch ③ shows large negative vehicle sideslip angles  $\beta$ , large negative steering angles  $\delta$ , and large total drive torques  $T_{\text{tot}}$ . It becomes evident from Figure 3 that the powerslide branch joins the second overdraw steering branch ④. In contrast to ④, the lateral tyre forces of the front axle are not saturated. Since Figure 3 corresponds to a left turn with a positive yaw rate  $\dot{\psi}$  according to Figure 1, the negative steering angle  $\delta$  indicates that the front wheels point to the outside of the curve, called countersteering.

Due to large sideslip angles  $\alpha_R$  and large longitudinal forces  $F_{xR}$  at the rear axle, the corresponding tyre forces are saturated at the powerslide branch ③. As a result of the mutual influence of longitudinal and lateral tyre forces, a strong coupling between the longitudinal and lateral dynamics of the vehicle can be expected, see subsequent Section 3.3. Moreover, this mutual influence may be helpful in the control and stabilisation task of the powerslide motion, see Sections 3.4 and 3.5.

### 3.2. Variation of friction potential and drive torque distribution

For a decreasing friction potential  $\mu$  of the tyre–road contact, the steady-state powerslide branch is shifted to lower normal accelerations  $a_n$ , as depicted in Figure 4(a), while its general shape remains similar.

By examining the required total drive torque  $T_{\text{tot}}$  for a steady-state powerslide at different vehicle sideslip angles  $\beta$  and tyre–road friction potentials  $\mu$ , an almost linear relationship between the resulting normal acceleration  $a_n = a_n(\beta, \mu)$  and the total drive torque  $T_{\text{tot}}$  appears, just as between the vehicle sideslip angle  $\beta$  and the total drive torque  $T_{\text{tot}}$ , Figure 4(b).

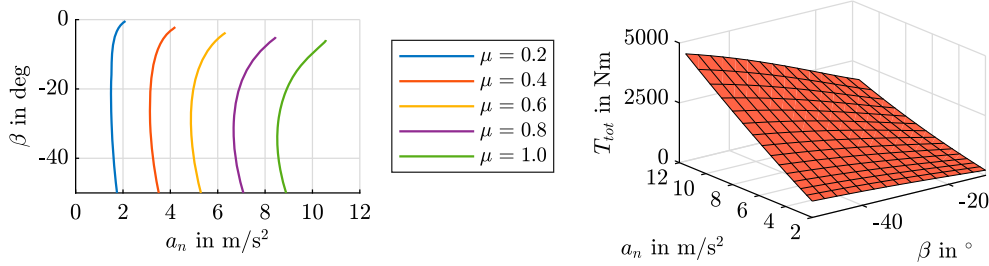


**Figure 4.** Steady-state solutions of the powerslide branch for different tyre–road friction potentials and required total drive torque ( $R = 60 \text{ m}$ ,  $\gamma = 0.8$ ). (a) Powerslide branches for different tyre–road friction potentials  $\mu$  and (b) Total drive torque  $T_{\text{tot}}$  depending on normal acceleration  $a_n$  and vehicle sideslip angle  $\beta$ .

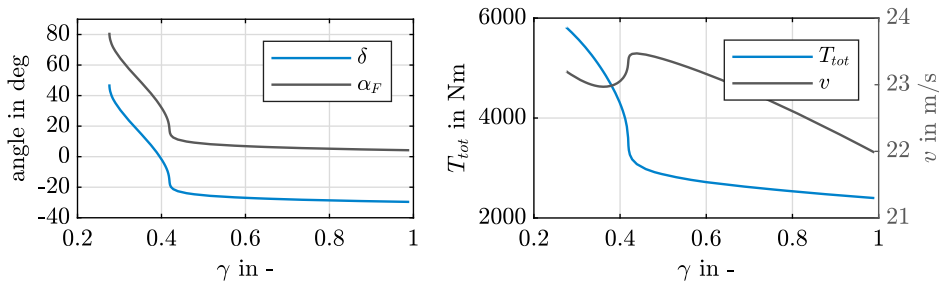


**Figure 5.** Steady-state solutions of the powerslide branch for different drive torque distributions  $\gamma$  at the constant vehicle sideslip angle  $\beta = -35^\circ$ . (a) Steering angle  $\delta$  and sideslip angle at the front axle  $\alpha_F$  and (b) Total drive torque  $T_{\text{tot}}$  and velocity  $v$ .

To learn about the existence and characteristic properties of the powerslide for different drive torque distributions  $\gamma$ , all steady-state solutions for constant vehicle sideslip angles  $\beta$  are calculated for  $\gamma$  reduced from  $\gamma = 1$  towards 0 until no powerslide solution exists.

For the chosen constant vehicle sideslip angle  $\beta = -35^\circ$ , steady-state solutions for the considered vehicle parameters are found in the range from  $\gamma = 1$  (rear-wheel drive) to the most ‘front-oriented’ drive torque distribution of  $\gamma \approx 0.27$ , see Figure 5. From  $\gamma = 1$  until  $\gamma \approx 0.43$  slightly increasing, large negative steering angles  $\delta$  result, typical for the powerslide motion with a rear-wheel drive vehicle, [1]. Also, the sideslip angle of the front axle  $\alpha_F$ , the total drive torque  $T_{\text{tot}}$ , and the vehicle velocity  $v$  slightly increase in this range until the maximum velocity is reached at  $\gamma \approx 0.43$ . In contrast, at drive torque distributions  $\gamma < 0.43$ , considerably less countersteering is required until regular steering (positive steering angle) is necessary for  $\gamma < 0.39$ . The need for considerably smaller negative or even positive steering angles  $\delta$  when drifting all-wheel drive vehicles compared with rear-wheel drive vehicles is well known from anecdotal evidence and observations. Moreover, a strong increase of the total drive torque  $T_{\text{tot}}$  is observed for  $\gamma < 0.43$ . This increase may be attributed to the degraded lateral tyre force potential at the front axle from the mutual influence of lateral and longitudinal tyre forces, resulting in very large sideslip angles  $\alpha_F$  and increased steering angles  $\delta$ , and corresponding energy dissipation.

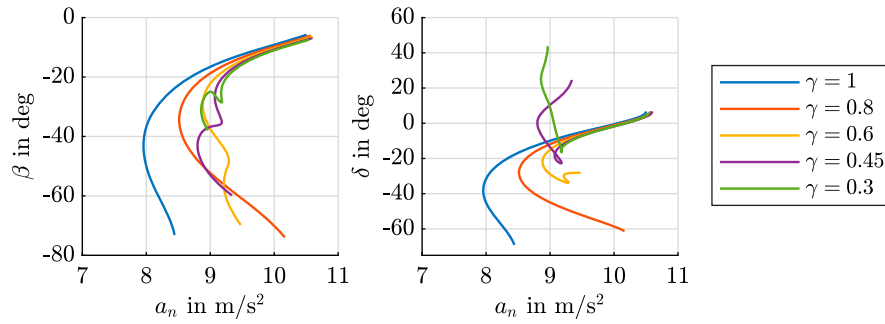


**Figure 6.** Vehicle sideslip angle  $\beta$  and steering angle  $\delta$  of the powerslide branch for different drive torque distributions  $\gamma$  ( $R = 60$  m,  $\mu = 1$ ).

The handling diagrams for different constant drive torque distributions  $\gamma$  are shown in Figure 6. For larger values of  $\gamma$ , the characteristics of the powerslide branches for vehicle sideslip angle and steering angle are similar as for rear-wheel drive vehicles. Decreasing values of  $\gamma$  further, results in a change of the characteristics, as front tyre forces become saturated as well. For certain vehicle velocities  $v$  and drive torque distributions  $\gamma$ , up to four powerslide equilibria can be identified for a given radius of curvature  $\rho$  and normal acceleration  $a_n$ , see, for example,  $\gamma = 0.6$  in Figure 6(right). Moreover, at more front-orientated drive torque distributions, e.g.  $\gamma = 0.45$ , where vehicle sideslip angles  $\beta$  are still large and negative, steering angles  $\delta$  may be positive, indicating regular steering, similar to Figure 5(a). Consequently, in contrast to RWD vehicles, counter-steering may not be required to maintain a steady-state powerslide for AWD vehicles, depending on the drive torque distribution  $\gamma$ . Considering a given vehicle sideslip angle  $\beta$ , up to three powerslide equilibria can be identified for a constant drive torque distribution  $\gamma$ , each associated with a different normal acceleration  $a_n$  and steering angle  $\delta$ , see e.g.  $\gamma = 0.3$  in Figure 6(left). Obviously, smaller values of  $\gamma$  result in higher normal accelerations  $a_n$ .

### 3.3. Stability of first order and modal analysis

Linearisation of the nonlinear system equations at the steady-state solution branches results in  $\Delta \dot{\mathbf{x}} = \mathbf{A} \Delta \mathbf{x} + \mathbf{B} \Delta \mathbf{u}$  with system matrix  $\mathbf{A}$  and input matrix  $\mathbf{B}$ .  $\Delta \mathbf{x} = \mathbf{x} - \mathbf{x}_0$  is the deviation of the state vector and  $\Delta \mathbf{u} = \mathbf{u} - \mathbf{u}_0$  the deviation of the input vector from the steady-state solution, indicated by index 0. For the sake of simplicity,  $\Delta$ -symbols and 0-indices have been omitted below. By solving the eigenvalue problem  $(\mathbf{A} - \mathbf{I}\lambda_i)\mathbf{p}_i = \mathbf{0}$  for eigenvalues  $\lambda_i$  and right eigenvectors  $\mathbf{p}_i$  corresponding to mode  $i$  ( $i = 1-5$ ), the local dynamic behaviour and stability of the steady-state solutions can be analysed.

The vehicle shows understeering characteristics at the regular cornering branch ① in Figure 3, the eigenvalues are all negative, and steady-state solutions are stable. The eigenvalues of the connecting first overdraw steering branch ② have only negative real parts as well, and also these steady-state solutions are stable. For the regular cornering branch, the largest eigenvalue always remains real but still negative and very close to zero; see also [1]. The main entries in the corresponding right eigenvector are related to velocity  $v$  and angular velocities of the front and rear wheels,  $\omega_F$  and  $\omega_R$ , and therefore can be associated with a ‘velocity mode’. The next two eigenvalues change from real to a conjugate-complex pair

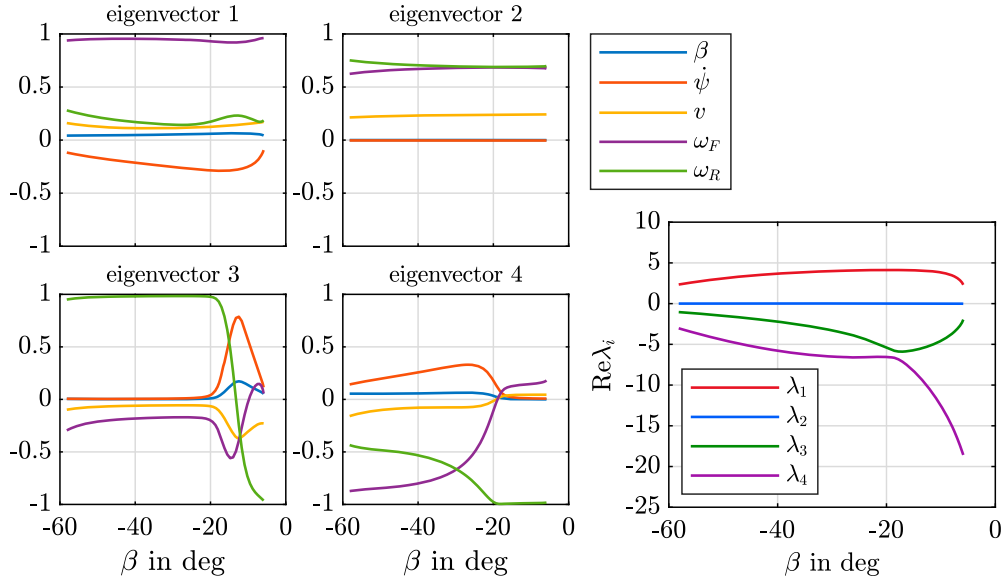


**Figure 7.** Dominant eigenvectors and eigenvalues corresponding to the powerslide branch ③ in Figure 3.

of eigenvalues with increasing velocity  $v$ . The oscillation mode remains for the first overdraw steering branch ②, with main contributions to yaw rate  $\dot{\psi}$  and vehicle sideslip angle  $\beta$ , affecting the lateral motion of the vehicle. The two remaining eigenvalues are largely negative, and the largest entries of the corresponding eigenvectors are mainly related to the angular velocities of the front and rear wheels,  $\omega_F$  and  $\omega_R$ .

For the powerslide branch ③ in Figure 3, the eigenvalues  $\lambda_i$  ( $i = 1-4$ ) and the entries in the corresponding (normalised) eigenvectors  $\mathbf{p}_i$  are plotted over the vehicle sideslip angle  $\beta$  in Figure 7. Index 1 refers to the largest and positive eigenvalue, index 4 to the smallest, negative eigenvalue. Less interesting  $\lambda_5$  and  $\mathbf{p}_5$  are not shown, the eigenvalue is largely negative, and its eigenvector has a main component in the angular velocity of the front wheel  $\omega_F$ .

In contrast to regular cornering, the eigenvalues of powerslide branch are always real. The real eigenvalues  $\lambda_1$  and  $\lambda_2$  are positive over the full range of vehicle sideslip angles  $\beta$ . Hence, the corresponding steady-state solutions are unstable, and the loss of stability is monotonic and governed by mode 1, see also [1], since  $\lambda_2$  is very close to zero, quite similar to the ‘velocity mode’ at the regular cornering branch. The entries in the eigenvectors corresponding to  $\lambda_1$  remain almost constant over the full range of vehicle sideslip angles  $\beta$  and affect all states, see Figure 7 on the left, with the largest contributions to the angular velocity of the front wheel  $\omega_F$  and the yaw rate  $\dot{\psi}$ .

The non-oscillatory and similar behaviour over the full vehicle sideslip range could be beneficial for the control and stabilisation task of the driver, considering the limitations of a human driver [32]. Since the contribution to the yaw rate  $\dot{\psi}$  remains quite large compared to the other ‘modes’, this unstable mode may be denoted ‘yaw mode’.

A qualitative change in the course of entries in the eigenvectors of mode 3 and 4 can be observed at  $\beta \approx -20^\circ$ , Figure 7, where the magnitudes of the real eigenvalues  $\lambda_3$  and

$\lambda_4$  come quite close. For vehicle sideslip angles  $\beta < -20^\circ$ , the angular velocity of the rear wheel  $\omega_R$  is dominant in the eigenvector of mode 3, and for  $\beta > -20^\circ$  in the eigenvector of mode 4. The eigenvalue  $\lambda_4$  for  $\beta > -20^\circ$  and  $\lambda_3$  for  $\beta < -20^\circ$  (in the areas where the angular velocity of the rear wheel  $\omega_R$  is dominant) strongly depends on the rear axle inertia  $I_R$ . A lower rear axle inertia would shift these eigenvalues to lower values and therefore the location of the qualitative change of the mode shapes to lower vehicle sideslip angles. A large decrease in the rear axle inertia  $I_R$  would even prevent the change of mode shape.

Following the powerslide branch, the second overdraw steering branch ④ in Figure 3 appears with increasing steering angles  $\delta$  after passing the maximum normal acceleration  $a_n$ . The second overdraw steering branch also corresponds to unstable steady-state solutions. The modes are qualitatively similar to the powerslide modes for small vehicle sideslip angles  $\beta$ , where again the real eigenvalue  $\lambda_1$  related to the ‘yaw mode’ is positive and the real eigenvalue  $\lambda_2$  related to the ‘velocity mode’ is negative. In contrast to the powerslide solutions, the lateral tyre force at the front axle is saturated.

Variation of the tyre–road friction potential in the range  $\mu = 0.2 - 1$  reveals for the powerslide branch that the friction potential has no qualitative impact on the dynamic behaviour. The eigenvalue of the unstable mode 1 decreases slightly with reduced friction potential. A similar result is found by varying the drive torque distribution between  $\gamma = 0.6 - 1$ . The largest (positive) eigenvalue decreases slightly with decreasing  $\gamma$ .

### 3.4. Controllability analysis of the powerslide motion

As shown in [2], the powerslide of a RWD vehicle can either be stabilised with the drive torque at the rear axle, with the steering angle, or with a combination of both commands. The effectiveness of the different inputs to control the steady-state regular cornering and powerslide motion with respect to sensed vehicle states has been evaluated by a gross measure of joint modal controllability and observability. It provides an idea of how a mode is affected by a specific input and how visible it is from a specific output of the locally linearised system model. The measure was introduced by Hamdan et al. [33]. Choi et al. applied a modified version in [34] by taking the length of the input vector  $|\mathbf{b}_j|$  of input  $j$  from input matrix  $\mathbf{B}$  into account. In this work, the measure is further extended by considering the range of operation of each actuator by scaling the modal controllability measure with the maximum input of the actuator.

The subsequent measure of modal controllability of mode  $i$  with input  $j$  is the cosine of the angle between the left eigenvector  $\mathbf{q}_i$  (from  $\mathbf{A}^T \mathbf{q}_i = \lambda_i \mathbf{q}_i$ ) and input vector  $\mathbf{b}_j$  scaled with the norm of the input vector  $|\mathbf{b}_j|$  and the maximum input  $u_{j,\max}$  of actuator  $j$ . This measure can be interpreted as the projection of the input vector  $\mathbf{b}_j$  on the left eigenvector  $\mathbf{q}_i$  normalised to length 1, scaled with  $u_{j,\max}$  and yields

$$M_{c,ij} = \cos \theta_{ij} |\mathbf{b}_j| u_{j,\max} \quad \text{with} \quad \cos \theta_{ij} = \frac{\mathbf{q}_i^T \mathbf{b}_j}{|\mathbf{q}_i| |\mathbf{b}_j|}. \quad (9)$$

Here, the maximum input  $u_{j,\max}$  is set to  $u_{\delta,\max} = \pi/4$  for the steering angle  $\delta$ ,  $u_{T_{\text{tot}},\max} = 5000$  for the total drive torque  $T_{\text{tot}}$ , and  $u_{\gamma,\max} = 1$  for the drive torque distribution  $\gamma$ . As a measure for the modal observability of mode  $i$  from output  $k$ , the projection of the right

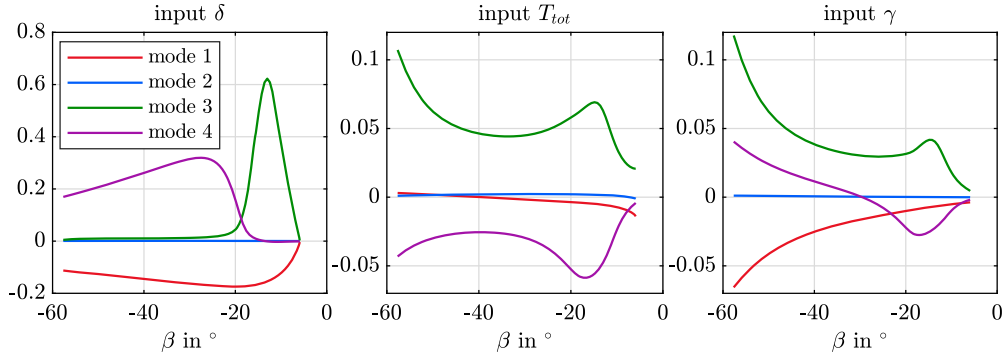


**Figure 8.** Joint modal controllability and observability measure  $M_{co,j\beta}$  for inputs  $j = \{\delta, T_{tot}, \gamma\}$  and observed vehicle sideslip angle  $\beta$  for the powerslide branch ③ in Figure 3.

eigenvector  $\mathbf{p}_i$  on the output vector  $\mathbf{c}_k$  from output matrix  $\mathbf{C}$  is applied,

$$M_{o,ki} = \cos \theta_{ki} |\mathbf{c}_k| \quad \text{with} \quad \cos \theta_{ki} = \frac{\mathbf{c}_k \mathbf{p}_i}{|\mathbf{p}_i| |\mathbf{c}_k|}. \quad (10)$$

The product of these two measures

$$M_{co,jk} = M_{o,ki} M_{c,ij} \quad (11)$$

provides insight into the effectiveness of specific actuator input–measured output combinations to control a specific mode and thus stabilise the unstable powerslide equilibrium.

The measure in (11) is now evaluated for the steady-state powerslide branch ③ in Figure 3 ( $R = 60$  m,  $\mu = 1$ , and  $\gamma = 0.8$ ) for the inputs  $\delta$ ,  $T_{tot}$  and  $\gamma$ , and output  $\beta$ . Figure 8 shows the measure  $M_{co,j\beta}$  for the first four modes, plotted over the steady-state vehicle sideslip angle  $\beta$  (actually  $\beta_0$  for clearness). Since the linear analysis is only valid in the vicinity of the steady-state solutions of the nonlinear powerslide branch, the results have to be interpreted with care.

The left plot of Figure 8 shows that the unstable mode 1 can be controlled very effectively with the steering angle  $\delta$  for the full range of considered vehicle sideslip angles  $\beta$ . In the range of vehicle sideslip angles where  $\omega_R$  is the dominant entry in the eigenvector of modes 3 and 4, see Figure 7, the possibility to influence these modes with the steering angle  $\delta$  almost vanishes, whereas controllability is given in the range of vehicle sideslip angles  $\beta$  where the yaw rate  $\dot{\psi}$  is the dominant entry. Mode 2, which represents the ‘velocity mode’, can hardly be controlled by the steering angle.

For the total drive torque input  $T_{tot}$  an interesting observation can be made, middle plot of Figure 8. The joint modal measure for the unstable mode 1 is about zero for vehicle sideslip angles  $\beta \approx -40^\circ$  and also changes its sign for further decreasing  $\beta$ . Thus, in this specific condition, the unstable mode cannot be controlled. This observation and the consequences of the change of the sign of the measure will be discussed in more detail below. Modes 3 and 4 that are basically dominated by the yaw and rear axle motion,  $\dot{\psi}$  and  $\omega_R$ , respectively, can be influenced well with input  $T_{tot}$ , whereas the measure remains again small for the ‘velocity mode’ 2 for the full range of vehicle sideslip angles  $\beta$ .

In the right plot of Figure 8, the modal measure is presented for the drive torque distribution  $\gamma$ . The possibility to influence the unstable mode 1 rises with decreasing vehicle

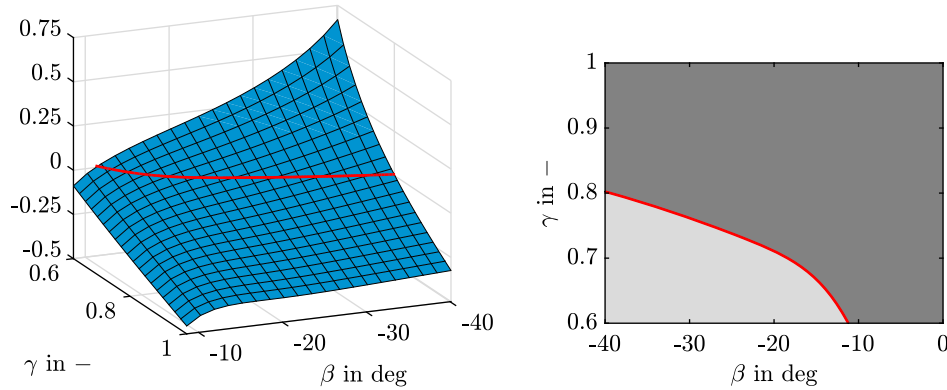


**Figure 9.** Modal controllability measure  $M_{c,1T_{tot}}$  for input  $T_{tot}$  and mode 1 ( $\mu = 1$ ). (a)  $M_{c,1T_{tot}}$  for different vehicle sideslip angles  $\beta$  and drive torque distributions  $\gamma$  and (b) Projection to the  $\beta$ - $\gamma$  plane: qualitative change of the control strategy at  $M_{c,1T_{tot}} = 0$  (red line).

sideslip angles  $\beta$ . The influence of  $\gamma$  on mode 3 is high and almost zero on the ‘velocity mode’, similar to the influence of the steering input  $\delta$ . For mode 4, the measure also exhibits zero-crossing. However, this is not relevant since the real eigenvalue related to mode 4 is negative.

Similar results as shown in Figure 8 are found for different tyre–road friction potentials  $\mu$ .

To gain more insight into the change of the sign of the joint modal controllability and observability measure  $M_{co,T_{tot}\beta}$  for the input total drive torque  $T_{tot}$  of the unstable mode 1, Figure 8, the associated modal controllability measure  $M_{c,1T_{tot}}$  in (9), is shown for different vehicles sideslip angles  $\beta$  and drive torque distributions  $\gamma$  in Figure 9(a).

It can be noticed that there are combinations of drive torque distributions  $\gamma$  and vehicle sideslip angles  $\beta$  where  $M_{c,1T_{tot}}$  crosses zero and changes its sign. The term  $\cos \theta_{1T_{tot}}$  in (9) becomes zero, when the angle between the input vector  $\mathbf{b}_{T_{tot}}$  and the left eigenvector  $\mathbf{q}_1$  related to mode 1 are orthogonal to each other. After transition through  $M_{c,1T_{tot}} = 0$  for e.g. varied  $\beta$  and fixed  $\gamma$ , the control command (w.r.t. the steady-state input) changes sign for a similar yaw response considering the unstable, dominant ‘yaw mode’ of the powerslide equilibrium, which is associated with a change of control strategy. Therefore, the required (strategy for the) control of the total drive torque  $T_{tot}$  to stabilise the powerslide mode at large negative vehicle sideslip angles  $\beta$ , will strongly depend on the drive torque distribution  $\gamma$ , see Figure 9(b).

Consequently, the control strategies may be distinguished by the drive train configuration between ‘RWD-strategy’ and ‘AWD-strategy’. The assumed distinction coincides with anecdotal knowledge from expert drivers, who report that a RWD vehicle can be controlled easily by drive torque commands (corresponding to  $T_{tot}$ ), since increased drive torque results in increased longitudinal slip  $s_{xR}$  and reduced lateral tyre forces  $F_{yR}$  at the rear axle, and therefore increased yaw rate  $\dot{\psi}$ , and vice versa. In contrast, at AWD vehicles, the increased drive torque  $T_{tot}$  results also in additional longitudinal tyre forces  $F_{xF}$  at the front axle that overcompensate the effects from the reduced lateral tyre forces  $F_{yR}$  at the rear axle, hence the yaw rate  $\dot{\psi}$  decreases. The areas of different control strategies in the

$\gamma - \beta$  plane are illustrated in Figure 9(b) in dark grey colour for ‘RWD-strategy’ and light grey colour for ‘AWD-strategy’.

### 3.5. Control strategy

The loss of controllability with the total drive torque  $T_{\text{tot}}$  in particular situations in contrast to the drive torque distribution  $\gamma$  suggests that  $\gamma$  or individual axle torques are proper inputs to stabilise the powerslide, or might even be superior to the total drive torque  $T_{\text{tot}}$  with fixed torque distribution  $\gamma$ . Therefore, a control strategy that stabilises the powerslide motion just with the drive train, in particular of an AWD vehicle, is addressed in this section. The steering angle shall be left for the control of the circular path.

The analysis with the joint modal controllability and observability measure, Figure 8, has revealed that the vehicle sideslip angle  $\beta$  and the yaw rate  $\dot{\psi}$  are proper measurement variables for a controller, with the last being even more effective for influencing the unstable powerslide or ‘yaw mode’. However, as there is only a marginal effect on the unstable ‘velocity mode’, further measurement variables related to the longitudinal motion are required, such as velocities  $v$ ,  $\omega_F$ ,  $\omega_R$ , which show a strong effect on the ‘velocity mode’. In agreement with the evaluation of the controllability criteria from Kalman and Hautus [35], the unstable eigenvalues can be stabilised, and the dynamics chosen favourably by placing the eigenvalues of the closed-loop, respectively, using the full state vector as a measurement vector.

However, to mimic a human driver, only the observed vehicle sideslip angle and yaw rate will now be considered as measurement variables. The idea is motivated by Goh et al. [26], who state that the vehicle velocity  $v$  does not need to be explicitly regulated even though the variable  $\dot{v}$  is uncontrolled as the coupling between the lateral and the longitudinal dynamics that occurs at high sideslip stabilises the velocity when operating under their imposed control law. It is interesting to note that these findings hold for their vehicle with RWD, but not necessarily for an AWD vehicle.

For illustration, the system model is linearised w.r.t.  $\beta = -35^\circ$  and a constant output feedback controller is considered to stabilise the steady-state powerslide equilibrium with input  $T_{\text{tot}}$  and outputs  $\dot{\psi}$  and  $\beta$ . The controller gains are denoted  $K_{\dot{\psi}}$  and  $K_\beta$ , respectively. The real parts of the largest eigenvalue of the controlled system are calculated for a wide range of control gains  $K_\beta$  and  $K_{\dot{\psi}}$  and plotted for configurations  $\gamma = 1$  (RWD) and  $\gamma = 0.6$  (AWD) in Figure 10.

For  $\gamma = 1$  (RWD) the largest eigenvalue can be moved into the negative half-plane for specific control gains. In contrast, for  $\gamma = 0.6$  (AWD), the largest eigenvalue remains positive and the equilibrium unstable for all combinations of gains  $K_{\dot{\psi}}$  and  $K_\beta$ . Both systems are controllable, except for drive torque distributions  $\gamma$  on the red line in Figure 9(b). However, the limited number of two controller design parameters only does not allow the five poles to be placed freely. Nevertheless, the RWD vehicle can still be stabilised, but not the AWD vehicle at  $\gamma = 0.6$ . For small enough  $\gamma$ , close to the limit of existing powerslide motions, stabilisation with this reduced control design space will be possible again.

When aiming to reduce the real part of the largest eigenvalue by a proper choice of  $K_\beta$ , signs of  $K_\beta$  are opposite for the two drive train configurations, Figure 10, confirming the above-mentioned different control strategies to stabilise the powerslide motion at RWD or

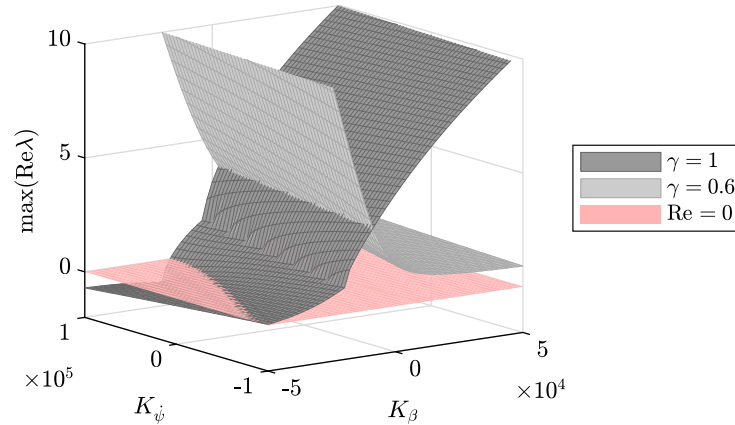


**Figure 10.** Maximum real part of the largest eigenvalue of the controlled system with gains  $K_{\psi}$  and  $K_{\beta}$ .

AWD vehicles. For RWD vehicles, the total drive torque  $T_{\text{tot}}$  needs to be reduced to diminish the vehicle sideslip angle  $\beta$ , and also the vehicle velocity  $v$  will be reduced accordingly (*RWD-strategy*). For  $\gamma$  in the light grey area of Figure 9(b), the total drive torque  $T_{\text{tot}}$  needs to be increased to diminish the vehicle sideslip angle  $\beta$ , and therefore the vehicle velocity  $v$  will also increase (*AWD-strategy*).

In conclusion, for AWD vehicles with specific constant drive torque distributions  $\gamma$ , the unstable eigenvalue related to the ‘yaw mode’ can be stabilised with the above controller. Still, one eigenvalue related to the ‘velocity mode’ remains unstable. Although the ‘velocity mode’ is also (slightly) unstable at RWD vehicles, the vehicle velocity converges to its equilibrium state when the vehicle sideslip angle is stabilised by the total drive torque due to the velocity zero-dynamics, [26]. But for AWD vehicles, the total drive torque to stabilise the unstable ‘yaw mode’ and thus the vehicle sideslip angle does not automatically stabilise the unstable ‘velocity mode’, indicating possibly unstable zero-dynamics. This result coincides with findings from [36], based on a phase-plane analysis of the powerslide motion.

As a consequence, it is assumed, when utilising a constant output controller with the vehicle sideslip angle as a measurement variable, having the right graph of Figure 8 in mind, that the powerslide motion could be stabilised for AWD vehicles with a variable drive torque distribution. In this way, with large  $\gamma$ , the benefit from a stable ‘velocity mode’ and with small  $\gamma$ , the benefit from a direct yaw moment due to the longitudinal tyre forces at the front axle can be combined. The feasibility of this approach is now tested in a particular application case.

#### 4. Application: driver assistance system

Based on the above analysis of the powerslide branch ③ in Figure 3 and the effectiveness of the investigated control inputs, a basic driver assistance system to perform a steady-state powerslide is proposed in this section. The task of this driver assistance system is to stabilise the powerslide motion by shifting the total drive torque between the front and rear axle, where the human driver has to track the circular path only by utilising steering commands.

In contrast to previous work, e.g. [9,24,26], which focuses on autonomous drifting, the human driver is included in the control loop.

Considering the conclusions from Sections 3.4 and 3.5, a variable drive torque distribution  $\gamma$  is used to stabilise the steady-state powerslide motion. The nominal drive torque distribution  $\gamma_0$  is selected in the range  $\gamma_0 = 0.5 - 0.9$  for powerslide steering behaviour with a negative steering angle and small sideslip angle at the front axle  $\alpha_F$  according to Figure 5. The total drive torque  $T_{\text{tot},0}(\beta_{\text{des}}, \mu, \gamma_0)$  is pre-selected to adjust to a desired vehicle sideslip angle  $\beta_{\text{des}}$  for a given tyre-road friction potential  $\mu$  and nominal drive torque distribution  $\gamma_0$ , see Figures 4(b) and 5 in Section 3.2.

A simple PD-controller is chosen to move the eigenvalue of the unstable mode 1, Figure 7 in Section 3.3, to the negative half-plane by controlling the drive torque of the front and rear axle,  $T_F$  and  $T_R$ ,

$$T_F = T_{\text{tot},0}(1 - \gamma_0) + a_1 e_\beta + a_2 \dot{e}_\beta \quad (12a)$$

$$T_R = T_{\text{tot},0}\gamma_0 - a_1 e_\beta - a_2 \dot{e}_\beta \quad (12b)$$

with the vehicle sideslip angle error  $e_\beta = \beta - \beta_{\text{des}}$  and its derivative  $\dot{e}_\beta$ , and the control gains  $a_1$  and  $a_2$ . Since (regenerative) braking is not considered, the lower boundary for the axle drive torques is zero. If this boundary is reached, the total drive torque  $T_{\text{tot}}$  can be increased by the driver assistance system (limited by the maximum motor torque) for better tracking performance of the controller at large disturbances. The availability of regenerative braking would be favourable in this respect.

#### 4.1. Human driver model – virtual test driver

To investigate the driver assistance system in the simulation environment, first, its interaction with a human driver is considered by adapting the virtual two-layer test driver model described in [37]. The steering angle  $\delta = \delta_{ff} + \delta_c + \delta_{cs}$  is composed of the steering angle  $\delta_{ff}$  from anticipation, the steering angle  $\delta_c$  from disturbance compensation, and the steering angle  $\delta_{cs}$  from countersteering. Since the anticipated curvature  $\kappa$  of the track remains constant for the circular path, the *anticipatory feed-forward layer* results in the constant steering angle  $\delta_{ff} = \delta_{ff,0}$  corresponding to the regular cornering manoeuvre before the powerslide is initiated.

The predictive *compensatory closed-loop layer*  $G_c(s)$  compensates the predicted (with preview time  $T_p$ ) path deviation  $\Delta y$  with the steering input  $\delta_c$ ,

$$G_c(s) = \frac{\delta_c(s)}{\Delta y(s)} = K_c \frac{1 + T_v s}{1 + T_n s} e^{-s\tau}, \quad (13)$$

with driver gain  $K_c$  and time constants  $T_v$  and  $T_n$ . The human reaction time is chosen constant  $\tau = 0.2$  s, [38].  $T_n = 0.14$  s,  $T_v = 3.6$  s,  $T_p = 0.3$  s, and  $K_c = 0.013$  rad/m are found by applying the ‘cross-over’ assumption, [38], for the considered vehicle and tyre model, Table 1 and Figure 2, at regular cornering for a normal acceleration of  $a_n = 8$  m/s<sup>2</sup>.

As the vehicle increases in sideslip, after the powerslide manoeuvre has been initiated, the driver applies countersteer, which effectively reduces the tyre sideslip angle at the front wheels and the yaw moment, until no net yaw moment is produced, [39]. Then, the vehicle is stabilised at the desired vehicle sideslip angle, and there results a small offset

between steering angle and vehicle sideslip angle. The countersteer task after the initiation of the powerslide manoeuvre is represented by an additional *countersteer layer* imposing a (human) lag steering behaviour  $\Delta\delta_{cs}$

$$G_{cs}(s) = \frac{\delta_{cs}(s)}{\Delta\beta(s)} = K_{cs} \frac{1}{1 + T_1 s} e^{-s\tau} \quad (14)$$

with time constant  $T_1 \approx T_n$  and  $K_{cs}$  to finally match the steering angle of the demanded powerslide equilibrium.  $\Delta\beta$  is the developing deviation of the current vehicle sideslip angle from the vehicle sideslip angle at initial regular cornering.

## 4.2. Simulation

A simulated powerslide manoeuvre of the closed-loop ‘vehicle–driver–driver assistance system’, utilising the vehicle model described in Section 2 and the driver model and the driver assistance system described in Section 4, is shown in Figure 11. The virtual test driver tracks a circular path with radius  $R = 60$  m on a surface with tyre–road friction potential  $\mu = 1$ . Starting in regular driving condition, the powerslide is initiated at time  $t = 5$  s by setting up a demanded vehicle sideslip angle ramp to  $\beta_{des} = -35^\circ$  with a rate of  $10^\circ/\text{s}$ . The left top plot in Figure 11 shows this ramp. The controller is able to track the demanded vehicle sideslip angle very well. During the initialisation phase, the controller shifts all drive torque to the rear until the maximum total drive torque is reached, left bottom plot, resulting in large traction forces at the rear axle, and the vehicle starts to turn into the corner, right bottom plot. At the end of this period, the total drive torque has settled down to its equilibrium value related to the final steady-state powerslide motion. The virtual test driver countersteers and compensates path deviation, right top plot, with additional steering input. Obviously, the states converge to the powerslide equilibrium, which has been successfully stabilised, left middle plot.

A step-like external disturbance, represented as a reduction of the friction potential to  $\mu = 0.8$ , is applied at time  $t = 20$  s for a duration of 0.2 s, which is equivalent to a length of 4.6 m at the current velocity. Only small yaw oscillations appear, and only small steering corrections are required from the virtual test driver while the driver assistance system robustly compensates the friction potential disturbance by vigorously adapting the drive torque distribution  $\gamma$ , left bottom plot in Figure 11.

## 4.3. Experiment

The driver assistance system was also tested in real application at different tyre–road surface conditions, on dry asphalt, wet asphalt, and packed ice ( $\mu \approx 1 - 0.6 - 0.25$ ). The experiments were conducted with an AWD vehicle with individual electric motors at the front and the rear axles, with vehicle parameters similar to Table 1. While the vehicle sideslip angle  $\beta$  was measured with an external GNSS/INS system, other signals were recorded from the internal bus system of the vehicle.

To initiate the powerslide with the driver assistance system, the driver applies and keeps full throttle, starting at regular cornering conditions. The driver assistance system increases the drive torque at the rear axle to linearly ramp-up the vehicle side slip angle  $\beta$  to the desired vehicle side slip angle  $\beta_{des}$ , while the driver has to countersteer to keep the desired

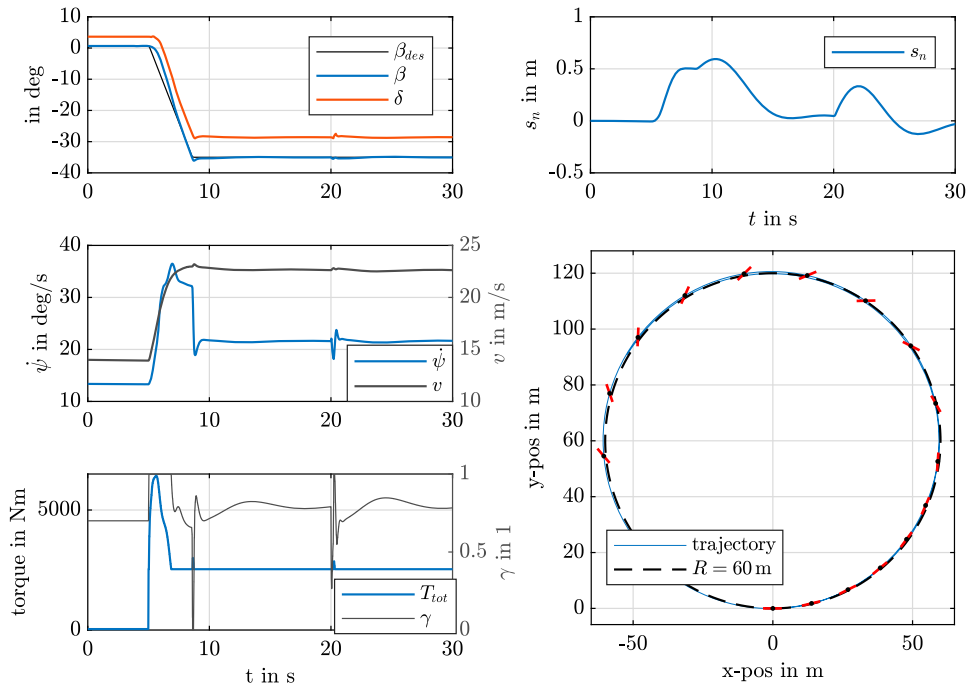


**Figure 11.** Simulation of powerslide initiation, stabilisation and disturbance compensation for radius  $R = 60$  m, desired vehicle sideslip angle  $\beta_{des} = -35^\circ$ , tyre-road friction potential  $\mu = 1$ ; nominal drive torque distribution  $\gamma_0 = 0.8$ ; control gains  $a_1 = 40,000$  Nm/rad,  $a_2 = 17,000$  Nms/rad.

reference trajectory. During the sustained powerslide, the driver assistance system controls the torque of each axle by changing parameters on the drive control unit of the vehicle to maintain the desired vehicle sideslip angle  $\beta_{des}$ , while the human driver tracks the reference trajectory by controlling the steering angle  $\delta$ . The driver terminates the powerslide by releasing the accelerator pedal. Recovery from the powerslide to normal driving is not yet implemented and has to be accomplished by the driver, as the focus of the experiments is put on the general powerslide stabilisation task and the interaction of the proposed driver assistance system with the human driver.

In Figure 12, measurement data are presented for a powerslide manoeuvre conducted on dry asphalt. The desired vehicle sideslip angle is set to  $\beta_{des} = -30^\circ$ . One can see that the controller of the driver assistance system very closely adjusts both the initial ramp and the desired constant vehicle sideslip angle. The steering angle of the human driver for tracking the circular path is quite smooth, top plot. Both the yaw rate  $\dot{\psi}$  and the vehicle velocity  $v$ , centre plot, converge to their steady-state values. The yaw rate is oscillating, probably due to time delays in the vehicle bus system and inertial effects of the drive train, which are not considered in the simple controller.

The bottom plot of Figure 12 shows the front and rear axle torques,  $T_F$  and  $T_R$ , and the drive torque distribution  $\gamma$ . The drive torque distribution oscillates w.r.t. the nominal drive torque distribution  $\gamma_0 \approx 0.7$ . Due to the high friction potential on dry asphalt and the limited maximum motor torques of the test vehicle, the radius  $R \approx 20$  m of the circular path was small at this test manoeuvre.

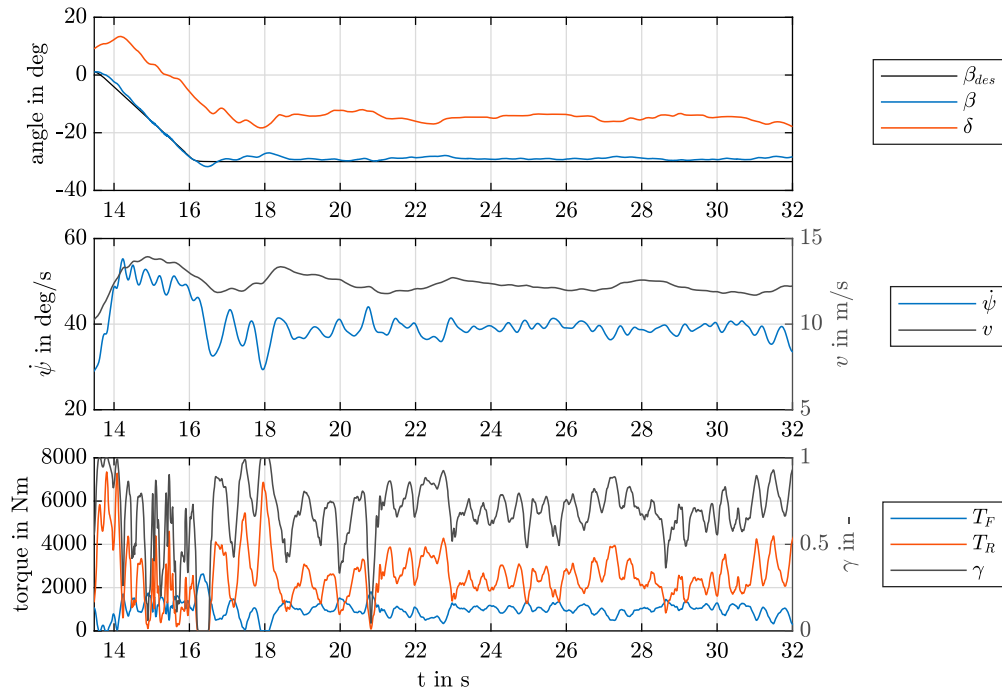


**Figure 12.** Measurement results from powerslide initiation and stabilisation with human driver/driver assistance system when tracking a circular path of radius  $R \approx 20$  m on dry asphalt (tyre–road friction potential  $\mu \approx 1$ ).

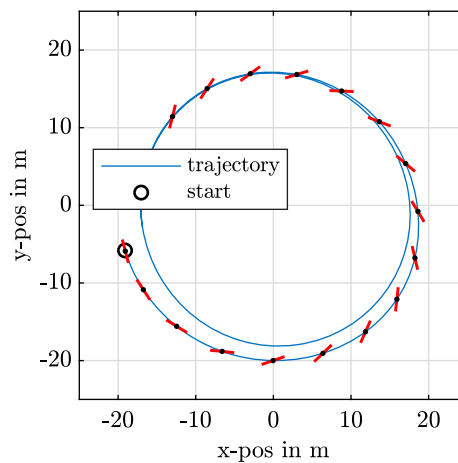


**Figure 13.** Measured trajectory of the CG of the vehicle and vehicle centre line corr. to Figure 12.

The resulting trajectory of the vehicle’s centre of gravity CG and the vehicle position are illustrated in Figure 13. It was easy for the driver to track the circular path or eventually increase/decrease the radius, as the driver was relieved from the stabilisation task of the unstable powerslide motion.

## 5. Conclusions

The characteristic properties of the powerslide motion for an all-wheel drive (electric) vehicle with individual motors at the front and rear axles have been investigated. Besides the steering angle input, the effectiveness of the drive train in stabilising the unstable steady-state powerslide motion has been analysed. In addition to the steering angle and the total drive torque input, the distribution of the total drive torque between the front and rear axles is an effective ‘actuator’ for the stabilisation task.

The controllability analysis reveals that the control strategy for stabilising the powerslide motion with the total drive torque depends on the (nominal) drive torque distribution. With decreasing drive torque distribution front:rear (here at about 25:75), the strategy has to be changed from an ‘RWD-strategy’ to an ‘AWD-strategy’, where the total drive torque has to be increased to reduce or stabilise the yaw rate and vehicle sideslip angle, in opposite to the ‘RWD-strategy’. The loss of controllability of the unstable powerslide mode with the total drive torque input indicates the (constant) drive torque distribution, where the strategy has to be changed.

Another interesting observation is that the total drive torque that stabilises the unstable ‘yaw mode’ and thus the vehicle sideslip angle at an AWD vehicle in powerslide motion, does not automatically stabilise the unstable ‘velocity mode’, in contrast to the stable velocity zero-dynamics of a RWD vehicle.

Both simulation and experimental results show that a basic (linear) PD-controller is sufficient to stabilise and maintain a powerslide motion by drive torque distribution control while the (human) driver just tracks the circular path.

To improve robustness concerning changes in the tyre–road friction potential or differences in human driver behaviour, first results from applying a machine learning-based control approach appear to be very promising, [40].

## Acknowledgments

We thank the ÖAMTC Fahrtechnikzentrum Wachau for providing the track for testing and measurements. We acknowledge TU Wien Bibliothek for financial support through its Open Access Funding Program.

## Disclosure statement

No potential conflict of interest was reported by the author(s).

## Funding

We acknowledge TU Wien Bibliothek for financial support through its Open Access Funding Program.

## References

- [1] Edelmann J, Plöchl M. Handling characteristics and stability of the steady-state powerslide motion of an automobile. *Regul Chaot Dyn.* 2009;14(6):682–692. doi: [10.1134/S1560354709060069](https://doi.org/10.1134/S1560354709060069)
- [2] Edelmann J, Plöchl M. Controllability of the powerslide motion of vehicles with different drive concepts. *Procedia Eng.* 2017;199:3266–3271. X International Conference on Structural Dynamics, EURO DYN 2017. doi: [10.1016/j.proeng.2017.09.357](https://doi.org/10.1016/j.proeng.2017.09.357)

- [3] Velenis E, Tsiotras P, Lu J. Modeling aggressive maneuvers on loose surfaces: the cases of trail-braking and pendulum-turn. In: 2007 European Control Conference (ECC); Kos, Greece. IEEE; 2007. p. 1233–1240. doi: [10.23919/ECC.2007.7068670](https://doi.org/10.23919/ECC.2007.7068670)
- [4] Velenis E, Tsiotras P. Minimum time vs maximum exit velocity path optimization during cornering. In: Proceedings of the IEEE International Symposium on Industrial Electronics, 2005. ISIE 2005; Vol. 1; Dubrovnik, Croatia; 2005. p. 355–360. doi: [10.1109/ISIE.2005.1528936](https://doi.org/10.1109/ISIE.2005.1528936)
- [5] Tavernini D, Massaro M, Velenis E, et al. Minimum time cornering: the effect of road surface and car transmission layout. Veh Sys Dyn. 2013;51(10):1533–1547. doi: [10.1080/00423114.2013.813557](https://doi.org/10.1080/00423114.2013.813557)
- [6] Berntorp K, Olofsson B, Bernhardsson B, et al. Models and methodology for optimal vehicle maneuvers applied to a hairpin turn. In: 2013 American Control Conference; Washington, USA; 2013. p. 2139–2146. doi: [10.1109/ACC.2013.6580152](https://doi.org/10.1109/ACC.2013.6580152)
- [7] Olofsson B, Lundahl K, Berntorp K, et al. An investigation of optimal vehicle maneuvers for different road conditions. IFAC Proc Vol. 2013;46(21):66–71. doi: [10.3182/20130904-4-JP-2042.00007](https://doi.org/10.3182/20130904-4-JP-2042.00007)
- [8] Acosta M, Kanarachos S, Blundell M. Vehicle agile maneuvering: from rally drivers to a finite state machine approach. In: 2016 IEEE Symposium Series on Computational Intelligence (SSCI); Athens, Greece; 2016. p. 1–8. doi: [10.1109/SSCI.2016.7850095](https://doi.org/10.1109/SSCI.2016.7850095)
- [9] Acosta M, Kanarachos S, Fitzpatrick ME. On full MAGV lateral dynamics exploitation: autonomous drift control. In: 2018 IEEE 15th International Workshop on Advanced Motion Control (AMC); Tokyo. IEEE; 2018. p. 529–534. doi: [10.1109/AMC.2019.8371149](https://doi.org/10.1109/AMC.2019.8371149)
- [10] Stano P, Tavernini D, Montanaro U, et al. Enhanced active safety through integrated autonomous drifting and direct yaw moment control via nonlinear model predictive control. IEEE Trans Intell Veh. 2024;9(2):4172–4190. doi: [10.1109/TIV.2023.3340992](https://doi.org/10.1109/TIV.2023.3340992)
- [11] Zhao T, Yurtsever E, Chladny R, et al. Collision avoidance with transitional drift control. In: 2021 IEEE International Intelligent Transportation Systems Conference (ITSC); Indianapolis, USA; 2021. p. 907–914. doi: [10.1109/ITSC48978.2021.9564496](https://doi.org/10.1109/ITSC48978.2021.9564496)
- [12] Zhao T, Yurtsever E, Rizzoni G. Justifying emergency drift control for automated vehicles. IFAC-PapersOnLine. 2022;55(24):141–148. 10th IFAC Symposium on Advances in Automotive Control AAC 2022; doi: [10.1016/j.ifacol.2022.10.275](https://doi.org/10.1016/j.ifacol.2022.10.275)
- [13] Ono E, Hosoe S, Tuan HD, et al. Bifurcation in vehicle dynamics and robust front wheel steering control. IEEE Trans Control Syst Technol. 1998;6(3):412–420. doi: [10.1109/87.668041](https://doi.org/10.1109/87.668041)
- [14] Della Rossa F, Mastinu G, Piccardi C. Bifurcation analysis of an automobile model negotiating a curve. Veh Syst Dyn. 2012;50(10):1539–1562. doi: [10.1080/00423114.2012.679621](https://doi.org/10.1080/00423114.2012.679621)
- [15] Hindiyeh RY, Gerdes JC. Equilibrium analysis of drifting vehicles for control design. In: Dynamic Systems and Control Conference; Vol. 48920; Hollywood, USA; 2009. p. 181–188. doi: [10.1115/DSCC2009-2626](https://doi.org/10.1115/DSCC2009-2626)
- [16] Steindl A, Edelmann J, Plöchl M. Influence of tyre characteristics on periodic motions for an understeering vehicle. PAMM. 2023;22(1):e202200289. doi: [10.1002/pamm.202200289](https://doi.org/10.1002/pamm.202200289)
- [17] Edelmann J, Eberhart M, Steindl A, et al. Post-critical behaviour of the powerslide motion. Veh Syst Dyn. 2024. submitted.
- [18] Velenis E, Frazzoli E, Tsiotras P. Steady-state cornering equilibria and stabilisation for a vehicle during extreme operating conditions. Int J Veh Auton Syst. 2010;8(2-4):217–241. doi: [10.1504/IJVAS.2010.035797](https://doi.org/10.1504/IJVAS.2010.035797)
- [19] Velenis E. FWD vehicle drifting control: the handbrake-cornering technique. In: 2011 50th IEEE Conference on Decision and Control and European Control Conference; Orlando, USA; 2011. p. 3258–3263. doi: [10.1109/CDC.2011.6161195](https://doi.org/10.1109/CDC.2011.6161195)
- [20] Velenis E, Katzourakis D, Frazzoli E, et al. Steady-state drifting stabilization of RWD vehicles. Control Eng Pract. 2011;19(11):1363–1376. doi: [10.1016/j.conengprac.2011.07.010](https://doi.org/10.1016/j.conengprac.2011.07.010)
- [21] Werling M, Reinisch P, Gröll L. Robust power-slide control for a production vehicle. Int J Veh Auton Syst. 2015;13(1):27–42. doi: [10.1504/IJVAS.2015.070727](https://doi.org/10.1504/IJVAS.2015.070727)
- [22] Voser C, Hindiyeh RY, Gerdes JC. Analysis and control of high sideslip manoeuvres. Veh Syst Dyn. 2010;48(S1):317–336. doi: [10.1080/00423111003746140](https://doi.org/10.1080/00423111003746140)

- [23] Chaichaowarat R, Wannasuphprasit W. Optimal control for steady state drifting of RWD vehicle. *IFAC Proc Vol.* 2013;46(21):824–830. doi: [10.3182/20130904-4-JP-2042.00055](https://doi.org/10.3182/20130904-4-JP-2042.00055)
- [24] Hindiyeh RY, Gerdes JC. Design of a dynamic surface controller for vehicle sideslip angle during autonomous drifting. *IFAC Proc Vol.* 2010;43(7):560–565. doi: [10.3182/20100712-3-DE-2013.00160](https://doi.org/10.3182/20100712-3-DE-2013.00160)
- [25] Goh JY, Gerdes JC. Simultaneous stabilization and tracking of basic automobile drifting trajectories. In: 2016 IEEE Intelligent Vehicles Symposium (IV); Gothenburg, Sweden; 2016. p. 597–602. doi: [10.1109/IVS.2016.7535448](https://doi.org/10.1109/IVS.2016.7535448)
- [26] Goh JY, Goel T, Christian Gerdes J. Toward automated vehicle control beyond the stability limits: drifting along a general path. *J Dyn Syst Meas Control.* 2019;142(2):021004. doi: [10.1115/1.4045320](https://doi.org/10.1115/1.4045320)
- [27] Goh JY, Thompson M, Dallas J, et al. Beyond the stable handling limits: nonlinear model predictive control for highly transient autonomous drifting. *Veh Syst Dyn.* 2024;62(10):2590–2613. doi: [10.1080/00423114.2023.2297799](https://doi.org/10.1080/00423114.2023.2297799)
- [28] Goel T, Goh JY, Gerdes JC. Opening new dimensions: vehicle motion planning and control using brakes while drifting. In: 2020 IEEE Intelligent Vehicles Symposium (IV); Las Vegas, USA; 2020. p. 560–565. doi: [10.1109/IV47402.2020.9304728](https://doi.org/10.1109/IV47402.2020.9304728)
- [29] Hou X, Zhang J, Ji Y, et al. Autonomous drift controller for distributed drive electric vehicle with input coupling and uncertain disturbance. *ISA Trans.* 2022;120:1–17. doi: [10.1016/j.isatra.2021.03.009](https://doi.org/10.1016/j.isatra.2021.03.009)
- [30] Nakano H, Okayama K, Kinugawa J, et al. Control of an electric vehicle with a large sideslip angle using driving forces of four independently-driven wheels and steer angle of front wheels. In: 2014 IEEE/ASME International Conference on Advanced Intelligent Mechatronics; Besacon, France; 2014. p. 1073–1078. doi: [10.1109/AIM.2014.6878223](https://doi.org/10.1109/AIM.2014.6878223)
- [31] Pacejka H. *Tire and vehicle dynamics*. 2nd ed. Oxford: Elsevier; 2005.
- [32] Plöchl M, Edelmann J. Driver models in automobile dynamics application. *Veh Syst Dyn.* 2007;45(7-8):699–741. doi: [10.1080/00423110701432482](https://doi.org/10.1080/00423110701432482)
- [33] Hamdan AMA, Nayfeh AH. Measures of modal controllability and observability for first- and second-order linear systems. *J Guid Control Dyn.* 1989;12(3):421–428. doi: [10.2514/3.20424](https://doi.org/10.2514/3.20424)
- [34] Choi JW, Lee JG, Kim Y, et al. Design of an effective controller via disturbance accommodating left eigenstructure assignment. *J Guid Control Dyn.* 1995;18(2):347–354. doi: [10.2514/3.21390](https://doi.org/10.2514/3.21390)
- [35] Lunze J. *Regelungstechnik 2*. Berlin, Heidelberg: Springer Vieweg; 2016.
- [36] Milani S, Marzbani H, Jazar RN. Vehicle drifting dynamics: discovery of new equilibria. *Veh Syst Dyn.* 2022;60(6):1933–1958. doi: [10.1080/00423114.2021.1887499](https://doi.org/10.1080/00423114.2021.1887499)
- [37] Edelmann J, Plöchl M, Reinalter W, et al. A passenger car driver model for higher lateral accelerations. *Veh Syst Dyn.* 2007;45(12):1117–1129. doi: [10.1080/00423110701203644](https://doi.org/10.1080/00423110701203644)
- [38] Mitschke M, Wallentowitz H. *Dynamik der Kraftfahrzeuge*. Berlin, Heidelberg: Springer Vieweg; 2004.
- [39] Abdulrahim M. On the dynamics of automobile drifting. SAE Technical Paper; 2006.
- [40] Jaumann F, Schuster T, Unterreiner M, et al. Powerslide control with deep reinforcement learning. In: Mastinu G, Braghin F, Cheli F, et al., editors. 16th International Symposium on Advanced Vehicle Control; Cham. Springer Nature Switzerland; 2024. p. 862–868. doi: [10.1007/978-3-031-70392-8\\_121](https://doi.org/10.1007/978-3-031-70392-8_121)

## Paper B

### *Post-critical behaviour of the powerslide motion*

TU Wien: Johannes Edelmann, Manuel Eberhart, Alois Steindl, Manfred Plöchl  
*Vehicle System Dynamics*, February 2025  
<https://doi.org/10.1080/00423114.2025.2471346>

**Keywords:** Loss of stability, bifurcation, vehicle handling behaviour, stability of motion, powerslide, drifting

**Abstract:** It is a challenge to control the vehicle motion when tyre forces at the rear axle are saturated and the sideslip angle of the vehicle is large. At the steady-state cornering condition called powerslide or drifting, the front wheels are steered to the outside of the curve, and the corresponding equilibrium is unstable. While previous and ongoing research concentrates above all on different stabilisation approaches, the post-critical behaviour is given attention in this study. Based on the nonlinear system equations of a basic two-wheel vehicle and brush tyre model, it is found that for a range of constant steering angles and constant drive torques at the rear driven wheels, the vehicle motion and states converge to a steady-state with a small radius of curvature or to a stable limit cycle orbiting an unstable equilibrium.

## Post-critical behaviour of the powerslide motion

Johannes Edelmann, Manuel Eberhart, Alois Steindl  and Manfred Plöchl

Institute of Mechanics and Mechatronics, TU Wien, Vienna, Austria

### ABSTRACT

It is a challenge to control the vehicle motion when tyre forces at the rear axle are saturated and the sideslip angle of the vehicle is large. At the steady-state cornering condition called powerslide or drifting, the front wheels are steered to the outside of the curve, and the corresponding equilibrium is unstable. While previous and ongoing research concentrates above all on different stabilisation approaches, the post-critical behaviour is given attention in this study. Based on the nonlinear system equations of a basic two-wheel vehicle and brush tyre model, it is found that for a range of constant steering angles and constant drive torques at the rear driven wheels, the vehicle motion and states converge to a steady-state with a small radius of curvature or to a stable limit cycle orbiting an unstable equilibrium.

### ARTICLE HISTORY

Received 15 June 2024  
Revised 9 December 2024  
Accepted 7 February 2025

### KEYWORDS

Loss of stability; bifurcation;  
vehicle handling behaviour;  
stability of motion;  
powerslide; drifting

### 1. Introduction

Pushing vigorously the accelerator pedal of a rear-wheel drive (RWD) vehicle during cornering reduces the lateral forces of the rear axle. The resulting change of yaw moment then turns the vehicle's longitudinal axis towards the inside of the corner, causing a large sideslip angle of the vehicle. The driver may now balance the motion by steering the front wheels to the outside of the corner, called countersteer. The established equilibrium is a possible solution of steady-state cornering and is called powerslide motion, [1], or simply drifting.

It is found in [2] that the existence of the powerslide motion is above all a phenomenon of the tyre characteristics, in particular of the degressive behaviour of the lateral forces at large longitudinal slip. Linearisation of the nonlinear equations of motion of a RWD vehicle and tyre model reveals that the powerslide equilibrium is unstable, [2]. Analysis of the eigenvector related to the positive real (and therefore unstable) eigenvalue shows a strong coupling between the longitudinal and the lateral vehicle states, [3,4].

It is reported in [5] that the unstable powerslide equilibrium, derived from a 3-DOF vehicle model, including longitudinal velocity, lateral velocity, and yaw rate, is a saddle point with characteristics that exhibit low sensitivity to friction potential and speed variation. At the powerslide equilibrium, non-minimum phase characteristics appear between steering angle and vehicle sideslip angle, which could facilitate destabilisation due to the right half zero, [6]. Therefore it is suggested to better control vehicle sideslip by controlling

**CONTACT** Johannes Edelmann  [johannes.edelmann@tuwien.ac.at](mailto:johannes.edelmann@tuwien.ac.at)

© 2025 The Author(s). Published by Informa UK Limited, trading as Taylor & Francis Group.  
This is an Open Access article distributed under the terms of the Creative Commons Attribution License (<http://creativecommons.org/licenses/by/4.0/>), which permits unrestricted use, distribution, and reproduction in any medium, provided the original work is properly cited.  
The terms on which this article has been published allow the posting of the Accepted Manuscript in a repository by the author(s) or with their consent.

the yaw rate or even by applying longitudinal control that allows also to sustain a drifting motion. In [4] it is found from controllability analysis that the control of the rear wheel torque is very effective in stabilising the powerslide motion, which can also be observed from the power thrusts of the driver when drifting.

While the stabilisation of the unstable powerslide equilibrium, either fully autonomously, [7–11], by the driver, [12], or with shared control, [13], has drawn a lot of attention by researchers, only little attention has been given to the dynamics of the vehicle after loss of stability with fixed control inputs. Therefore, this paper aims to close this gap and contribute to a better understanding of the post-critical behaviour of the powerslide motion. It builds on the conference paper [14] of the authors.

The remainder of this paper is organised as follows: Section 2 introduces the applied vehicle model with RWD and the tyre model used to map the nonlinear tyre characteristics. In Section 3 the post-critical behaviour is studied. Therefore, the vehicle motion after loss of stability is illustrated, the handling diagram focussing the powerslide branch is analysed in detail, and a bifurcation analysis is performed and discussed to outline and explain the resulting periodic vehicle motion. Measurement results that support the theoretical findings are included as well. Finally, the main outcome of the paper is summarised, and conclusions are drawn.

## 2. Tyre and vehicle model

A two-wheel vehicle model with RWD is used to map the powerslide motion and the dynamic behaviour after loss of stability. This model is particularly reasonable at low-friction surfaces when the load transfer between the left and the right wheels is less important and may thus be neglected. The vehicle model in powerslide condition is plotted in Figure 1. The velocity  $v$ , the sideslip angle  $\beta$  of the vehicle and the yaw rate  $\dot{\psi}$  constitute, together with the angular velocity  $\omega_R$  of the rear wheel, the state variables of the system. The system control inputs are the steering angle  $\delta_F$  of the front wheel and the drive torque  $M_R$  at the rear wheel.

The nonlinear equations of motion of the vehicle and the rear wheel are

$$m\dot{v} \cos \beta - m(\dot{\psi} + \dot{\beta})v \sin \beta = F_{xR} - F_{yF} \sin \delta_F, \quad (1a)$$

$$m\dot{v} \sin \beta + m(\dot{\psi} + \dot{\beta})v \cos \beta = F_{yR} + F_{yF} \cos \delta_F, \quad (1b)$$

$$I_z \ddot{\psi} = F_{yF} \cos \delta_F l_F - F_{yR} l_R, \quad (1c)$$

$$I_w \dot{\omega}_R = M_R - F_{xR} r_l, \quad (1d)$$

with vehicle mass  $m$ , yaw moment of inertia  $I_z$  of the vehicle, moment of inertia  $I_w$  of the rear axle, the distances  $l_F$  and  $l_R$  from the centre of gravity (COG) to the front, and to the rear axle, respectively, and the loaded radius  $r_l$  of the rear wheel.

Also for the sake of simplicity, the brush tyre model from [15] is chosen to represent the tyre characteristics, including typically less realistic assumptions, such as the same lateral and longitudinal tyre slip stiffness. The horizontal tyre forces  $F_{yF}, F_{xR}, F_{yR}$  depend on the sideslip angles  $\alpha_i$ , the longitudinal slips  $\kappa_i$ , and the vertical tyre loads  $F_{zi}$  with  $i = F, R$ . The normalised steady-state tyre/axle characteristics are shown in Figure 2 for the theoretical slips  $\sigma_{xi} = \kappa_i / (1 + \kappa_i)$  and  $\sigma_{yi} = \tan \alpha_i / (1 + \kappa_i)$ , see Appendix. The characteristics of the

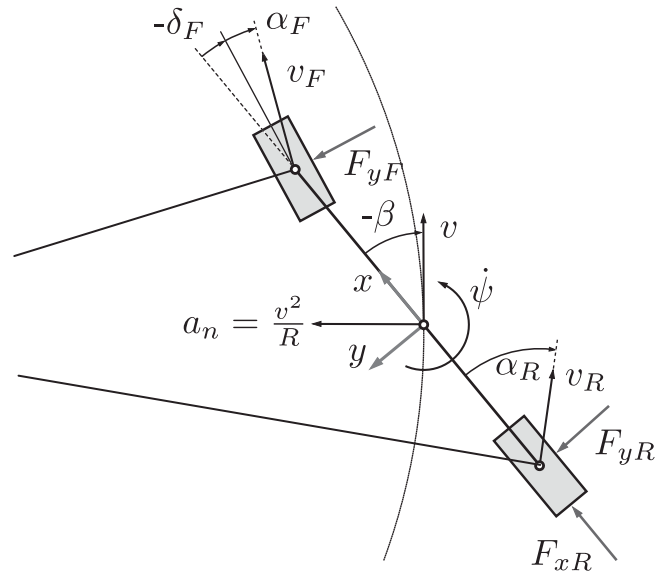


**Figure 1.** Powerslide driving condition for rear-wheel drive vehicle model.

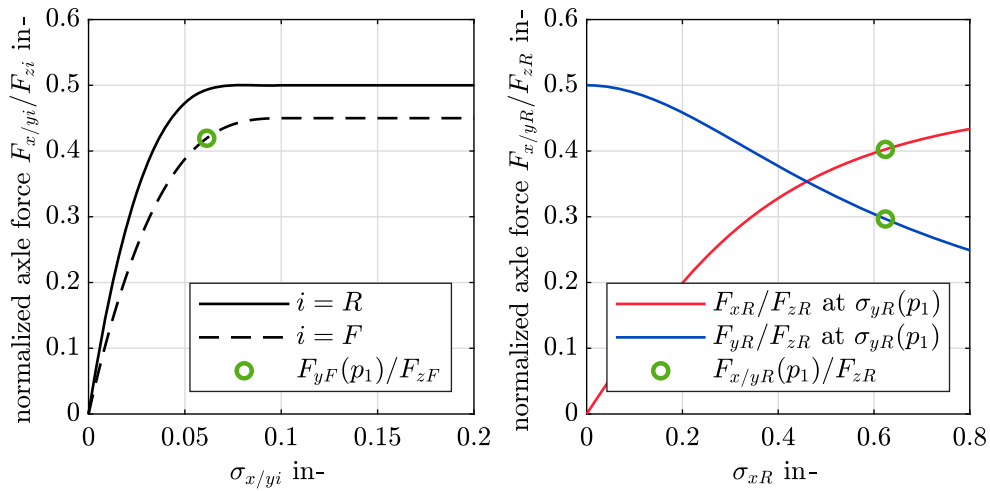


**Figure 2.** Normalised tyre/axle characteristics with marked normalised tyre/axle forces at powerslide equilibrium  $p_1$ .

front and the rear tyre/axle are different and result in a slightly understeer vehicle, see later Figure 3. On the left of Figure 2 the ‘stronger’ rear axle with respect to the front axle can be noticed. For the same constant sideslip angle, the decrease of the rear lateral axle force with increasing longitudinal slip is presented on the right, and the corresponding tyre/axle forces associated with the later addressed powerslide equilibrium  $p_1$  are marked.

The parameters used for the numeric results in Section 3 are listed in Table 1.

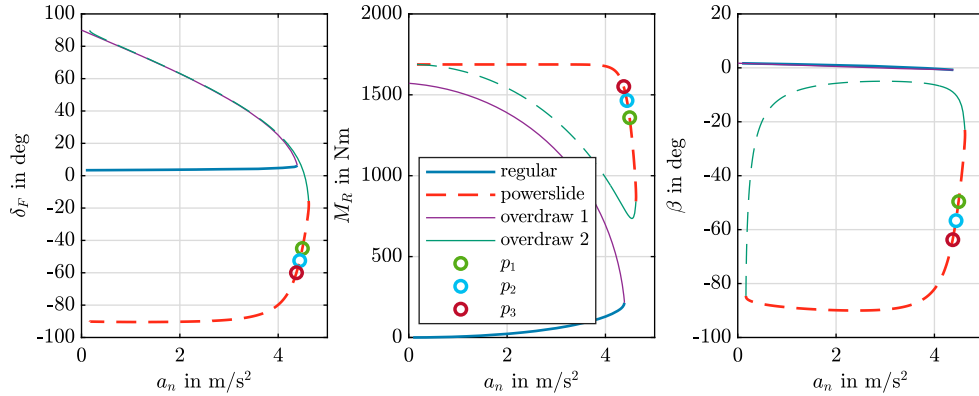


**Figure 3.** Handling diagram with regular driving and powerslide branch for constant radius (50 m) cornering (solid lines: stable solutions; dashed line: unstable solutions).

**Table 1.** Parameters of the two-wheel vehicle and tyre/axle model.

parameter	symbol	value	unit
vehicle mass	$m$	2000	kg
yaw inertia of inertia	$I_z$	2650	kg m <sup>2</sup>
moment of inertia of rear axle	$I_w$	6	kg m <sup>2</sup>
distance of COG to front axle	$l_F$	1.45	m
distance of COG to rear axle	$l_R$	1.50	m
loaded radius of rear wheel	$r_l$	0.35	m
effective rolling radius of rear tyre	$r_e$	0.35	m
front tyre/axle slip stiffness	$2c_{pF}a_F^2$	$9 \cdot 10^4$	N
rear tyre/axle slip stiffness	$2c_{pR}a_R^2$	$6.5 \cdot 10^4$	N
max. friction coefficients	$\mu_F, \mu_R$	0.45, 0.5	–

### 3. Stability of powerslide equilibrium and post-critical dynamic behaviour

The required steering angle, drive torque at the rear axle and vehicle sideslip angle for quasi-steady-state cornering at a constant radius of 50 m are shown in the handling diagram in Figure 3. Besides the equilibria of the regular driving branch and the powerslide branch, overdraw solutions, which are not relevant in this context, are depicted. Note that slightly larger normal accelerations can be reached in powerslide motion. The requested drive torque is larger than for regular driving, thus the powerslide motion is less energy-efficient.

The required drive torque at the rear axle in powerslide motion increases in a quite proportional manner with steering angle within the range of practical interest, Figure 4, which can be useful information for the human driver to control the powerslide. The powerslide equilibria  $p_1$ ,  $p_2$ , and  $p_3$  marked in Figures 3 and 4 are analysed below w.r.t. the corresponding post-critical behaviour in detail.

Now, the system equations are linearised at the equilibria on the powerslide branch. The resulting four eigenvalues and corresponding eigenvectors for varied normal accelerations are shown in Figure 5, with equilibrium  $p_1$  marked again. The positive eigenvalue, red line, reveals the unstable nature of the powerslide branch and its eigenvector the relatively strong coupling of the generalised coordinates in longitudinal ( $v, \omega_R$ ) and lateral ( $\psi, \beta$ )

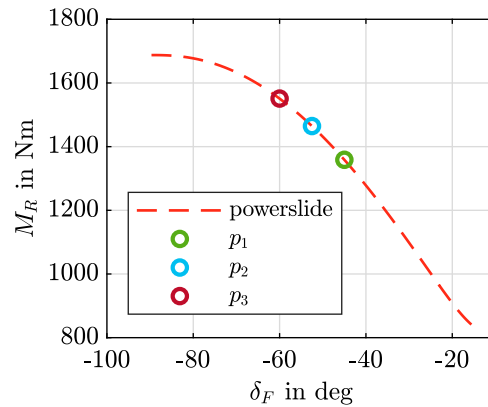


**Figure 4.** Relationship between the steering angle and the rear drive torque corresponding to Figure 3 for the (unstable) powerslide branch.

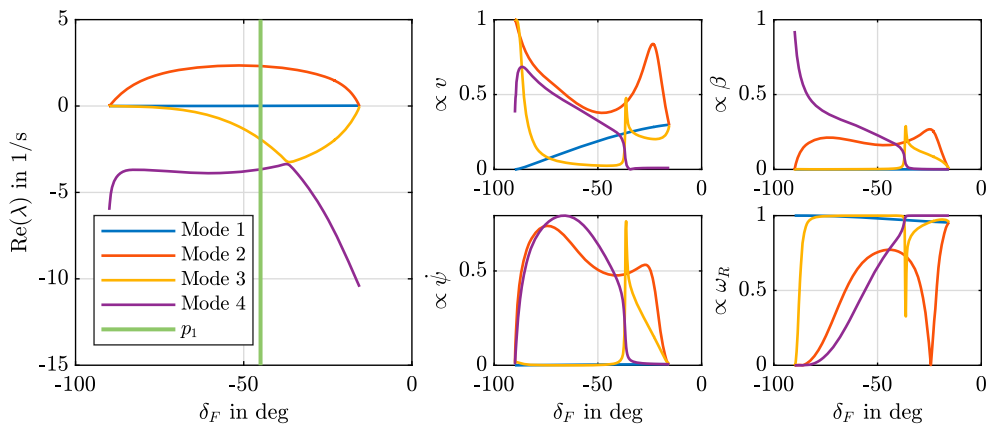


**Figure 5.** Eigenvalues and corresponding eigenvectors corresponding to Figure 3 for the powerslide branch.

directions. The results are similar to [4], where a four-wheel vehicle model and a detailed tyre model are applied.

As the positive eigenvalue is real, a monotonic loss of stability, with the vehicle spinning in or out, can be expected to appear. But interestingly, simulations of the vehicle motion after loss of stability at a wide range of powerslide equilibria show that the vehicle will end up in flower-like, periodic motions, see trajectories in Figure 6, for fixed control inputs. Drivers may know this phenomenon from their own experience when they keep both the steering angle and accelerator pedal fixed and draw tyre marks on the surface. The green flower refers again to the green powerslide equilibrium  $p_1$ , and the other trajectories to the powerslide equilibria marked in the handling diagram in Figure 3 and the relationship between steering angle and drive torque in Figure 4 with  $p_2$  and  $p_3$ .

The COG of the vehicle may deviate to the inside or the outside of the circle closely after a loss of stability. The following approach may be applied to decide about the direction, and it is illustrated in an example.

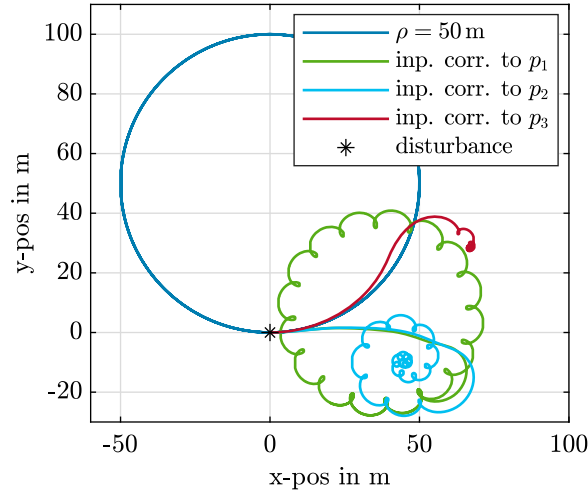


**Figure 6.** Trajectories of the COG of the vehicle after loss of stability at powerslide equilibria  $p_1, p_2, p_3$  and initial trajectories referring to a given disturbance at position '\*' addressed in the *Example*.

For the considered powerslide branch, a pair of unstable complex conjugate eigenvalues and two real eigenvalues, with one unstable, appear, Figure 5. This positive real eigenvalue will govern the evolution of the system (1) with state vector

$$\mathbf{x} = [v, \beta, \dot{\psi}, \omega_R]^T. \quad (2)$$

The powerslide equilibrium is denoted with state vector  $\mathbf{x}_0$ , and the radius of the traced circle is

$$\varrho = v/\dot{\psi}. \quad (3)$$

If the initial state vector  $\mathbf{x}(0)$  is given by

$$\mathbf{x}(0) = \mathbf{x}_0 + \varepsilon \mathbf{v}_u, \quad (4)$$

where  $\mathbf{v}_u$  denotes the eigenvector corresponding to the dominant unstable eigenvalue  $\lambda_u$ , the trajectory will evolve initially according to

$$\mathbf{x}(t) = \mathbf{x}_0 + \exp(\lambda_u t) \varepsilon \mathbf{v}_u. \quad (5)$$

For  $\varrho(t)$  one obtains the relation

$$\dot{\varrho} = \frac{\dot{v}\dot{\psi} - v\ddot{\psi}}{\dot{\psi}^2}. \quad (6)$$

With  $\dot{\mathbf{x}}(0) = \lambda_u \varepsilon \mathbf{v}_u$  there follows

$$\dot{\varrho}(0) = \lambda_u \varepsilon \frac{v_{u,1} \dot{\psi}(0) - v(0) v_{u,3}}{\dot{\psi}^2(0)}, \quad (7)$$

where  $v_{u,k}$  denotes the  $k$ th component of  $\mathbf{v}_u$ . For  $\dot{\varrho}(0) > 0$ , the circle will grow initially.

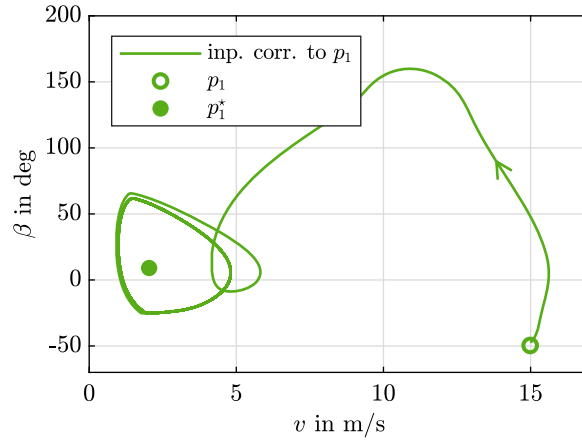


**Figure 7.** Trajectory in the  $(v, \beta)$ -phase plane after loss of stability: from (disturbed) powerslide equilibrium  $p_1$  towards encircling the unstable equilibrium  $p_1^*$ .

If the initial state  $\mathbf{x}(0)$  lies close to the powerslide equilibrium state  $\mathbf{x}_0$ , its component in the dominating unstable direction is given by the projection of  $\mathbf{d}_0 = \mathbf{x}(0) - \mathbf{x}_0$  into the direction of  $\mathbf{v}_u$ . If

$$\mathbf{V} = [\mathbf{v}_1, \mathbf{v}_2, \dots, \mathbf{v}_n = \mathbf{v}_u]$$

denotes the matrix of eigenvectors with  $\mathbf{v}_u$  in the last column, the coefficient  $c_u$  of  $\mathbf{d}_0$  w.r.t. the eigenvector basis is given by

$$c_u = \mathbf{W}_n \mathbf{d}_0, \quad (8)$$

where  $\mathbf{W}_n$  denotes the last line of  $\mathbf{W} = \mathbf{V}^{-1}$ . This follows from the relation  $\mathbf{d}_0 = \mathbf{V}\mathbf{c}$ . The calculation of the inverse matrix may be avoided by using the left eigenvectors.  $c_u$  is then used for  $\varepsilon$  in (7).

Now, as an *Example*, a disturbance  $\Delta\beta = \pm 3^\circ$  of the sideslip angle of the vehicle with respect to its steady-state value in powerslide motion with equilibria  $p_1, p_2$  and  $p_3$  is considered at an arbitrary time instant  $t = 0$ . The resulting initial trajectories are included in Figure 6. For  $\Delta\beta = -3^\circ$ , the vehicle will leave the circle to the outside after loss of stability, green and blue trajectory. In contrast, for  $\Delta\beta = 3^\circ$ , the vehicle will turn inside, red trajectory in Figure 6.

Looking at the green trajectory of the COG in the  $x$ - $y$ -plane in Figure 6 and at the green trajectory in the  $(v, \beta)$ -phase plane starting from the (disturbed) equilibrium  $p_1$  in Figure 7 suggests that the trajectories converge to a stable periodic solution encircling a further equilibrium  $p_1^*$ .

This equilibrium  $p_1^*$  coexists with the stationary equilibrium  $p_1$  for the same control inputs. Deriving further  $p_i^*$  corresponding to respective  $p_i$  on the powerslide branch, by using the continuation method MATCONT, [16], results in a new branch that is depicted on the top plot in Figure 8 by the black line. The equilibria  $p_i^*$  on this branch undergo Hopf bifurcations at the Hopf points  $H_1$  and  $H_2$ . In between, stable limit cycles evolve.

From the above, it becomes clear that after the monotonic loss of stability at the powerslide equilibrium, the motion finally results in a stable periodic motion. The three pairs

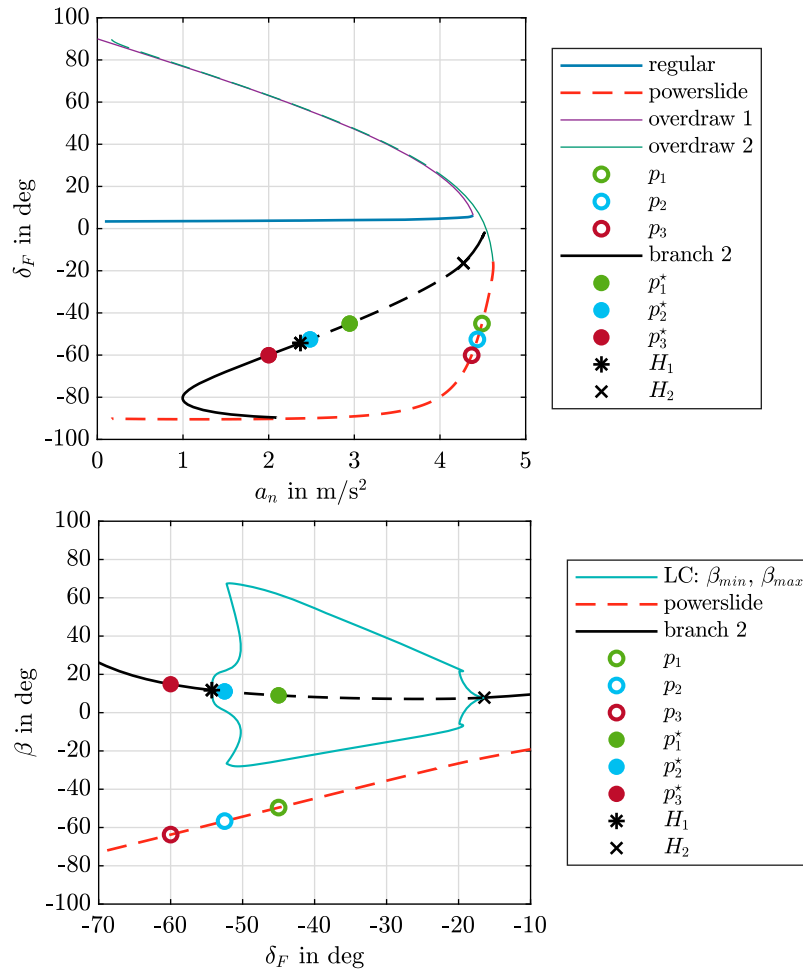


**Figure 8.** Handling and bifurcation diagram (solid lines: stable solutions; dashed line: unstable solutions).

of equilibria,  $p_j$  and  $p_j^*$ ,  $j = 1-3$ , are included in the handling diagram and the respective branch of the bifurcation diagram at the bottom plot of Figure 8, with the steering angle as the bifurcation parameter. The bifurcation diagram depicts the maximum and minimum values of the sideslip angles of the vehicle at the limit cycles. With increasing (negative) steering angle, the branch of unstable equilibria  $p_i^*$  turns stable at Hopf point  $H_1$ . This is interesting to note, as for very large (negative) steering angles (and large drive torques, Figure 4), even a stable, stationary solution ( $p_3^*$ ) as a circular trajectory with a small radius of curvature on the  $x$ - $y$ -plane may appear (and may be noticed as ‘donut’ marks on the surface). Figure 9 shows these small radii of the solutions, in particular when they turn stable after the Hopf point  $H_1$ . While the regular driving and powerslide equilibria are related to the given radius of 50 m in the handling diagram at the top plot of Figure 8, the graph with equilibria  $p_i^*$  is related to the varying radii presented in Figure 9.

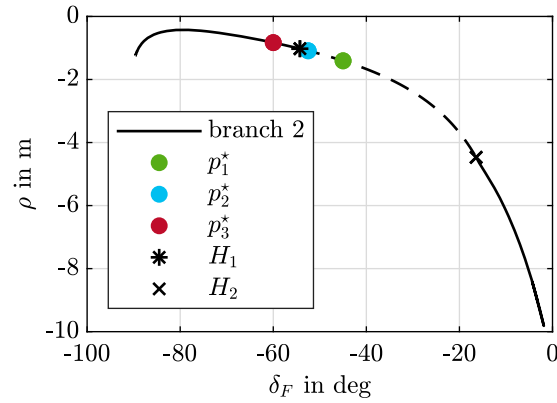


**Figure 9.** Bifurcation diagram with the steering angle  $\delta_F$  as bifurcation parameter for the radius of curvature  $\rho$  (solid lines: stable solutions; dashed line: unstable solutions).

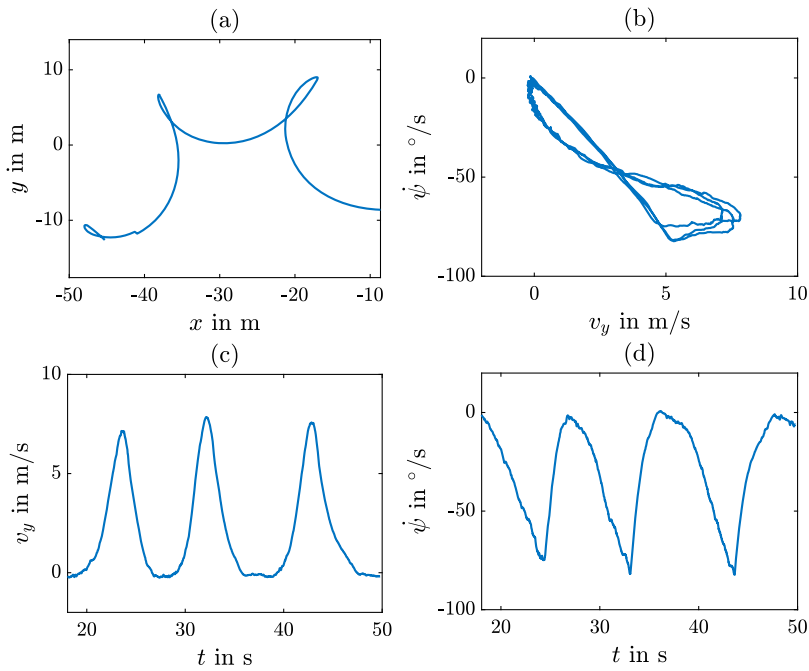


**Figure 10.** Measured signals of the vehicle motion after loss of stability with fixed control inputs  $\delta_F \approx -9^\circ$  and  $M_R \approx 1000 \text{ Nm}$ : (a) trajectory of COG in  $x$ - $y$ -plane; (b)  $(\dot{\psi}, v_y)$ -phase plane; (c) yaw rate  $\dot{\psi}(t)$ ; (d) lateral velocity  $v_y(t)$ .

To confirm the occurrence of a periodic motion after the loss of stability with fixed control inputs, also respective vehicle tests were carried out. The tests were performed on packed snow with an SUV-type electric vehicle with a motor at the front axle and a motor at the rear axle with locked differential. Actually for other test purposes, the motor torques could be controlled freely. To mimic an RWD vehicle, the front axle motor torque was set to a minimum, and the rear axle torque was controlled to achieve a demanded torque. Next

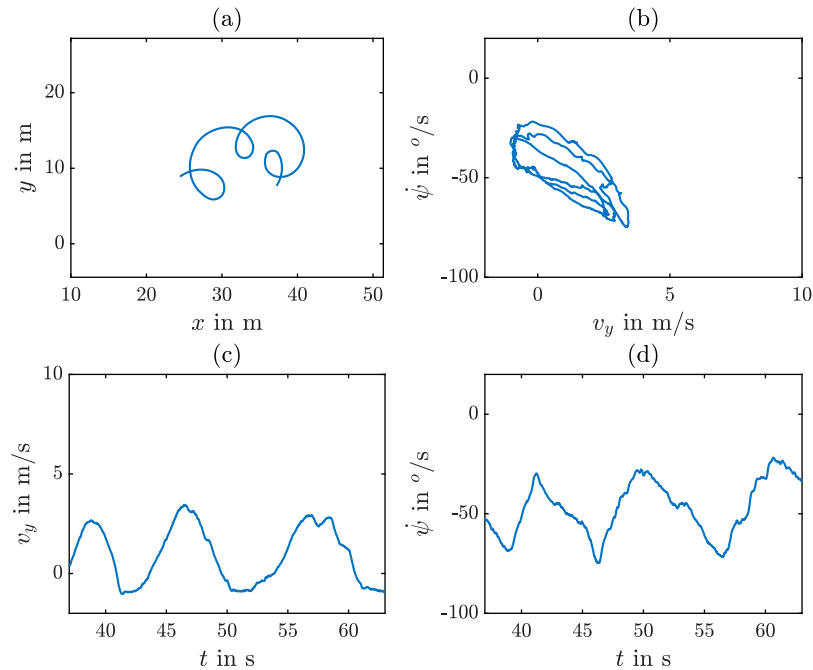


**Figure 11.** Measured signals of the vehicle motion after loss of stability with fixed control inputs  $\delta_F \approx -38^{\circ}$  and  $M_R \approx 1350 \text{ Nm}$ : (a) trajectory of COG in  $x$ - $y$ -plane; (b)  $(\dot{\psi}, v_y)$ -phase plane; (c) yaw rate  $\dot{\psi}(t)$ ; (d) lateral velocity  $v_y(t)$ .

to the signals on the vehicle data bus, a high-precision dual antenna GNSS-aided Inertial Measuring Unit (GNSS-IMU) was available as a measuring system in particular for the lateral velocity of the vehicle. Winter tyres of different dimensions were mounted on the front and rear axles. The vehicle and tyre/road friction parameters match only roughly to the parameters given in Table 1.

The test manoeuvres were initiated when the driver (continuously) fully pushed the accelerator pedal, which allowed the torque control to modulate the torque request and set a demanded value while the driver countersteered for stabilisation in the initial phase and then kept the steering hand wheel fixed in approximate powerslide motion.

Figures 10 and 11 show the measured results of two of the test manoeuvres. While the first manoeuvre relates to a powerslide motion with a small steering and vehicle sideslip angle, the second manoeuvre relates to large angles. As model parameters and parameters of the test condition are different to some extent, the measurement results correspond only roughly to the above derived characteristics. Nevertheless, the graphs reveal that the vehicle indeed runs into limit cycles in both test manoeuvres, which becomes most obvious from the trajectories in the  $(\dot{\psi}, v_y)$ -phase plane in (b) and the periodic time histories of the yaw rate  $\dot{\psi}(t)$  in (c) and the lateral velocity  $v_y(t) = v(t) \sin \beta(t)$  in (d). Also, flower-like trajectories of the COG in the  $x$ - $y$ -plane appear, see (a). The vehicle had to be stopped (e.g. on the left side of the plot (a) in Figure 10), and so the drawing of a full flower due to limited space. The centre of the unstable equilibrium cannot be spotted anyway because of naturally occurring (e.g. frictional) disturbances on the one hand and the unstabilised vehicle

states on the other hand. For the test manoeuvre with the large steering angle, Figure 11, the periodicity is more disturbed than in Figure 10 but still evident.

#### 4. Conclusions

The loss of stability of a vehicle in powerslide motion (i.e. when drifting) is of monotonic nature due to a typically dominant positive real eigenvalue of the system, linearised w.r.t. the powerslide equilibrium. The yaw rate of the vehicle will start to increase or decrease depending on the disturbance. Then, there will be a transition from the powerslide equilibrium to another equilibrium for the same fixed controls. For very large (negative) steering angles, this equilibrium may be stable, and the vehicle will end again in steady-state cornering with a typically small radius, but with different states compared to the corresponding steady-state cornering in powerslide condition. For smaller steering angles, the equilibrium will be unstable and of oscillatory nature and a respective Hopf bifurcation is found. The resulting stable limit cycles of the vehicle states appear as flower-like trajectories on the road plane, where the COG of the vehicle spirals around a fixed point.

While recent studies mainly focus on controlling or stabilising the powerslide, the loss of stability and its consequences still needed to be addressed. The findings in this paper build on theoretical research, but evidence from practical observations and first vehicle test runs suggests the plausibility of the results.

From a practical application point of view, trajectories of the COG and vehicle states in the time period (closely) after the loss of stability seem to be most important, as the powerslide and related trajectories that would not be feasible with regular driving are becoming more relevant in recent and future research, e.g. [11].

#### Acknowledgments

We acknowledge TU Wien Bibliothek for financial support through its Open Access Funding Program.

#### Disclosure statement

No potential conflict of interest was reported by the author(s).

#### ORCID

Alois Steindl  <http://orcid.org/0000-0002-6813-2486>

#### References

- [1] Edelmann J, Plöchl M, Lugner P, et al. Investigations on the powerslide of automobiles. In: 9th International Symposium on Advanced Vehicle Control (AVEC'08); 2008 Oct 6–9; Kobe, Japan. Available from: <https://repositum.tuwien.at/handle/20.500.12708/65776>.
- [2] Edelmann J, Plöchl M. Handling characteristics and stability of the steady-state powerslide motion of an automobile. *Regul Chaotic Dyn.* 2009;14(6):682–692. doi: [10.1134/S1560354709060069](https://doi.org/10.1134/S1560354709060069).
- [3] Edelmann J, Plöchl M. Controllability of the powerslide motion of an automobile with different actuation inputs. *PAMM.* 2016;16:803–804. doi: [10.1002/pamm.201610390](https://doi.org/10.1002/pamm.201610390).

- [4] Edelmann J, Plöchl M. Controllability of the powerslide motion of vehicles with different drive concepts. *Procedia Eng.* 2017;199:3266–3271. doi: [10.1016/j.proeng.2017.09.357](https://doi.org/10.1016/j.proeng.2017.09.357).
- [5] Hindiyeh RY, Gerdes JC. Equilibrium analysis of drifting vehicles for control design. In: ASME 2009 Dynamic Systems and Control Conference; 2009 Oct 12–14; Hollywood, California, USA. p. 181–188.
- [6] Voser C, Hindiyeh RY, Gerdes JC. Analysis and control of high sideslip manoeuvres. *Veh Syst Dyn.* 2010;48(sup1):317–336. doi: [10.1080/00423111003746140](https://doi.org/10.1080/00423111003746140).
- [7] Werling M, Reinisch P, Gröll L. Robust power-slide control for a production vehicle. *Int J Veh Auton Syst.* 2015;13(1):27–42. doi: [10.1504/IJVAS.2015.070727](https://doi.org/10.1504/IJVAS.2015.070727).
- [8] Goh JY, Gerdes JC. Simultaneous stabilization and tracking of basic automobile drifting trajectories. In: 2016 IEEE Intelligent Vehicles Symposium (IV); 2016; Gothenburg, Sweden. p. 597–602.
- [9] Vignati M, Sabbioni E, Cheli F. A torque vectoring control for enhancing vehicle performance in drifting. *Electronics.* 2018;7(12):394. doi: [10.3390/electronics7120394](https://doi.org/10.3390/electronics7120394).
- [10] Goh JY, Goel T, Gerdes JC. Toward automated vehicle control beyond the stability limits: drifting along a general path. *J Dyn Syst-T Asme.* 2020;142(2):Article ID 021004. doi: [10.1115/1.4045320](https://doi.org/10.1115/1.4045320)
- [11] Stano P, Tavernini D, Montanaro U, et al. Enhanced active safety through integrated autonomous drifting and direct yaw moment control via nonlinear model predictive control. *IEEE Trans Intell Veh.* 2023;9(2):4172–4190. doi: [10.1109/TIV.2023.3340992](https://doi.org/10.1109/TIV.2023.3340992).
- [12] Edelmann J, Plöchl M, Pfeffer P. Analysis of steady-state vehicle handling and driver behaviour at extreme driving conditions. In: Proceedings of 22st International Symposium on Dynamics of Vehicles on Roads and Tracks (IAVSD 2011); 2011; Manchester, UK. Available from: <https://repositum.tuwien.at/handle/20.500.12708/66338>.
- [13] Eberhart M, Plöchl M, Unterreiner M, et al. Insights into stability and control of the powerslide motion with variable drive torque distribution – applied to a driver assistance system. *Veh Syst Dyn.* 2025;1–21. doi: [10.1080/00423114.2025.2457433](https://doi.org/10.1080/00423114.2025.2457433).
- [14] Steindl A, Edelmann J, Plöchl M. Influence of tyre characteristics on periodic motions for an understeering vehicle. *PAMM.* 2023;22(1):e202200289. doi: [10.1002/pamm.20220289](https://doi.org/10.1002/pamm.20220289).
- [15] Pacejka HB. *Tire and vehicle dynamics*. 3rd ed. Oxford Waltham: Butterworth-Heinemann Elsevier; 2012.
- [16] Dhooge A, Govaerts W, Kuznetsov YA. MatCont: a matlab package for numerical bifurcation analysis of ODEs. *ACM Trans Math Softw.* 2003;29(2):141–164. doi: [10.1145/779359.779362](https://doi.org/10.1145/779359.779362).

## Appendix. Tyre model

The brush tyre model in [15] is applied for the front and rear tyre characteristics. Here, the model equations for the rear tyre are given in a compact manner; the model equations for the front tyre are similar but ‘pure lateral’. In contrast to [15], no practical slips  $\kappa$  and  $\tan \alpha$  are introduced, but the theoretical slips,

$$\sigma_{xR} = -\frac{v_{sxR}}{|r_e \omega_R|}, \quad \sigma_{yR} = -\frac{v_{syR}}{|r_e \omega_R|}, \quad \sigma_R = \sqrt{\sigma_{xR}^2 + \sigma_{yR}^2}, \quad (A1)$$

with longitudinal and lateral slip velocities  $v_{sxR}$  and  $v_{syR}$ ,

$$v_{sxR} = v \cos \beta - r_e \omega_R \quad \text{and} \quad v_{syR} = v \sin \beta - l_R \dot{\psi}, \quad (A2)$$

are directly related to the kinematics of the vehicle model. Then, the magnitude of the rear tyre/axle force  $F_R$  reads

$$F_R = \begin{cases} \mu_R F_{zR} (3\theta_R \sigma_R - 3(\theta_R \sigma_R)^2 + (\theta_R \sigma_R)^3) & \text{for } \sigma_R \leq \sigma_{sR} \\ \mu_R F_{zR} & \text{for } \sigma_R > \sigma_{sR} \end{cases} \quad (A3)$$

with slip  $\sigma_{slR} = 1/\theta_R$  where total sliding starts and parameter

$$\theta_R = \frac{2c_{pR}a_R^2}{3\mu_R F_{zR}}. \quad (\text{A4})$$

Finally, the longitudinal and lateral components of the rear tyre/axle force are

$$F_{xR} = F_R \frac{\sigma_{xR}}{\sigma_R} \quad \text{and} \quad F_{yR} = F_R \frac{\sigma_{yR}}{\sigma_R}. \quad (\text{A5})$$

## Paper C

*Stability boundaries and bifurcation analysis of an AWD vehicle: the influence of the drive torque distribution*

TU Wien: Manuel Eberhart, Manfred Plöchl, Johannes Edelmann  
*Nonlinear Dynamics*, Volume 113, p. 20943–20957  
<https://doi.org/10.1007/s11071-025-11232-x>

**Keywords:** vehicle handling, vehicle dynamics, all-wheel drive, stability, bifurcation analysis, drive torque distribution, Takens–Bogdanov bifurcation

**Abstract:** All-wheel drive electric vehicles, equipped with independent motors at the front axle and the rear axle, allow for adaptive drive torque distribution between the axles to influence handling and stability characteristics. To analyse manoeuvres at combined longitudinal and lateral accelerations, a quasi-steady-state assumption is used to apply bifurcation and continuation techniques. Different types of loss of stability are found and analysed. The Takens–Bogdanov bifurcation is studied in more detail, and it is shown that the respective branch represents the boundary between final understeer and final oversteer, and defines the stable envelope in the GG diagram. The drive torque distribution at the Takens–Bogdanov branch is therefore considered a good design criterion for a safe and performant powertrain control. Besides the Takens–Bogdanov branch, related Hopf and Fold branches are identified that define limits for practically reasonable drive torque distributions.



RESEARCH

# Stability boundaries and bifurcation analysis of an AWD vehicle: the influence of the drive torque distribution

Manuel Eberhart · Manfred Plöchl · Johannes Edelmann

Received: 5 February 2025 / Accepted: 8 April 2025 / Published online: 22 May 2025  
© The Author(s) 2025

**Abstract** All-wheel drive electric vehicles, equipped with independent motors at the front axle and the rear axle, allow for adaptive drive torque distribution between the axles to influence handling and stability characteristics. To analyse manoeuvres at combined longitudinal and lateral accelerations, a quasi-steady-state assumption is used to apply bifurcation and continuation techniques. Different types of loss of stability are found and analysed. The Takens–Bogdanov bifurcation is studied in more detail, and it is shown that the respective branch represents the boundary between final understeer and final oversteer, and defines the stable envelope in the GG diagram. The drive torque distribution at the Takens–Bogdanov branch is therefore considered a good design criterion for a safe and performant powertrain control. Besides the Takens–Bogdanov branch, related Hopf and Fold branches are identified that define limits for practically reasonable drive torque distributions.

**Keywords** Vehicle handling · Vehicle dynamics · All-wheel drive · Stability · Bifurcation analysis · Drive torque distribution · Takens–Bogdanov bifurcation

## 1 Introduction

Powertrains of electric vehicles are often equipped with more than one electric motor. Since the individual motors are not mechanically coupled and very responsive, they offer new possibilities for vehicle control systems. Considering the mutual influence of longitudinal and lateral tyre forces, the drive torques may improve the responsiveness and stability properties of the vehicle. However, for this purpose, a profound understanding of the impact of the drive torque distribution on the stability and handling properties of the vehicle is required to ensure effective and safe operation. The focus of this paper is to gain a better understanding of the influence of the front-to-rear drive torque distribution of an all-wheel drive (AWD) vehicle with two independent motors, one at the front axle and one at the rear axle, on its stability properties and quasi-steady-state handling performance. Therefore, the handling regime at combined longitudinal and lateral acceleration of the vehicle is considered, where the impact of longitudinal tyre forces on lateral tyre forces and consequently the front-to-rear drive torque distribution may modify handling and stability characteristics considerably.

The (quasi-)steady-state handling characteristics of vehicles are fundamentally important to assess its (open loop) stability properties and to judge the vehicle's response to driver steering commands, [1–3]. Depending on the longitudinal acceleration, both in driving and braking conditions, and the powertrain and control architecture, the handling characteristics and stability

---

M. Eberhart (✉) · M. Plöchl · J. Edelmann  
Institute of Mechanics and Mechatronics, TU Wien, Getreide-  
markt 9, 1060 Vienna, Austria  
e-mail: manuel.eberhart@tuwien.ac.at

properties of the vehicle can significantly change, [4–6].

In [4], Klomp et al. analyse the impact of all-wheel drive (AWD), front-wheel drive (FWD) and rear-wheel drive (RWD) powertrain architectures on the handling characteristics and lateral acceleration potential of a vehicle. For this purpose, a method is proposed to determine an ‘optimal’ drive torque distribution using a quasi-steady-state description of the vehicle model.

Bucchi et al. [7] and Lenzo et al. [8] compare FWD and RWD vehicles with a focus on handling and yaw torque analysis. It is shown that an FWD powertrain is less prone to understeer in steady-state cornering due to the additional yaw torque of the longitudinal forces at the front axle.

Using a basic two degrees of freedom (DOF) vehicle model and a simplified Pacejka ‘Magic Formula’ tyre model, Ono et al. [9] show that vehicle loss of stability is caused by a saddle-node bifurcation (also denoted Fold bifurcation), which depends considerably on the rear lateral tyre force saturation. A steering control strategy is proposed to stabilise the motion of the vehicle.

A study on vehicle dynamics and stability, taking into account different friction potentials of the tyres at the front axle and the rear axle, is presented by Shen et al. in [10]. The joint point locus approach is applied to identify system equilibrium points and to assess their stability characteristics.

A fundamental study on a two DOF vehicle model is done by Della Rossa et al. in [11]. Various types of loss of stability for different combinations of effective tyre force characteristics at the front axle and the rear axle of the vehicle model are studied and discussed with the help of bifurcation analysis and the phase-plane diagram.

The impact of the effective tyre force characteristics on the stability behaviour of a vehicle are studied by Pauwelussen in [12], focusing on the appearance of limit cycles, whereas Farroni et al. investigate its influence on the handling diagram and on the phase-plane diagram in [13].

Horiuchi et al. [5] use a quasi-steady-state description to model a vehicle in combined lateral and longitudinal acceleration conditions. Using the steering angle as the bifurcation parameter, a Fold bifurcation is found for a vehicle under negative longitudinal acceleration and a fixed brake torque distribution.

Wang et al. analyse the stability properties of a vehicle at combined braking and steering in [14]. The sta-

bility of the vehicle is analysed for different speeds, steering angles and brake torques with the help of bifurcation analysis, equivalent equilibrium description and phase-plane analysis for an ideal constant brake distribution between the front axle and the rear axle.

In contrast to conventional brake systems, regenerative braking using electric motors allows for a variable brake force distribution between the front axle and the rear axle and may allow to extend the combined stable longitudinal and lateral acceleration envelope in the GG diagram.

Besides improving the stable handling envelope, in certain conventional and critical driving conditions, the control of the drive torque distribution may be beneficial to enhance the responsiveness of the vehicle. A ‘responsiveness and stability metric’ is used by Zang et al. [15] to control the front-to-rear drive torque distribution for improved responsiveness and stability properties of the vehicle.

To study the properties of the lateral motion of the vehicle during longitudinal acceleration, the quasi-steady-state assumption (equivalent equilibrium) is applied to convert the transient condition into a mechanical equivalent steady-state. This transformation allows for the use of mathematical methods used for linear systems. Horiuchi et al. consider the front-to-rear load transfer and longitudinal tyre forces in [5] by adding a virtual external force to the equation of motion of the vehicle in the longitudinal direction. Abe applies a quasi-steady-state assumption in [6], disregarding the change of the longitudinal velocity of the vehicle for a short period of time. Also, the vehicle roll, pitch and yaw motion are assumed to maintain their steady states. Klomp et al. use a similar approach in [4]. Tremlett et al. in [16] and Novellis et al. in [17] additionally require that the derivative of the longitudinal slip of each wheel is zero, whereas the lateral and yaw motion fulfil the steady-state condition.

In the literature, vehicle stability properties are analysed using basic vehicle models, either assuming steady-state conditions or combined longitudinal and lateral acceleration, where stability properties are examined for specific, fixed drive or brake torque distributions.

The novelty of this paper is the incorporation of a variable drive torque distribution, an inherent feature of AWD electric vehicle powertrain architectures, to analyse its impact on the stability properties of the vehicle at combined longitudinal and lateral acceleration. There-

fore, a detailed vehicle model is applied to take relevant effects like the dynamics of the individual wheels, the wheel load transfer, and the mutual influence of longitudinal and lateral tyre forces into account.

The paper is structured as follows: In the subsequent Sect. 2, the vehicle and tyre model are introduced. In Sect. 3, the used methods are briefly described. In the following Sect. 4 the handling characteristics are shown and different types of loss of stability are identified. The Takens–Bogdanov bifurcation is shown in the GG envelope and different causes of its appearance and its connection to the occurrence of a Fold bifurcation are presented. In Sect. 5, main findings are summarised and conclusions are drawn.

### 2 Vehicle and tyre model

To study vehicle stability properties up to high levels of both lateral and longitudinal acceleration, a nonlinear 10 degrees of freedom vehicle model is employed, Fig. 1, incorporating a nonlinear tyre model, wheel load transfer, and nonlinear steering kinematics. The road surface is represented by a horizontal plane.

The vehicle body is modelled as a rigid body with 6 degrees of freedom, with mass  $m$  and moments of inertia  $I_x, I_y$  and  $I_z$ . The products of inertia are neglected. The vehicle body is connected to the massless axles with spring stiffnesses  $c_k$  and damping  $d_k, k \in \{F, R\}$ , at the front axle and rear axle, respectively. The anti-roll bars are considered by additional stiffnesses  $c_{rk}$ . The four individual wheels with effective moment of inertia  $I_{Wk}$  are modelled with one rotational degree of freedom each. The vehicle parameters are listed in Table 1. These refer to an SUV vehicle and are adjusted to measurements carried out with the reference vehicle.

The tyre force characteristics are described by Pacejka’s Magic Formula model [18], where tyre parameters are derived from trailer measurements and the slip stiffnesses and maximum friction values of the tyres are adjusted to fit the handling characteristics of the reference vehicle.

To reduce the complexity in the derivation of the governing equations of motion of the vehicle body, two different coordinate systems are used: the equations of motion for the rotational degrees of freedom are described in the body-fixed coordinate system  $(x_B-y_B-z_B)$ , whereas the equations of the translational degrees of freedom are described in a coordinate system moved

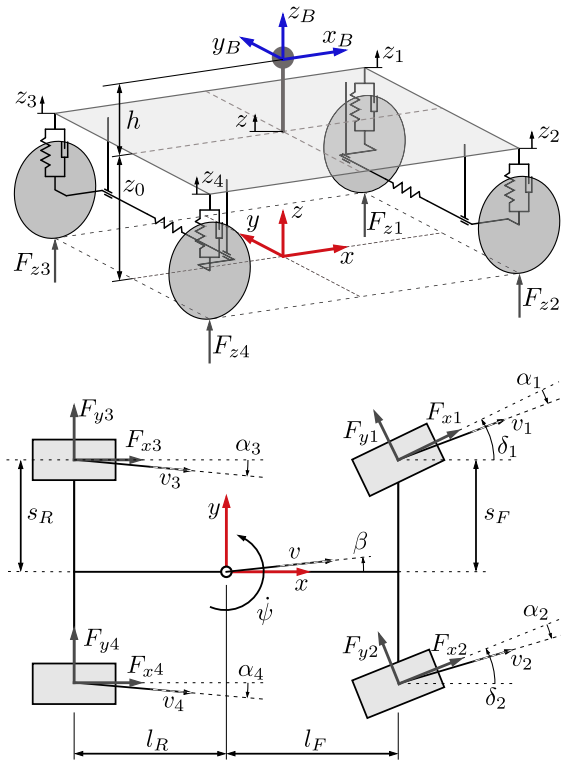


Fig. 1 Schematic illustration of the vehicle model

in the ground plane  $(x-y-z)$ . The body-fixed coordinate system  $(x_B-y_B-z_B)$  is rotated relative to the ground plane with pitch angle  $\theta$  and roll angle  $\varphi$  w.r.t. the  $y_B$ -axis and the  $x_B$ -axis, respectively. The equations of motions are derived assuming small angles  $\varphi$  and  $\theta$ , and respective derivatives,

$$m(\dot{v}_x - v_y \dot{\psi} + h \ddot{\theta}) + 2h \dot{\theta} \dot{\psi} - h \theta \dot{\psi}^2 + h \varphi \dot{\psi} = \Sigma F_x \tag{1a}$$

$$m(\dot{v}_y + v_x \dot{\psi} - h \ddot{\varphi}) + 2h \dot{\varphi} \dot{\psi} + h \varphi \dot{\psi}^2 + h \theta \dot{\psi} = \Sigma F_y \tag{1b}$$

$$m \dot{v}_z = \Sigma F_z \tag{1c}$$

$$I_x \ddot{\varphi} - (I_y - I_z) \dot{\theta} \dot{\psi} = \Sigma M_x - \theta \Sigma M_z \tag{1d}$$

$$I_y \ddot{\theta} - (I_z - I_x) \dot{\psi} \dot{\varphi} = \Sigma M_y + \varphi \Sigma M_z \tag{1e}$$

$$I_z \ddot{\psi} - (I_x - I_y) \dot{\varphi} \dot{\theta} = \Sigma M_z + \theta \Sigma M_x - \varphi \Sigma M_y \tag{1f}$$

with the longitudinal velocity  $v_x$ , lateral velocity  $v_y$ , yaw rate  $\dot{\psi}$ , and the sum of forces  $\Sigma F_j, j \in \{x, y, z\}$ , and of moments  $\Sigma M_j$ :

$$\Sigma F_x = F_{x1} \cos \delta_1 - F_{y1} \sin \delta_1 + F_{x2} \cos \delta_2 - F_{y2} \sin \delta_2 + F_{x3} + F_{x4} \quad (2a)$$

$$\Sigma F_y = F_{y1} \cos \delta_1 + F_{x1} \sin \delta_1 + F_{y2} \cos \delta_2 + F_{x2} \sin \delta_2 + F_{y3} + F_{y4} \quad (2b)$$

$$\Sigma F_z = F_{z1} + F_{z2} + F_{z3} + F_{z4} - m g \quad (2c)$$

$$\Sigma M_x = F_{z1} (s_F + h \varphi) - F_{z2} (s_F - h \varphi) + F_{z3} (s_R + h \varphi) - F_{z4} (s_R - h \varphi) + \Sigma F_y (h + z_0 + z) \quad (2d)$$

$$\Sigma M_y = -(F_{z1} + F_{z2}) (l_F - h \theta) + (F_{z3} + F_{z4}) (l_R + h \theta) - \Sigma F_x (h + z_0 + z) \quad (2e)$$

$$\Sigma M_z = \Sigma M_{z, \text{tyre}} + (F_{y1} \cos \delta_1 + F_{x1} \sin \delta_1 + F_{y2} \cos \delta_2 + F_{x2} \sin \delta_2) (l_F - h \theta) - (F_{y3} + F_{y4}) (l_R + h \theta) - (F_{x1} \cos \delta_1 - F_{y1} \sin \delta_1) (s_F + h \varphi) + (F_{x2} \cos \delta_2 - F_{y2} \sin \delta_2) (s_F - h \varphi) - F_{x3} (s_R + h \varphi) + F_{x4} (s_R - h \varphi). \quad (2f)$$

$F_{xi}$ ,  $i \in \{1, 2, 3, 4\}$ , represent the longitudinal tyre forces of the individual wheels, and  $F_{yi}$  represent the lateral tyre forces, which depend on the longitudinal tyre slips  $s_{xi}$ , sideslip angles  $\alpha_i$ , and the vertical tyre forces  $F_{zi}$ .  $\Sigma M_{z, \text{tyre}}$  represents the sum of the self-aligning torques  $M_{zi}$  of the tyres. The vertical tyre forces are calculated with

$$F_{z1} = F_{z1,0} - c_F z_1 - d_F \dot{z}_1 - c_{rF} (z_1 - z_2) \quad (3a)$$

$$F_{z2} = F_{z2,0} - c_F z_2 - d_F \dot{z}_2 + c_{rF} (z_1 - z_2) \quad (3b)$$

$$F_{z3} = F_{z3,0} - c_R z_3 - d_R \dot{z}_3 - c_{rR} (z_3 - z_4) \quad (3c)$$

$$F_{z4} = F_{z4,0} - c_R z_4 - d_R \dot{z}_4 + c_{rR} (z_3 - z_4) \quad (3d)$$

where  $F_{zi,0}$  represents the nominal vertical tyre forces. The wheel travels  $z_i$  are derived from the vertical displacement  $z$  of the vehicle body, the pitch angle  $\theta$  and the roll angle  $\varphi$ ,

$$z_1 = z + \varphi s_F - \theta l_F \quad (4a)$$

$$z_2 = z - \varphi s_F - \theta l_F \quad (4b)$$

$$z_3 = z + \varphi s_R + \theta l_R \quad (4c)$$

$$z_4 = z - \varphi s_R + \theta l_R \quad (4d)$$

From geometric and kinematic considerations, the tyre sideslip angles  $\alpha_i$  are derived,

$$\tan(\delta_1 - \alpha_1) = \frac{v_y + l_F \dot{\psi}}{v_x - s_F \dot{\psi}} \quad (5a)$$

$$\tan(\delta_2 - \alpha_2) = \frac{v_y + l_F \dot{\psi}}{v_x + s_F \dot{\psi}} \quad (5b)$$

$$\tan \alpha_3 = -\frac{v_y - l_R \dot{\psi}}{v_x - s_R \dot{\psi}} \quad (5c)$$

$$\tan \alpha_4 = -\frac{v_y - l_R \dot{\psi}}{v_x + s_R \dot{\psi}} \quad (5d)$$

Ackermann steering behaviour is assumed,

$$\frac{l_F + l_R}{\tan \delta_1} + s_F = \frac{l_F + l_R}{\tan \delta} \quad (6a)$$

$$\frac{l_F + l_R}{\tan \delta_2} - s_F = \frac{l_F + l_R}{\tan \delta} \quad (6b)$$

with the steering angle  $\delta$  and the steering angles  $\delta_{1,2}$  of the front wheels.

The longitudinal tyre slips  $s_{xi}$  are defined by

$$s_{x1} = \frac{r \omega_1}{v_{W1}} - 1 \quad (7a)$$

$$s_{x2} = \frac{r \omega_2}{v_{W2}} - 1 \quad (7b)$$

$$s_{x3} = \frac{r \omega_3}{(v_x - s_R \dot{\psi})} - 1 \quad (7c)$$

$$s_{x4} = \frac{r \omega_4}{(v_x + s_R \dot{\psi})} - 1 \quad (7d)$$

$v_{Wi}$  represent the velocities of the centre of the front wheels in the direction of the respective wheel plane,

$$v_{W1} = (v_x - s_F \dot{\psi}) \cos \delta_1 + (v_y + l_F \dot{\psi}) \sin \delta_1 \quad (8a)$$

$$v_{W2} = (v_x + s_F \dot{\psi}) \cos \delta_2 + (v_y + l_F \dot{\psi}) \sin \delta_2 \quad (8b)$$

with the angular velocities of the wheels  $\omega_i$  and tyre radius  $r$ .

The equation of motion of the wheels read

$$I_{Wk} \dot{\omega}_i = T_i - F_{xi} r, \quad (9)$$

with the effective moment of inertia  $I_{Wk}$ ,  $k \in \{F, R\}$ , which represents half of the reduced moment of inertia of the respective axle. Assuming open differential gears at both the front axle and the rear axle, the drive (or brake) torque  $T_i$  of the individual wheels is given by  $T_{1,2} = T_F/2$  and  $T_{3,4} = T_R/2$ , respectively.

The drive torque at the front axle and the rear axle,  $T_F$  and  $T_R$ , respectively, depends on the total drive torque  $T_{tot}$  requested by the driver (through throttle and brake pedal inputs) and the drive torque distribution  $\gamma$ . The drive torque distribution  $\gamma$  represents the ratio of the total drive torque  $T_{tot}$  that is applied to the rear axle,

$$\gamma = T_R/T_{tot}. \tag{10}$$

Consequently, the torque at the front axle and the rear axle are given by

$$T_F = (1 - \gamma) T_{tot} \quad \text{and} \quad T_R = \gamma T_{tot}. \tag{11}$$

In the figures presented in Sect. 4, instead of the longitudinal velocity  $v_x$  and the lateral velocity  $v_y$  of the origin of the  $x$ - $y$ - $z$  coordinate system, the velocity  $v$  and the sideslip angle  $\beta$  of the vehicle are depicted, were

$$v_x = v \cos \beta, \quad v_y = v \sin \beta. \tag{12}$$

This representation is more intuitive, offering a clearer understanding of the vehicle state being illustrated.

The longitudinal and lateral tyre forces,  $F_{xi}$  and  $F_{yi}$ , respectively, of the applied Magic Formula tyre model depend, as mentioned above, on the vertical tyre force  $F_{zi}$ , the tyre sideslip angle  $\alpha_i$ , and the longitudinal slip  $s_{xi}$ . The influence of the camber angle is neglected.

In Fig. 2 the normalized lateral tyre forces  $F_{yi}/F_{zi,0}$  are shown over the normalized longitudinal tyre forces  $F_{xi}/F_{zi,0}$  for constant sideslip angles  $\alpha$ . The characteristics of a front tyre are shown in solid lines and the characteristics of a rear tyre are shown in dash-dotted lines.

Examining the pure lateral tyre characteristics (i.e. the points where  $F_{xi}/F_{zi,0} = 0$  for different values of  $\alpha$  in Fig. 2) shows that the cornering stiffness of the front tyres is lower than the cornering stiffness of the rear tyres, due to different tyre dimensions considered. Both the maximum lateral and the longitudinal friction potentials are higher at the rear tyres compared to the front tyres.

With increasing longitudinal slip, the (local) cornering stiffness of the tyres decreases, significantly affecting the vehicle's handling and stability properties under combined lateral and longitudinal tyre slip conditions.

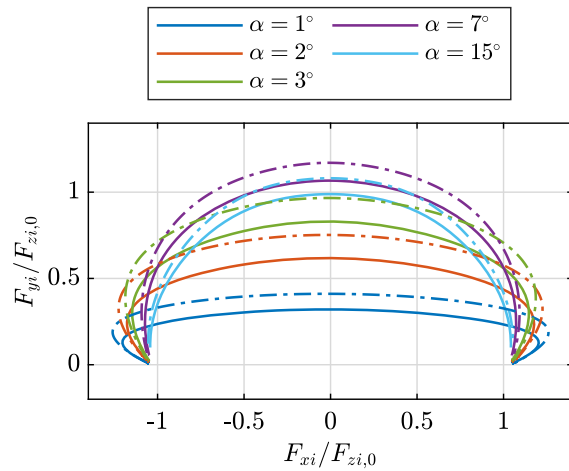


**Fig. 2** Combined normalized tyre forces for constant sideslip angles  $\alpha$  and varied longitudinal slip  $s_x$  for a front tyre,  $i \in \{1, 2\}$  (solid lines), and a rear tyre,  $i \in \{3, 4\}$  (dash-dotted lines)

### 3 Methods

To analyse the impact of the drive torque distribution  $\gamma$  on the stability properties of the vehicle during manoeuvres with combined lateral and longitudinal acceleration, the transient state ( $a_n \neq 0, a_t \neq 0$ ) is transformed to a quasi-steady-state that approximates the transient condition well, [4, 5, 16, 17].

#### 3.1 Quasi-steady-state description

Here, a similar approach to Horiuchi et al. [5] is used, where an equivalent longitudinal force is applied in the vehicle's longitudinal axis at the centre of gravity to transform the transient state during acceleration and braking into an equivalent equilibrium state. The derivative of the velocity of the vehicle,  $\dot{v}$ , is set to the desired tangential acceleration  $a_t$ . This adjustment is equivalent to applying an inertial force acting at the centre of gravity of the vehicle in the opposite direction of the velocity  $v$ . As a result, both the wheel load transfer and the longitudinal tyre forces required to achieve the desired tangential acceleration  $a_t$  are taken into account, allowing the vehicle to be considered in a steady-state condition.

The yaw acceleration  $\ddot{\psi}$ , the derivative of the vehicle sideslip angle  $\dot{\beta}$ , and the derivatives of the other states are set to zero to satisfy the steady-state condition. In contrast to [16] and [17], not the derivative of longitu-

**Table 1** Parameters of the vehicle model

Parameter	Value	Unit	Description
$m$	2550	kg	Total mass of the vehicle
$I_x$	950	kg m <sup>2</sup>	Moment of inertia about the $x$ -axis
$I_y$	3400	kg m <sup>2</sup>	Moment of inertia about the $y$ -axis
$I_z$	3600	kg m <sup>2</sup>	Moment of inertia about the $z$ -axis
$I_{WF}$	3.3	kg m <sup>2</sup>	Effective moment of inertia of one front wheel
$I_{WR}$	8	kg m <sup>2</sup>	Effective moment of inertia of one rear wheel
$l_F$	1.5	m	Length from the centre of gravity to the front axle
$l_R$	1.4	m	Length from the centre of gravity to the rear axle
$s_F$	0.84	m	Half of the track width at the front axle
$s_R$	0.83	m	Half of the track width at the rear axle
$z_0$	0.13	m	Height $z_0$
$h$	0.42	m	Height $h$
$r$	0.367	m	Radius of the tyre
$c_F$	$2.5 \times 10^4$	N/m	Spring stiffness at the front axle
$c_R$	$2.6 \times 10^4$	N/m	Spring stiffness at the rear axle
$d_F$	$5 \times 10^3$	N/(m s)	Damping constant at the front axle
$d_R$	$5 \times 10^3$	N/(m s)	Damping constant at the rear axle
$c_{rF}$	$3.5 \times 10^4$	N/m	Roll stiffness at the front axle
$c_{rR}$	$3.2 \times 10^4$	N/m	Roll stiffness at the rear axle

dinal tyre slips  $\dot{s}_{xi}$  but the angular acceleration of the wheels  $\dot{\omega}_i$  are set to zero.

### 3.2 Stability of first order

Once a solution of the nonlinear quasi-steady-state system is found, the nonlinear equations of motion are linearised w.r.t. this steady state,  $\Delta \dot{\mathbf{x}} = \mathbf{A} \Delta \mathbf{x} + \mathbf{B} \Delta \mathbf{u}$ , with state vector  $\Delta \mathbf{x}$  and (fixed) control parameter vector  $\Delta \mathbf{u}$ , and system matrix  $\mathbf{A}$  and input matrix  $\mathbf{B}$ . Lyapunov's first method implies that a steady state is stable if all eigenvalues of  $\mathbf{A}$  have negative real parts, [19]. If one or more eigenvalues have a positive real part, the steady state is unstable. If one or more eigenvalues have a zero real part while all the other eigenvalues have a negative real part, the steady state is at the stability limit. The configuration and number of the eigenvalues with zero real part determine the type of bifurcation emerging from this steady state.

### 3.3 Bifurcation analysis and continuation algorithm

Bifurcation analysis refers to the study of changes in the structure or stability of the solutions of a system as parameters are varied, [19–22]. With the help of a path continuation algorithm, solution paths are found by varying a distinguished parameter. To conduct a bifurcation analysis, the system to be investigated is described by the dynamics equation

$$\dot{\mathbf{x}}(t) = \mathbf{f}(\mathbf{x}, \mathbf{p}) \quad (13)$$

where  $\mathbf{x}$  represents the state vector of the vehicle model and  $\mathbf{p}$  is the vector of parameters. In this study the parameter vector consists of  $\mathbf{p} = [\delta, T_{\text{tot}}, \gamma, a_t]^T$ . The parameter vector is split into a distinguished parameter  $\lambda$ , e.g. the drive torque distribution  $\gamma$ , and free and fixed parameters  $\mathbf{p}_{\text{free}}$  and  $\mathbf{p}_{\text{fixed}}$ , respectively.

It is intended to investigate different (quasi-steady-state) driving conditions for the same vehicle velocity for a varied distinguished parameter. Hence, the vehicle velocity is fixed, here to a selected value of  $v = v_0 = 20$  m/s. Therefore constraint equations are required,

and the augmented set of equations reads as follows:

$$\dot{\mathbf{x}}(t) = \mathbf{f}(\mathbf{x}, \mathbf{p}), \quad \mathbf{g}(\mathbf{x}, \mathbf{p}) = \mathbf{0}. \tag{14}$$

where

$$\mathbf{g}(\mathbf{x}, \mathbf{p}) = \begin{bmatrix} v - v_0 \\ \mathbf{p}_l - \mathbf{p}_{\text{fixed}} \end{bmatrix} \tag{15}$$

with the indices  $l$  of the fixed parameters. If, in addition to the velocity  $v$ , further states shall be fixed, a respective number of fixed parameters from  $\mathbf{p}_{\text{fixed}}$  must instead be incorporated into  $\mathbf{p}_{\text{free}}$ .

For path continuation, the algorithm tracks the solution path by ‘tangential continuation’, utilizing the current and prior found solution to make an initial guess for the next solution step, [20]. To track solution paths of bifurcation points, additional constraint equations related to the respective type of bifurcation (e.g. Hopf, Fold and Takens–Bogdanov bifurcation), [19–22], have to be considered, where, depending on the codimension of the corresponding bifurcation, [19], the respective number of fixed parameters have to be set free.

## 4 Results

### 4.1 Steady-state handling characteristics

Vehicle and tyre parameters have been selected to map a vehicle with understeering characteristics, [18], at zero tangential acceleration  $\dot{v} = a_t = 0 \text{ m/s}^2$ , see also Sect. 2. The handling diagram for  $\gamma = 0$  (FWD configuration) and  $\gamma = 1$  (RWD configuration) is depicted in the top graph of Fig. 3, where the steering angle  $\delta$  is plotted over the steady-state normal acceleration  $a_n = v \dot{\psi}$  at a constant vehicle velocity of  $v = 20 \text{ m/s}$ . Moreover, at high normal acceleration, both configurations show final understeer characteristics, [23]. Consequently, various AWD configurations (i.e.  $0 < \gamma < 1$ ) will show similar (final) understeer characteristics. Due to zero tangential acceleration  $a_t$  and small vehicle sideslip angles  $\beta$ , the longitudinal load transfer is almost zero.

Since the traction forces at the front wheels generate additional yaw torque in the FWD configuration due to the steered front wheels, a slightly higher maximum normal acceleration may be observed compared to RWD configuration, see also [8]. This effect decreases

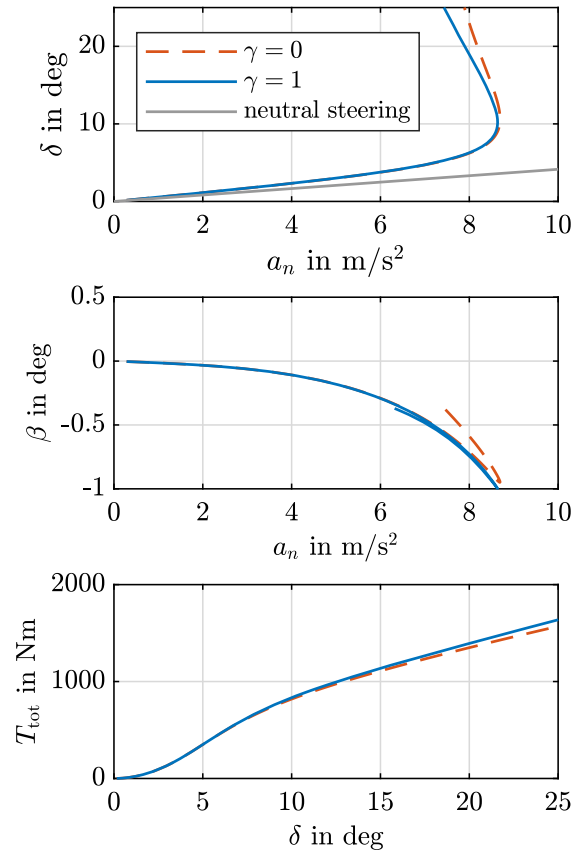


**Fig. 3** Handling diagram of the front and rear-drive vehicle at zero tangential acceleration  $a_t = 0 \text{ m/s}^2$  and constant velocity  $v = 20 \text{ m/s}$ , compared to neutral steering behaviour

with increasing vehicle velocities since the steering angle at the maximal normal acceleration decreases.

In the middle graph of Fig. 3, the evolution of the vehicle sideslip angle  $\beta$  is depicted. It may be noticed that at the FWD configuration, the absolute value of the vehicle sideslip angle  $\beta$  decreases after reaching the maximum normal acceleration. In contrast, at the RWD configuration, the sideslip angles  $\beta$  remain similar. This effect can also be attributed to the longitudinal forces at the front axle. The steady-state total drive torque  $T_{\text{tot}}$  is plotted over the steering angle  $\delta$  at the bottom graph in Fig. 3. After reaching the maximum normal acceleration  $a_n$  at  $\delta \approx 10$  deg, slightly higher total drive torques  $T_{\text{tot}}$  result at the RWD configuration compared to the FWD configuration.

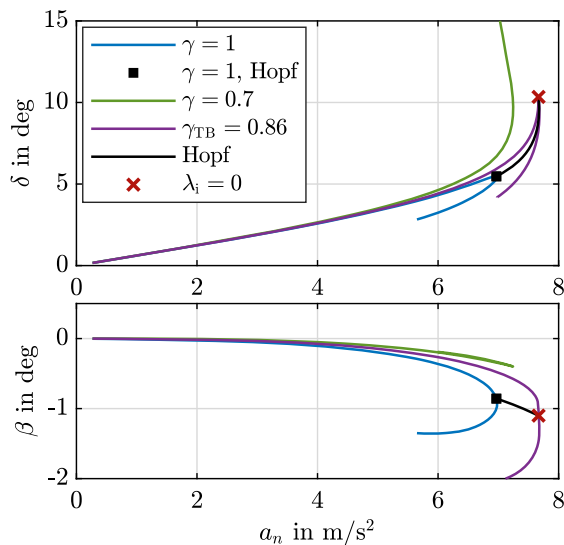


**Fig. 4** Steering angle  $\delta$  and vehicle sideslip angle  $\beta$  for different drive torque distributions  $\gamma$  plotted over the normal acceleration  $a_n$ . Quasi-steady-state solutions for tangential acceleration  $a_t = 4 \text{ m/s}^2$  and constant velocity  $v = 20 \text{ m/s}$

#### 4.2 Handling behaviour under longitudinal acceleration

Increasing the vehicle tangential acceleration  $a_t$  results in a qualitative change in the handling characteristics of the vehicle with the RWD configuration,  $\gamma = 1$ , compared to the zero tangential acceleration case. The handling diagram in Fig. 4 is derived for a constant tangential acceleration  $a_t = 4 \text{ m/s}^2$ , which corresponds to a medium tangential acceleration on a high friction road surface. The handling characteristics change to final oversteer behaviour at a certain normal acceleration, Fig. 4, blue line. In contrast, for an AWD configuration with a considerable portion of the total drive torque  $T_{\text{tot}}$  at the front axle, e.g.  $\gamma = 0.7$ , the final understeer characteristics are maintained, green line.

At evaluating the eigenvalues of the  $\gamma = 1$  branch at  $a_t = 4 \text{ m/s}^2$ , a Hopf-type loss of stability is identified close to the maximum normal acceleration  $a_n \approx 7 \text{ m/s}^2$ , marked with a black square in Fig. 4. Similar findings are presented in [24–26] for vehicles with oversteering characteristics in steady-state conditions. The Hopf bifurcation indicates an oscillatory loss of stability, in this case with very low frequency up to approximately 0.05 Hz. The critical mode shape of the Hopf bifurcation is described in [24] for a three degrees of freedom two-wheel vehicle model. It was shown that

the velocity  $v$  and yaw rate  $\dot{\psi}$  represent the dominant entries of the eigenvector. With the extended vehicle model applied in this study, additionally, the angular speed of the rear inner wheel  $\omega_3$  significantly contributes to the eigenvector of the critical mode.

To derive the Hopf branch in the handling diagram depicted in Fig. 4, the drive torque distribution  $\gamma$  is selected to be the distinguished parameter. The solution of the Hopf branch is calculated for constant tangential acceleration  $a_t = 4 \text{ m/s}^2$ . With decreasing drive torque distribution  $\gamma$ , the Hopf point, starting at the black square in Fig. 4 with  $\gamma = 1$ , moves to higher normal accelerations  $a_n$ , black line, until the imaginary part of the Hopf eigenvalue  $\lambda_i$  approaches zero, indicated by the red  $\times$ . The period of the limit cycle related to the Hopf bifurcation increases towards infinity, and the loss of stability transitions from oscillatory to non-oscillatory. For the considered vehicle model and parameters, and for a tangential acceleration of  $a_t = 4 \text{ m/s}^2$ , this condition is reached at  $\gamma = \gamma_{\text{TB}} = 0.86$ .

For  $\lambda_i = 0$  a new type of bifurcation occurs, characterised by a double zero eigenvalue, known as the Takens–Bogdanov bifurcation. This type of bifurcation was reported in [11] for a pure lateral two degrees of freedom two-wheel vehicle model, and it is characterised by reaching the maximum lateral axle force of the front axle and the rear axle simultaneously. As a result, a small change in the vehicle state will not result in a change in the lateral axle forces both at the front axle and the rear axle. In the detailed vehicle model used in this study, the Takens–Bogdanov point has the property that either the lateral force or the longitudinal force of the front axle and the rear axle reach their maximum simultaneously. This will be discussed in more detail in Sect. 4.4.

A further decrease of the drive torque distribution  $\gamma$  ( $< \gamma_{\text{TB}}$ ) results in a final understeer handling characteristics of the vehicle. Therefore the Takens–Bogdanov point defines the change from final oversteer to final understeer behaviour.

For a given tangential acceleration, e.g.  $a_t = 4 \text{ m/s}^2$  in Fig. 4, there exists only one quasi-steady-state solution with a double zero eigenvalue, i.e. the Takens–Bogdanov point.

4.3 GG envelope

From the handling diagram Fig. 4, it becomes obvious that the Takens–Bogdanov point, red  $\times$ , represents a quasi-steady-state driving condition very close to the maximum attainable normal acceleration  $a_n$  of the vehicle for a given tangential acceleration  $a_t$ . Moreover, it defines the maximum normal acceleration  $a_n$  of stable steady-state driving conditions in the vehicle handling characteristics for the drive torque distribution  $\gamma_{TB}$ , due to the double zero eigenvalue, purple line in Fig. 4.

Hence, by varying the tangential acceleration  $a_t$ , the corresponding normal acceleration  $a_n$  at the Takens–Bogdanov points defines a GG envelope of the vehicle close to the maximum attainable GG envelope found with optimisation technique [27]. However, the GG envelope defined by the Takens–Bogdanov branch represents the maximum GG envelope of stable steady-state driving conditions.

In Fig. 5, the GG envelope is plotted w.r.t. the longitudinal and lateral acceleration of the vehicle,  $a_x$  and  $a_y$ , respectively, as is typical for a GG diagram, [28]. Since this diagram is symmetrical w.r.t. the abscissa, it is plotted and discussed for  $a_y \geq 0 \text{ m/s}^2$  only in the following. At longitudinal accelerations  $a_x \approx 3 \text{ m/s}^2$  to  $12 \text{ m/s}^2$  and decelerations  $a_x \approx -2 \text{ m/s}^2$  to  $-12 \text{ m/s}^2$ , Takens–Bogdanov branches exist and are plotted in red colour. Between  $a_x \approx -2 \text{ m/s}^2$  and  $a_x \approx 3 \text{ m/s}^2$ , the vehicle exhibits final understeer behaviour for several drive torque distributions  $\gamma$ , where the maximum attainable normal accelerations  $a_y$  for  $\gamma = 1$  is depicted in Fig. 5, blue colour. Obviously, the maximum attainable lateral accelerations  $a_y$  increase with decreasing  $a_x$  between the onsets of the Takens–Bogdanov branches. This property of the GG envelope may be attributed to the longitudinal load transfer between the axles, which increases the vertical load at the front (‘weaker’) axle for decreasing  $a_x$ , and consequently enhances transferable tyre forces.

At  $a_x \approx 3 \text{ m/s}^2$ , besides the Takens–Bogdanov branch, also a Hopf bifurcation emerges, both for a drive torque distribution of  $\gamma = 1$ , see  $p_1$  indicated by the blue  $\times$  in Fig. 5, and similar at  $a_x \approx -2 \text{ m/s}^2$ . Beyond longitudinal accelerations  $a_x \approx 3 \text{ m/s}^2$ , the Hopf branch for  $\gamma = 1$  (grey solid line in Fig. 5) limits the ‘stable’ area of combined accelerations for the RWD configuration, similarly for negative  $a_x$ . The Hopf bifurcation exists for final oversteer vehicle con-

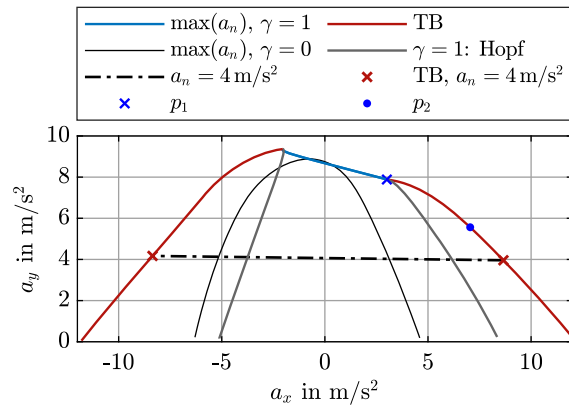
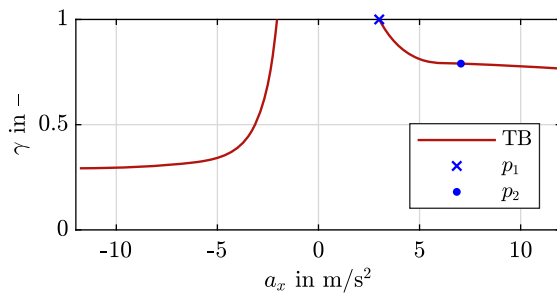


Fig. 5 Takens–Bogdanov and Hopf branches in the GG diagram

figurations, which is equivalent to a drive torque distribution between  $\gamma = 1$  and the drive torque distribution  $\gamma_{TB}$  of the Takens–Bogdanov point, for a given longitudinal acceleration  $a_x$ .

The black line in Fig. 5 shows the maximum attainable combined lateral and longitudinal accelerations for drive and brake forces applied at the front axle only ( $\gamma = 0$ ). It can be observed that in the acceleration case,  $a_x > 0$ , the configuration with  $\gamma = 1$  is superior compared to  $\gamma = 0$  considering the GG envelope, with the opposite in the deceleration case. However, the (stable) GG envelope for both  $\gamma = 1$  and  $\gamma = 0$  is considerably smaller compared to the Takens–Bogdanov configuration  $\gamma = \gamma_{TB}$ .

The drive torque distribution  $\gamma_{TB}$  along both Takens–Bogdanov branches is plotted in Fig. 6 over the longitudinal acceleration  $a_x$ . For longitudinal accelerations  $a_x > 0$ , starting at  $a_x \approx 3 \text{ m/s}^2$  and  $\gamma_{TB} = 1$ , the drive torque distribution  $\gamma_{TB}$  decreases initially rather strongly. For higher levels of longitudinal acceleration ( $a_x \gtrsim 6 \text{ m/s}^2$ ), the drive torque distribution  $\gamma_{TB}$  remains almost constant. This qualitative change arises from the fact that the appearance of the Takens–Bogdanov bifurcation may have various causes that will be investigated in Sect. 4.4 by inspecting the corresponding tyre forces. In the deceleration case ( $a_x < 0$ ), the evolution of the drive torque distribution  $\gamma_{TB}$  over  $a_x$  exhibits qualitatively similar behaviour. However, at high levels of deceleration, the value of  $\gamma_{TB}$  is considerably lower, at  $\approx 0.3$ . This value is typical for the brake force distribution that ensures optimal braking performance, see [29].



**Fig. 6** Drive torque distribution  $\gamma_{TB}$  of the Takens–Bogdanov branch plotted over longitudinal acceleration  $a_x$

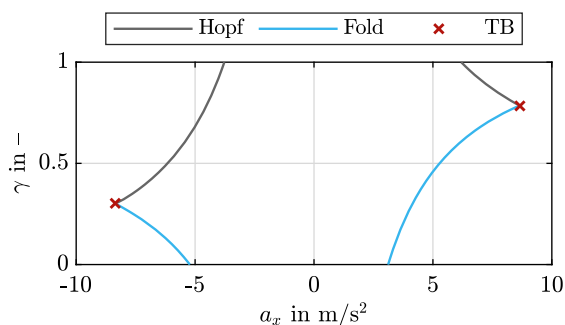


**Fig. 7** Hopf and Fold bifurcation in the  $\gamma$ - $a_x$ -plane for a normal acceleration of  $a_n = 4 \text{ m/s}^2$  corresponding to the dash-dotted line in Fig. 5

For drive torque distributions  $\gamma < \gamma_{TB}$ , e.g. FWD vehicles, and a certain level of longitudinal acceleration  $|a_x|$ , another type of loss of stability is found: a Fold bifurcation. The Fold bifurcation is, similar to the Hopf bifurcation, a codimension one bifurcation. It is characterised by a single zero eigenvalue.

To illustrate how the stability boundaries, defined by the Hopf, Takens–Bogdanov, and Fold bifurcations, evolve depending on the drive torque distribution  $\gamma$  for a specific level of normal acceleration  $a_n$  ( $\approx a_y$ ), a corresponding contour plot is indicated as a black dash-dotted line in the GG diagram Fig. 5 and plotted in Fig. 7.

For the  $\gamma = 0$  configuration and  $a_n = 4 \text{ m/s}^2 = \text{const}$ , at  $a_x \approx 3 \text{ m/s}^2$  and  $a_x \approx -5 \text{ m/s}^2$ , Fold bifurcations occur, characterised by a non-oscillatory loss of stability. The corresponding critical eigenvector indicates a spin-up of the front inner wheel, where the global motion of the vehicle in the road plane is only marginally affected. By increasing the drive torque distribution  $\gamma$ , the Fold bifurcation branches reach the Takens–Bogdanov points, red  $\times$  in Fig. 7. A second

eigenvalue (besides the zero eigenvalue of the Fold bifurcation) converges to zero approaching the Takens–Bogdanov points. Increasing the drive torque distribution  $\gamma$  further ( $\gamma > \gamma_{TB}$ ), the Hopf bifurcation branches define the stability boundary, where the double zero eigenvalues change to conjugate complex eigenvalue pairs, and the configuration results in a final oversteer vehicle behaviour.

Obviously, for a desired constant lateral acceleration  $a_y$ , the drive torque distribution  $\gamma_{TB}$  allows for maximum longitudinal acceleration  $a_x$  within the stable GG envelope.

The most relevant parameter defining the GG envelope is the friction potential since the stability boundaries strongly depend on the saturation of the tyre forces. A different friction potential basically scales the GG diagram. At low friction surfaces, due to lower levels of acceleration and consequently vertical load transfer, lower drive torque distributions result for the Takens–Bogdanov branch for positive longitudinal acceleration. The branch is shifted, but the qualitative behaviour does not change.

Besides the Takens–Bogdanov bifurcation, characteristic properties of the Fold bifurcation are investigated in more detail in the next sections, focusing on practical implications.

#### 4.4 Interpretation from a vehicle dynamics perspective

To allow for an interpretation of the Takens–Bogdanov branch from a vehicle dynamics perspective, the operating conditions of the tyres are inspected at two representative vehicle states in the following.

In Figs. 8 and 9, the longitudinal and lateral tyre forces are shown for two characteristic Takens–Bogdanov points,  $p_1$  and  $p_2$  (see Figs. 5 and 6). In the left graphs, the normalized longitudinal tyre forces  $F_{xi}/F_{zi,0}$ ,  $i \in \{1, 2, 3, 4\}$  are plotted against the longitudinal slips  $s_{xi}$  for the constant sideslip angles  $\alpha_i$  corresponding to  $p_1$  and  $p_2$ , respectively. In the right graphs, the normalized lateral tyre forces  $F_{yi}/F_{zi,0}$  plotted against the sideslip angles  $\alpha_i$  are depicted for respective longitudinal slips  $s_{xi}$ . The tyre forces at the investigated Takens–Bogdanov points are indicated by  $\circ$ .

Since  $\gamma = \gamma_{TB} = 1$  at  $p_1$ , the normalized longitudinal tyre forces  $F_{xi}/F_{zi,0}$  at the front axle are zero in

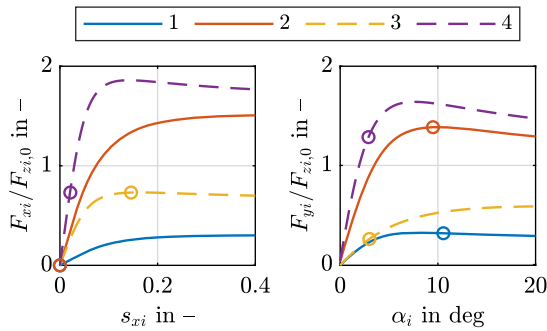


**Fig. 8** Tyre characteristics corresponding to  $p_1$  ( $\gamma = 1, a_t \approx 2.8 \text{ m/s}^2$ )

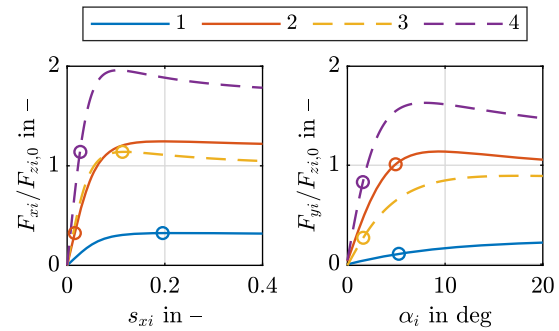


**Fig. 9** Tyre characteristics corresponding to  $p_2$  ( $\gamma = 0.79, a_t = 7 \text{ m/s}^2$ )

Fig. 8 (left graph). The double zero eigenvalue at this Takens–Bogdanov point can be attributed to the vanishing effective (local) cornering stiffness of the front axle, caused by the saturation of the effective lateral axle force,  $i \in \{1, 2\}$  (right graph) and the saturation of the longitudinal force of the inner wheel at the rear axle  $i = 3$  (left graph), similar to findings presented in [11]. Consequently, due to the differential gear at the rear axle, a small variation of the slips of the tyres  $i \in \{1, 2, 3\}$  does not result in a change of the respective axle forces. The post-critical behaviour of the vehicle after loss of stability is characterised by a wheel spin-up of the inner wheel at the rear axle ( $i = 3$ ).

A different observation can be made by inspecting the tyre forces at the Takens–Bogdanov point  $p_2$ , where rather small gradients of  $\gamma$  w.r.t. the longitudinal acceleration  $a_x$  may be noted in Fig. 6. Compared to  $p_1$ , due to the increased portion of the total drive torque  $T_{\text{tot}}$  at the front axle (i.e.  $\gamma < 1$ ), the inspection of the tyre forces shows that both the inner wheel at the front axle  $i = 1$  and the inner wheel at the rear axle  $i = 3$  reach their longitudinal force saturation simultaneously, Fig. 9 (left graph). Similar to the above, a small variation of the longitudinal slips of the tyres  $i \in \{1, 3\}$  does not result in a change of the respective axle forces, due to the differential gears, resulting in a double zero eigenvalue. In the case of loss of stability, the inner wheels at both the front and rear axle may spin up.

An increase of the drive torque distribution  $\gamma > \gamma(p_2)$  leads to a final oversteer behaviour of the vehicle and a Hopf bifurcation, see Fig. 7, since the tyre forces at the rear axle,  $i \in \{3, 4\}$ , are saturated first. Contrary, a reduction of the drive torque distribution  $\gamma < \gamma(p_2)$  will result in a saturation of the longitudinal tyre force of the front inner wheel,  $i = 1$ , which is char-

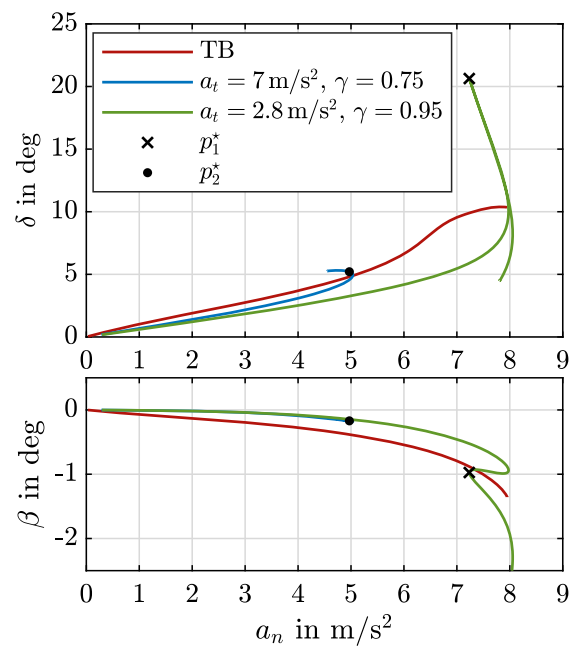


**Fig. 10** Handling characteristics for different constant tangential accelerations  $a_t$  and drive torque distributions  $\gamma$ , with Takens–Bogdanov branch and Fold points

acterised by a single zero eigenvalue, the Fold bifurcation. This behaviour seems reasonable when inspecting the tyre forces at the Takens–Bogdanov point  $p_2$ . A corresponding handling diagram for the latter case is exemplarily shown in Fig. 10 for  $a_t = 7 \text{ m/s}^2$  and  $\gamma = 0.75 < \gamma(p_2)$  (blue line), where a Fold bifurcation occurs directly after reaching the maximum normal acceleration. The location of the corresponding Fold point is denoted  $p_2^*$  and marked by a black dot. Loss of stability is characterised by the spin-up of the front inner wheel,  $i = 1$ .

In contrast, at the Takens–Bogdanov point  $p_1$ , longitudinal forces at the front axle,  $i \in \{1, 2\}$ , are zero, see Fig. 8, since  $\gamma = 1$ . Consequently, the loss of stability at the corresponding Fold bifurcation for  $\gamma < \gamma(p_1)$  and  $a_t = a_t(p_1) = 2.8 \text{ m/s}^2$  will not be characterised by a spin-up of the front inner wheel  $i = 1$ . The handling diagram for  $a_t = a_t(p_1)$  and  $\gamma = 0.95 < \gamma(p_1)$  shows ‘final understeer’ characteristics, Fig. 10 (green line). At the maximum steering angle  $\delta \approx 21 \text{ deg}$ , a Fold bifurcation occurs, where the loss of stability is characterised by the spin-up of the inner wheel at the rear axle  $i = 3$ , similar to  $p_1$ . The corresponding Fold point is denoted  $p_1^*$  and marked by a black  $\times$ . The following (unstable) quasi-steady vehicle states show final oversteer characteristics. This behaviour is caused from the increased curvature resistance due to the increasing steering angle  $\delta$  and consequent increase of the necessary total drive torque  $T_{\text{tot}}$ , causing the saturation of the longitudinal force at the rear axle. A further reduction of the drive torque distribution, e.g. to  $\gamma = 0.9$ , shifts the corresponding Fold bifurcation to even higher steering angles  $\delta > 35 \text{ deg}$ , where the qualitative handling characteristics remain similar to the  $\gamma = 0.95$  configuration (green line in Fig. 10). However, due to the large steering angles  $\delta$ , this case is of less relevance from a practical perspective.

The steering angles  $\delta$  and vehicle sideslip angles  $\beta$  corresponding to the Takens–Bogdanov branch are depicted in Fig. 10 in red colour.

Consequently, compared to the post-critical behaviour of the vehicle after the loss of stability caused by the Hopf bifurcation, see [25], the loss of stability caused by the Takens–Bogdanov and Fold bifurcation, were  $\gamma \leq \gamma_{\text{TB}}$ , is less severe from a vehicle dynamics perspective.

#### 4.5 Fold bifurcation in the GG– $\gamma$ diagram

To interpret the above Fold points  $p_1^*$  and  $p_2^*$  in the context of the GG diagram Fig. 5, the occurrence of Fold bifurcations is illustrated in a three-dimensional figure for positive longitudinal accelerations  $a_x$ , the GG– $\gamma$  diagram, Fig. 11. In addition, the contour plot at  $a_n = 4 \text{ m/s}^2$ , Fig. 7, is represented by the light grey shaded plane. For completeness, the Takens–Bogdanov branch and points  $p_1$  and  $p_2$  (blue  $\times$  and dot), the Hopf branch for  $\gamma = 1$  (grey line), and the maximum attain-

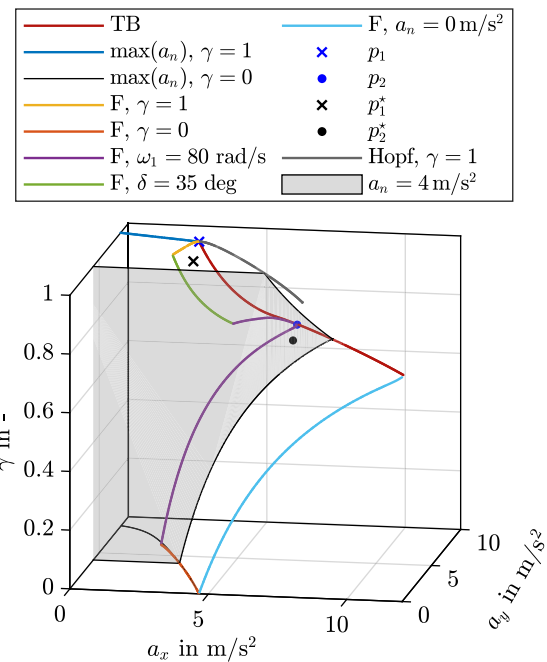


**Fig. 11** Fold bifurcations in the GG– $\gamma$  diagram ( $a_x > 0 \text{ m/s}^2$ )

able normal acceleration for  $\gamma = 1$  and  $\gamma = 0$  (blue and black line), corresponding to Fig. 5, are depicted.

As described above, for a constant tangential acceleration  $a_t$ , at reducing the drive torque distribution  $\gamma < \gamma_{\text{TB}}$  and starting from the corresponding Takens–Bogdanov point, a Fold point is found, i.e.  $p_1 \rightarrow p_1^*$  and  $p_2 \rightarrow p_2^*$ . Since in Sect. 4.4 two qualitatively different types of Fold points are identified from a vehicle dynamics perspective,  $p_1^*$  and  $p_2^*$ , an illustration of the areas, where these two different types of Fold points appear in the GG– $\gamma$ -diagram, is attempted.

To represent the Fold surface related to the Fold point  $p_2^*$  (black dot), where the loss of stability is characterised by the spin-up of the front inner wheel  $i = 1$ , four bounds are considered. One bound is defined by the Takens–Bogdanov branch (red line). The second bound is defined by the Fold branch for  $a_n = 0 \text{ m/s}^2$  (light blue line) that consequently is located at the  $\gamma - a_x$ -plane of Fig. 11. The third bound is represented by the Fold branch found for  $\gamma = 0$  (orange line), i.e. a FWD vehicle, that is located at the  $a_x - a_y$ -plane. As this branch is continued toward higher lateral accelerations, Fold points are found that are characterised by extremely high longitudinal slips ( $s_{x1} \gg 1$ ) at the front inner tyre,  $i = 1$ , while the lateral acceleration  $a_y$

ceases to increase further. To determine the Fold surface for practical useful states, the fourth Fold branch is calculated for a constant wheel speed of the front inner wheel of  $\omega_1 = 80$  rad/s (purple line), where the longitudinal slip  $s_{x1}$  is limited to  $\approx 0.25$ . Several Fold points located at this surface show similar behaviour w.r.t. the loss of stability.

The second Fold surface depicted in Fig. 5 is related to the Fold point  $p_1^*$  (black  $\times$ ), where the loss of stability is characterised by the spin-up of the rear inner wheel  $i = 3$  (at rather large steering angles  $\delta$ ). Besides the Takens–Bogdanov branch (red line), this surface again is bounded by the Fold branch calculated for a constant wheel speed of the front inner wheel of  $\omega_1 = 80$  rad/s (purple line). Starting again at the Takens–Bogdanov branch, following the third Fold branch for  $\gamma = 1$  (orange line), i.e. a RWD vehicle, leads to an increase of the steering angle  $\delta$  beyond practical meaningful steering angles  $\delta > 35$  deg, with a handling characteristics similar as depicted in Fig. 10 for the Fold point  $p_1^*$ . Consequently, the fourth Fold branch is found considering a constant steering angle  $\delta = 35$  deg (green line), taking kinematic limitations of the steering system into account.

Finally, the practical relevance of the two characteristic Fold surfaces related to  $p_1^*$  and  $p_2^*$  is investigated from a vehicle dynamics perspective. Considering the Fold surface related to  $p_2^*$ , the maximum attainable normal acceleration  $a_n$  for  $\gamma = 0$  in Fig. 11 (black line in the  $a_x - a_y$ -plane) is compared to the Fold branch for  $\gamma = 0$ , i.e. an FWD vehicle (orange line). The Fold branch is located close to the line characterising the maximum attainable normal acceleration. This is also obvious from inspecting the Fold point  $p_2^*$  (black dot) for  $\gamma = 0.75$  in the handling diagram Fig. 10, where the maximum attainable normal acceleration  $a_n$  at a given tangential acceleration  $a_t$  is located next to  $p_2^*$ . Consequently, conditions, where the loss of stability is characterised by the wheel spin-up of the front inner wheel  $i = 1$ , are very likely to appear in practical driving scenarios, considering parameter and state disturbances. In contrast, regarding the Fold surface related to  $p_1^*$ , several respective handling diagrams are qualitatively similar to the diagram depicted in Fig. 10,  $a_t = a_t(p_1) = 2.8$  m/s<sup>2</sup>,  $\gamma = 0.95$  (green line). Obviously, the Fold point (black  $\times$ ) emerges at a considerably larger steering angle  $\delta$  and lower level of normal acceleration  $a_n$  compared to the maximum attainable normal acceleration in the vicinity of the Takens–

Bogdanov branch (red line). Consequently, the second Fold surface is considered to be of less practical relevance.

## 5 Conclusions

In this paper, the impact of the drive torque distribution between the front axle and rear axle of an AWD vehicle on its combined lateral and longitudinal handling envelope and on respective stability properties has been investigated. For that purpose, bifurcation and continuation methods have been applied to a four-wheel vehicle model. Some of the main conclusions of the present research are:

- Regarding the critical mode shapes, a rather detailed vehicle and tyre model has to be considered in a simulation study on the stability properties of a vehicle at the limits of handling in regular driving to map both the ‘global’ vehicle motion and the dynamics of the individual wheels.
- Takens–Bogdanov bifurcations appear at the limits of handling and characterise the change from final oversteer to final understeer.
- Besides the Takens–Bogdanov bifurcations, corresponding Hopf bifurcations, [25], and Fold bifurcations are found. The drive torque distributions at the Takens–Bogdanov branch determine the transition from Hopf to Fold bifurcations.
- The Takens–Bogdanov branch also defines the drive torque distribution for reaching the maximum possible combined longitudinal and lateral acceleration envelope within the (open loop) stable steady-state handling regime, which is quite similar to the optimal, partially unstable envelope shown in [27].
- Two distinct Fold surfaces are identified that are related to the tyre operating conditions at the corresponding Takens–Bogdanov bifurcations. These Fold surfaces exhibit different, characteristic types of loss of stability, where one of these surfaces is considered to be of practical relevance.
- The drive torque distributions at the Takens–Bogdanov branch provide a good indication for a design criterium for safe and performant drive torque distribution controllers of AWD vehicles.

The approach presented in this paper to investigate the stability and handling properties of AWD vehicles at combined longitudinal and lateral accelerations will be

applied to different drive architectures (e.g. including a torque vectoring system, limited-slip and locked differential gears) in future research. Moreover, an appropriate drive torque control strategy shall be developed and tested on an experimental vehicle.

**Acknowledgements** The authors thank Alois Steindl for the support and discussion to find and trace the bifurcation branches. The authors acknowledge TU Wien Bibliothek for financial support through its Open Access Funding Program.

**Author contributions** All authors contributed to the study conception and design. The analysis was performed by M.E. All authors read and approved the final manuscript.

**Funding** Open access funding provided by TU Wien (TUW). Open access funding provided by TU Wien (TUW).

**Data availability** No datasets were generated or analysed during the current study.

#### Declarations

**Competing interests** The authors declare no competing interests.

**Open Access** This article is licensed under a Creative Commons Attribution 4.0 International License, which permits use, sharing, adaptation, distribution and reproduction in any medium or format, as long as you give appropriate credit to the original author(s) and the source, provide a link to the Creative Commons licence, and indicate if changes were made. The images or other third party material in this article are included in the article's Creative Commons licence, unless indicated otherwise in a credit line to the material. If material is not included in the article's Creative Commons licence and your intended use is not permitted by statutory regulation or exceeds the permitted use, you will need to obtain permission directly from the copyright holder. To view a copy of this licence, visit <http://creativecommons.org/licenses/by/4.0/>.

#### References

- Pacejka, H.B.: Simplified analysis of steady-state turning behaviour of motor vehicles. Part 1. Handling diagrams of simple systems. *Veh. Syst. Dyn.* **2**(3), 161–172 (1973). <https://doi.org/10.1080/00423117308968439>
- Pacejka, H.B.: Simplified analysis of steady-state turning behaviour of motor vehicles part 2: stability of the steady-state turn. *Veh. Syst. Dyn.* **2**(4), 173–183 (1973). <https://doi.org/10.1080/00423117308968440>
- Pacejka, H.B.: Simplified analysis of steady-state turning behaviour of motor vehicles part 3: more elaborate systems. *Veh. Syst. Dyn.* **2**(4), 185–204 (1973). <https://doi.org/10.1080/00423117308968441>
- Klomp, M., Thomson, R.: Influence of front/rear drive force distribution on the lateral grip and understeer of all-wheel drive vehicles. *Int. J. Veh. Des.* **56**(1–4), 34–48 (2011). <https://doi.org/10.1504/IJVD.2011.043272>
- Horiuchi, S., Okada, K., Nohtomi, S.: Analysis of accelerating and braking stability using constrained bifurcation and continuation methods. *Veh. Syst. Dyn.* **46**, 585–597 (2008). <https://doi.org/10.1080/00423110802007779>
- Abe, M.: A theoretical analysis on vehicle cornering behaviors in acceleration and in braking. *Veh. Syst. Dyn.* **15**(sup1), 1–14 (1986). <https://doi.org/10.1080/00423118608969122>
- Bucchi, F., Frendo, F.: A new formulation of the understeer coefficient to relate yaw torque and vehicle handling. *Veh. Syst. Dyn.* **54**(6), 831–847 (2016). <https://doi.org/10.1080/00423114.2016.1167225>
- Basilio Lenzo, A.S., Bucchi, F., Frendo, F.: On the handling performance of a vehicle with different front-to-rear wheel torque distributions. *Veh. Syst. Dyn.* **57**(11), 1685–1704 (2019). <https://doi.org/10.1080/00423114.2018.1546013>
- Ono, E., Hosoe, S., Tuan, H.D., Doi, S.: Bifurcation in vehicle dynamics and robust front wheel steering control. *IEEE Trans. Control Syst. Technol.* **6**(3), 412–420 (1998). <https://doi.org/10.1109/87.668041>
- Shuiwen Shen, P.S., Wang, J., Premier, G.: Nonlinear dynamics and stability analysis of vehicle plane motions. *Veh. Syst. Dyn.* **45**(1), 15–35 (2007). <https://doi.org/10.1080/00423110600828285>
- Della Rossa, F., Mastinu, G., Piccardi, C.: Bifurcation analysis of an automobile model negotiating a curve. *Veh. Syst. Dyn.* **50**(10), 1539–1562 (2012). <https://doi.org/10.1080/00423114.2012.679621>
- Pauwelussen, J.: Axle characteristics and vehicle limit cycle behaviour. *Veh. Syst. Dyn.* **0**(0), 1–19 (2024). <https://doi.org/10.1080/00423114.2024.2322487>
- Farroni, F., Russo, M., Russo, R., Terzo, M., Timpone, F.: A combined use of phase plane and handling diagram method to study the influence of tyre and vehicle characteristics on stability. *Veh. Syst. Dyn.* **51**(8), 1265–1285 (2013). <https://doi.org/10.1080/00423114.2013.797590>
- Wang, X., Li, W., Zhang, F., Li, Z., Bao, W.: Research on the vehicle steering and braking stability region. *Appl. Sci.* (2023). <https://doi.org/10.3390/app13137806>
- Zhang, L., Ding, H., Guo, K., Zhang, J., Pan, W., Jiang, Z.: Cooperative chassis control system of electric vehicles for agility and stability improvements. *IET Intel. Transp. Syst.* **13**(1), 134–140 (2019). <https://doi.org/10.1049/iet-its.2018.5079>
- Tremlett, A.J., Assadian, F., Purdy, D.J., Vaughan, N., A.P., M., Halley, M.: Quasi-steady-state linearisation of the racing vehicle acceleration envelope: a limited slip differential example. *Veh. Syst. Dyn.* **52**(11), 1416–1442 (2014). <https://doi.org/10.1080/00423114.2014.943927>
- De Novellis, L., Sorniotti, A., Gruber, P.: Optimal wheel torque distribution for a four-wheel-drive fully electric vehicle. *SAE Int. J. Passenger Cars Mech. Syst.* **6**(1), 128–136 (2013). <https://doi.org/10.4271/2013-01-0673>
- Pacejka, H.: *Tire and Vehicle Dynamics*. Elsevier (2005)
- Kuznetsov, Y.A.: *Elements of Applied Bifurcation Theory*. Springer (1998)
- Seydel, R.: *Practical Bifurcation and Stability Analysis*. Springer (2009)

21. Guckenheimer, J., Holmes, P.: *Nonlinear Oscillations, Dynamical Systems, and Bifurcations of Vector Fields*. Springer (1983)
22. Troger, H., Steindl, A.: *Nonlinear Stability and Bifurcation Theory: An Introduction for Engineers and Applied Scientists*. Springer (2012)
23. Hindiyeh, R.Y., Gerdes, J.C.: Equilibrium Analysis of Drifting Vehicles for Control Design. *Dynamic Systems and Control Conference*, vol. ASME 2009 Dynamic Systems and Control Conference, Volume 1, pp. 181–188 (2009). <https://doi.org/10.1115/DSCC2009-2626>
24. Edelmann, J., Plöchl, M.: Analysis of controllability of automobiles at steady-state cornering considering different drive concepts. In: Spiriyagin, M., Gordon, T., Cole, C., McSweeney, T. (eds.) *Dynamics of Vehicles on Roads and Tracks Vol 1*, pp. 3–8. CRC Press, Rockhampton, Queensland, Australia (2017). <https://doi.org/10.1201/9781351057264>
25. Steindl, A., Edelmann, J., Plöchl, M.: Limit cycles at oversteer vehicle. *Nonlinear Dyn.* **99**(1), 313–321 (2020). <https://doi.org/10.1007/s11071-019-05081-8>
26. Steindl, A., Edelmann, J., Plöchl, M.: Hopf bifurcations for an oversteer vehicle—the influence of wheel load changes. *PAMM* (2021). <https://doi.org/10.1002/pamm.202100179>
27. Eberhart, M., Arndt, M., Edelmann, J., Plöchl, M.: Influence of the front-rear torque distribution on the handling characteristics and stability boundaries of an awd-vehicle. In: Mastinu, G., Braghin, F., Cheli, F., Corno, M., Savaresi, S.M. (eds.) *16th International Symposium on Advanced Vehicle Control*, pp. 200–206. Springer, Cham (2024). [https://doi.org/10.1007/978-3-031-70392-8\\_29](https://doi.org/10.1007/978-3-031-70392-8_29)
28. Milliken, W.F., Milliken, D.L.: *Race car vehicle dynamics*. SAE international Warrendale (1995)
29. Ploechl, M., Lugner, P., Edelmann, J.: Basics of longitudinal and lateral vehicle dynamics. In: Mastinu, G., Ploechl, M. (eds.) *Road and Off-Road Vehicle System Dynamics Handbook*, pp. 971–1021. CRC Press, Boca Raton (2014). <https://doi.org/10.1201/b15560>

**Publisher's Note** Springer Nature remains neutral with regard to jurisdictional claims in published maps and institutional affiliations.

## Paper D

### *Influence of the Front-Rear Torque Distribution on the Handling Characteristics and Stability Boundaries of an AWD-Vehicle*

TU Wien: Manuel Eberhart, Manfred Plöchl, Johannes Edelmann  
CARIAD SE: Martin Arndt

*In: Mastinu, G., Braghin, F., Cheli, F., Corno, M., Savaresi, S.M. (eds) 16th International Symposium on Advanced Vehicle Control. AVEC 2024. Lecture Notes in Mechanical Engineering. Springer, Cham., p. 200–206*

[https://doi.org/10.1007/978-3-031-70392-8\\_24](https://doi.org/10.1007/978-3-031-70392-8_24)

**Keywords:** handling characteristics, stability, bifurcation, drive torque distribution, optimisation, AWD vehicle

**Abstract:** The influence of the drive torque distribution of an AWD vehicle with individual motors at the front and rear axles on the handling and stability properties is investigated. By applying bifurcation analysis methods, different types of loss of stability at combined longitudinal and lateral acceleration are identified. The impact of the drive torque distribution on the stability boundaries in the GG diagram is examined, and the related stable acceleration envelope is compared to the envelope derived from applying optimisation methods. Representative corresponding handling characteristics are compared and discussed.



# Influence of the Front-Rear Torque Distribution on the Handling Characteristics and Stability Boundaries of an AWD-Vehicle

Manuel Eberhart<sup>1</sup>( ), Martin Arndt<sup>2</sup>, Johannes Edelmann<sup>1</sup>,  
and Manfred Plöchl<sup>1</sup>

<sup>1</sup> TU Wien, Institute of Mechanics and Mechatronics, Vienna, Austria  
[manuel.eberhart@tuwien.ac.at](mailto:manuel.eberhart@tuwien.ac.at)

<sup>2</sup> CARIAD SE, Vehicle Motion Energy, Wolfsburg, Germany  
[martin.arndt@cariad.technology](mailto:martin.arndt@cariad.technology)

<https://www.mec.tuwien.ac.at/vsd>, <https://www.cariad.technology>

**Abstract.** The influence of the drive torque distribution of an AWD vehicle with individual motors at the front and rear axles on the handling and stability properties is investigated. By applying bifurcation analysis methods, different types of loss of stability at combined longitudinal and lateral acceleration are identified. The impact of the drive torque distribution on the stability boundaries in the GG diagram is examined, and the related stable acceleration envelope is compared to the envelope derived from applying optimisation methods. Representative corresponding handling characteristics are compared and discussed.

**Keywords:** Handling Characteristics · Stability · Bifurcation · Drive Torque Distribution · Optimisation · AWD Vehicle

## 1 Introduction

Drive train architectures of electric vehicles, often equipped with more than one electric motor, allow both to ‘stabilise’ and to make the vehicle’s motion ‘more responsive’ but also require a profound understanding of its influence on stability and handling to ensure safe operation. Depending on the longitudinal acceleration and drive train configuration, the handling behaviour and respective passive stability properties of the vehicle can significantly change [1,5,6]. To study these characteristic properties, a quasi-steady-state description is derived, where the state of a vehicle accelerated in longitudinal direction is transformed to a mechanically equivalent steady-state [1,6].

Bifurcation analysis is frequently used to find stability boundaries [10]. In [3], Della Rossa et al. analyse the stability properties of a vehicle with different tyre configurations and demonstrate that various types of loss of stability may appear. Horiuchi et al. use a quasi-steady-state description to model transient states to investigate the loss of stability for a longitudinally accelerated vehicle

© The Author(s) 2024  
G. Mastinu et al. (Eds.): AVEC 2024, LNME, pp. 200–206, 2024.  
[https://doi.org/10.1007/978-3-031-70392-8\\_29](https://doi.org/10.1007/978-3-031-70392-8_29)

with fixed drive torque distribution in [5]. Lenzo et al. analyse the handling characteristics for different drive concepts and present the relation between yaw torque and understeer coefficient [7].

This paper investigates the impact of the drive torque distribution of an AWD vehicle with individual motors at the front and rear axles on the transient handling and stability properties. The vehicle state is transformed to a mechanically equivalent quasi-steady-state to apply linear stability theory and to utilise bifurcation and continuation algorithms. For various drive torque distributions, different types of bifurcations are found and discussed. The stable acceleration envelope is compared to the solution found by optimisation, and differences are discussed.

The paper is structured as follows: In the next Section, the vehicle and tyre models are addressed. In Sect. 3, the applied methods are briefly described. In the following Sect. 4, the impact of the longitudinal acceleration on the handling characteristics is shown. The stability boundary found with the bifurcation method is presented in the GG diagram and compared to the optimised acceleration envelope in Sect. 5.

## 2 Vehicle Model

A nonlinear four-wheel vehicle model with 10 degrees of freedom, as introduced and described in [4] and illustrated in Fig. 1, is considered in this study. The rigid vehicle body is modelled with 6 degrees of freedom, (longitudinal velocity  $v_{xB}$ , lateral velocity  $v_{yB}$ , vertical velocity  $v_{zB}$ , roll angle  $\varphi_B$ , pitch angle  $\theta_B$  and yaw rate  $\dot{\psi}_B$ ), and one rotational degree of freedom is considered for each wheel,  $\omega_i$  ( $i = 1, 2, 3, 4$ ). Input quantities are the drive torques at the individual wheels,  $T_1 = T_2$  and  $T_3 = T_4$ , and the steering angle  $\delta$ , where  $\delta_1(\delta)$  and  $\delta_2(\delta)$ . The Magic Formula [9] is used to model the combined tyre force characteristics. In the subsequent figures, the vehicle states are represented in the  $x$ - $y$ - $z$ -coordinate frame depicted in red colour in Fig. 1.

For vehicle parameters, governing equations and tyre force characteristics, please refer to [4].

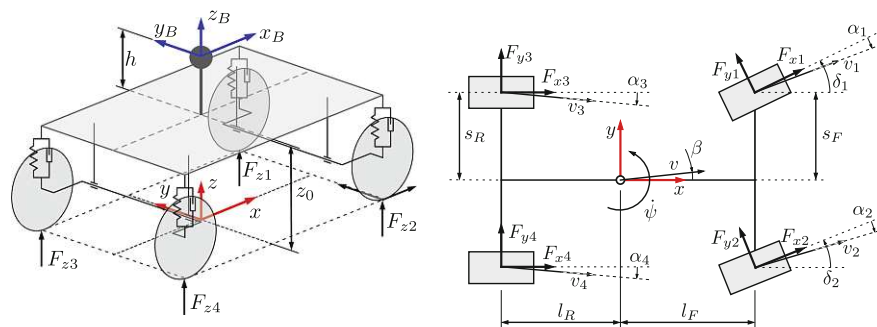


Fig. 1. Schematic illustration of the vehicle model

### 3 Methods

To apply continuation methods for the nonlinear stability analysis, the combined accelerated manoeuvre ( $a_n \neq 0$  and  $a_t \neq 0$ ) is transformed to a quasi-steady-state, mechanically equivalent state, which approximates the combined acceleration manoeuvre well [2, 5]. In this paper, similar to [5], an equivalent force in the direction of the velocity vector is applied at the centre of gravity of the vehicle. This system adaption considers both the load transfer and the mutual influence of the longitudinal and lateral tyre forces. Yaw acceleration  $\dot{\psi}$ , derivative of the vehicle sideslip angle  $\dot{\beta}$ , and the derivatives of the other states are set to zero to fulfil the steady-state condition.

Once equivalent equilibrium solutions are found, linear methods are applied to analyse stability properties. For that purpose, the equations of motion are linearised with respect to the equilibrium solutions,  $\Delta\dot{\mathbf{x}} = \mathbf{A}\Delta\mathbf{x} + \mathbf{B}\Delta\mathbf{u}$ . Lyapunov's first method implies that an equilibrium solution is stable if all eigenvalues  $\lambda_i$  from  $(\mathbf{A} - \lambda_i\mathbf{I})\mathbf{p}_i = \mathbf{0}$ , with the right eigenvector  $\mathbf{p}_i$ , have negative real parts [10].

With the help of a path continuation algorithm [10], solution paths are found by varying parameters and inputs. A more detailed description of the used method is given in [4]. Moreover, optimisation techniques are applied to find the maximum possible acceleration envelope [8]. The result is compared to the stable acceleration envelope found with bifurcation analysis.

### 4 Handling Characteristics at Longitudinal Acceleration

The handling diagram for the considered vehicle with drive torque distribution  $\gamma = 1$ , i.e. rear-wheel-drive (RWD), and zero tangential acceleration shows understeer handling characteristics and limit understeer behaviour, see Fig. 2 (blue line). The respective vehicle configuration with  $\gamma = 0$ , i.e. front-wheel-drive (FWD), shows qualitatively the same characteristics and is not depicted.

Increasing the vehicle tangential acceleration, e.g. to  $a_t = 4 \text{ m/s}^2$ , results in a qualitative change to limit oversteer behaviour of the vehicle with  $\gamma = 1$  (Fig. 2, orange line). In contrast, no qualitative change may be observed for  $\gamma = 0$  (not depicted) and an all-wheel-drive (AWD) configuration with a certain portion of drive torque at the front axle (e.g.  $\gamma = 0.7$ , green line).

Evaluating the eigenvalues for  $\gamma = 1$  at  $a_t = 4 \text{ m/s}^2$  indicates a Hopf-type loss of stability ( $\circ$  in Fig. 2), characterised by a conjugate complex pair of eigenvalues with zero real part. For decreased parameter  $\gamma$  the Hopf point moves to higher normal accelerations  $a_n$  (black line) while the imaginary part of the Hopf eigenvalue  $\lambda_I$  decreases and finally results in two zero eigenvalues, Fig. 2 black  $\times$ , called Takens–Bogdanov bifurcation. Further decrease of the drive torque distribution  $\gamma$  leads to limit understeer behaviour. The torque distribution at the Takens–Bogdanov point,  $\gamma_{\text{TB}} \approx 0.86$  for a tangential acceleration of  $a_t = 4 \text{ m/s}^2$ , characterises the change from limit understeer to limit oversteer behaviour and vice versa. The Takens–Bogdanov solution for various  $\gamma$  and  $a_t$  is depicted in Fig. 2 (red line).

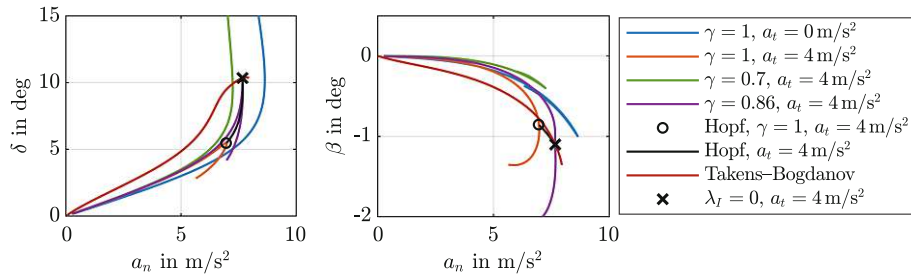


**Fig. 2.** Steering angle  $\delta$  and vehicle sideslip angle  $\beta$  for different drive torque distributions  $\gamma$  at tangential acceleration  $a_t$ . Quasi-steady-state solutions for vehicle velocity  $v = 20 \text{ m/s}$ .

### 5 Takens–Bogdanov Point as Design Criteria

The corresponding  $a_x$ – $a_y$  diagram (GG diagram) depicted in the left graph of Fig. 3 includes two coloured lines: the maximum lateral acceleration for the considered vehicle with  $\gamma = 1$  (blue line) that shows limit understeer behaviour up to a longitudinal acceleration of  $a_x = 2.6 \text{ m/s}^2$ , followed by the Takens–Bogdanov solution for higher longitudinal accelerations (red line). In the right graph of Fig. 3 (red line), the respective torque distribution  $\gamma$  for the Takens–Bogdanov solution is plotted over the longitudinal acceleration  $a_x$ .

In addition, the numerically optimised GG diagram that represents the maximum acceleration envelope for the considered vehicle and the resulting optimisation parameter  $\gamma$  are plotted in Fig. 3 (black lines).

In the left graph, it can be seen that the solutions from bifurcation analysis and optimisation are almost equal. Nevertheless, at small longitudinal accelerations  $a_x < 2.5 \text{ m/s}^2$  the maximum lateral accelerations  $a_y$  from the optimised drive torque distribution  $\gamma$  are slightly superior. Inspecting the respective drive torque distributions  $\gamma$ , right graph in Fig. 3, shows that an AWD configuration is beneficial in this regime.

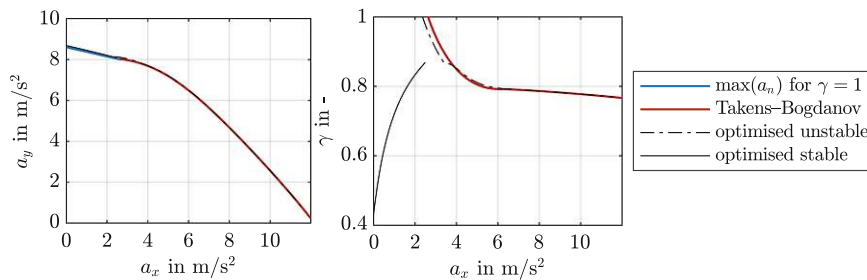


**Fig. 3.** Comparison of Takens–Bogdanov solution and optimised solution: Acceleration envelope  $a_x$ – $a_y$  and drive torque distribution  $\gamma$ .

Considering the graph of the optimal drive torque distribution  $\gamma$ , at  $a_x \approx 2.5$  m/s<sup>2</sup> a discontinuity can be noticed. Evaluating the stability properties of the steady-state solutions derived with the optimisation technique reveals a qualitative change from stable conditions (black solid line) to unstable conditions (black dashed-dotted line) at  $a_x > 2.5$  m/s<sup>2</sup>, whereas the Takens–Bogdanov solution characterises the stability boundary in the  $a_x$ – $a_y$ -envelope. This can also be seen in Fig. 4 where handling curves for three constant tangential accelerations  $a_t = 1, 3, 5$  m/s<sup>2</sup> are plotted for the respective optimal and Takens–Bogdanov quasi-steady-state solutions, and corresponding constant drive torque distributions  $\gamma_{\text{opt}}$  and  $\gamma_{\text{TB}}$ , respectively.

The handling curves for  $a_t = 1$  m/s<sup>2</sup> show that the maximum normal acceleration  $a_n$  of the optimised solution is superior compared to the  $\gamma = 1$  configuration. For  $a_t = 3$  m/s<sup>2</sup> the optimal solution is found for  $\gamma_{\text{opt}} < \gamma_{\text{TB}}$  after loss of stability (Fold bifurcation). The Fold bifurcation occurs after limit understeer behaviour and can be attributed to the saturation of the longitudinal tyre forces at the inner rear wheel ( $i = 3$ ). The behaviour then changes to an unstable oversteer behaviour where the optimal solution is found.

At tangential acceleration  $a_t = 5$  m/s<sup>2</sup> the torque distribution of the optimised solution is a little larger than the torque distribution of the Takens–Bogdanov point ( $\gamma_{\text{opt}} > \gamma_{\text{TB}}$ ) and a slightly higher normal acceleration  $a_n$  is achieved. The optimised quasi-steady-state solution is again unstable following a Hopf bifurcation.

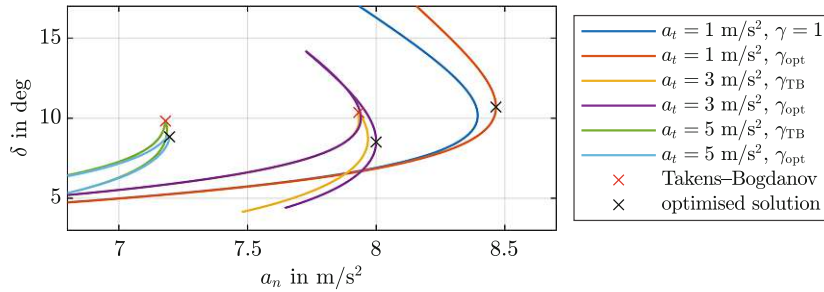


**Fig. 4.** Detail of handling diagram for different constant tangential accelerations  $a_t$  and drive torque distributions  $\gamma$ .

## 6 Conclusions

The transition between limit understeer and limit oversteer behaviour due to the change of the drive torque distribution at longitudinal acceleration in quasi-steady-state condition was investigated. It was shown that the Takens–Bogdanov solution characterises both the change from limit oversteer to limit understeer

behaviour and the change of the type of loss of stability from Hopf to Fold bifurcation.

A Takens–Bogdanov solution was identified by Della Rossa et al. in [3] by studying a pure lateral vehicle model with the same maximum friction potential of the tyres at the front and rear axles. In this study, it was shown that a similar behaviour may result from the mutual influence of longitudinal and lateral tyre forces at a vehicle accelerated in longitudinal direction.

The Takens–Bogdanov solution seems to be a reasonable design criterion for the drive torque distribution of an AWD vehicle since, for a given longitudinal acceleration (or an equivalent drive torque demand), almost the maximum normal acceleration may be achieved without ‘early’ limit understeer or oversteer behaviour. This may improve the vehicle’s safety and manoeuvrability during combined manoeuvres. In addition, the Takens–Bogdanov solution represents the acceleration envelope near the optimal (maximal) envelope. In contrast to the latter, which includes unstable solutions, the Takens–Bogdanov solution may be of more practical relevance, since the solutions are stable. However, potential practical implications have to be investigated thoroughly. The impact of relevant system parameters like tyre–road friction potential and different vehicle parameters have to be considered, and their influence on the shown method should be analysed.

Further investigations on the drive torque distribution to generate yaw torque to modify the handling behaviour and stability boundaries appear to be reasonable. This will be studied in more detail in a forthcoming paper.

## References

1. Abe, M.: A theoretical analysis on vehicle cornering behaviors in acceleration and in braking. *Veh. Syst. Dyn.* **15**(1), 1–14 (1986). <https://doi.org/10.1080/00423118608969122>
2. De Novellis, L., Sorniotti, A., Gruber, P.: Optimal wheel torque distribution for a four-wheel-drive fully electric vehicle. *SAE Int. J. Passeng. Cars Mech. Syst.* **6**(1), 128–136 (2013). <https://doi.org/10.4271/2013-01-0673>
3. Della Rossa, F., Mastinu, G., Piccardi, C.: Bifurcation analysis of an automobile model negotiating a curve. *Veh. Syst. Dyn.* **50**(10), 1539–1562 (2012). <https://doi.org/10.1080/00423114.2012.679621>
4. Eberhart, M., Plöchl, M., Edelmann, J.: Stability boundaries and bifurcation analysis of an AWD vehicle with variable drive torque distribution. To be submitted to *Nonlinear Dynamics* (2024)
5. Horiuchi, S., Okada, K., Nohtomi, S.: Analysis of accelerating and braking stability using constrained bifurcation and continuation methods. *Veh. Syst. Dyn.* **46**(1), 585–597 (2008). <https://doi.org/10.1080/00423110802007779>
6. Klomp, M., Thomson, R.: Influence of front/rear drive force distribution on the lateral grip and understeer of all-wheel drive vehicles. *Int. J. Veh. Des.* **56**(1–4), 34–48 (2011). <https://doi.org/10.1504/IJVD.2011.043272>
7. Lenzo, B., Bucchi, F., Sorniotti, A., Frenzo, F.: On the handling performance of a vehicle with different front-to-rear wheel torque distributions. *Veh. Syst. Dyn.* **57**(11), 1685–1704 (2019). <https://doi.org/10.1080/00423114.2018.1546013>

8. Massaro, M., Limebeer, D.J.N.: Minimum-lap-time optimisation and simulation. *Veh. Syst. Dyn.* **59**(7), 1069–1113 (2021). <https://doi.org/10.1080/00423114.2021.1910718>
9. Pacejka, H.: *Tire and Vehicle Dynamics*. Elsevier, Amsterdam (2005)
10. Seydel, R.: Practical bifurcation and stability analysis. In: *Interdisciplinary Applied Mathematics*, vol. 5. Springer, Cham (2009). <https://doi.org/10.1007/978-1-4419-1740-9>

**Open Access** This chapter is licensed under the terms of the Creative Commons Attribution 4.0 International License (<http://creativecommons.org/licenses/by/4.0/>), which permits use, sharing, adaptation, distribution and reproduction in any medium or format, as long as you give appropriate credit to the original author(s) and the source, provide a link to the Creative Commons license and indicate if changes were made.

The images or other third party material in this chapter are included in the chapter's Creative Commons license, unless indicated otherwise in a credit line to the material. If material is not included in the chapter's Creative Commons license and your intended use is not permitted by statutory regulation or exceeds the permitted use, you will need to obtain permission directly from the copyright holder.

